Title	A Solution to the Solar Neutrino Problem by Matter-Enhanced Neutrino Oscillations at KAMIOKANDE-II
Author(s)	福田, 善之
Citation	大阪大学, 1992, 博士論文
Version Type	VoR
URL	https://doi.org/10.11501/3060112
rights	
Note	

A Solution to the Solar Neutrino Problem by Matter-Enhanced Neutrino Oscillations at KAMIOKANDE-II

Thesis

by

Yoshiyuki Fukuda
Osaka University

February 1992

Abstract

An analysis of the MSW effect using the Kamiokande-II data is presented. Based on 1040 days of detector live time, constraints on neutrino oscillation parameters are obtained. The measured recoil-electron energy spectrum alone provides the conclusion to disfavor the adiabatic region $7.2 \times 10^{-4} \leq \sin^2 2\theta \leq 6.3 \times 10^{-3}$ and $\Delta m^2 \sim 1.3 \times 10^{-4}$ eV^2 at the 90 % confidence level.

A neutrino regeneration effect in the Earth is also searched for. No difference in the flux between day and night time is observed. A region defined by $\sin^2 2\theta \geq 0.02$ and $2 \times 10^{-6} \leq \Delta m^2 \leq 10^{-5}$ eV^2 is excluded at the 90 % confidence level without any assumption on the absolute value of the incident solar neutrino flux.

The resultant region allowed by Kamiokande-II remains on the non-adiabatic solution, the large-mixing angle solution except the region excluded by day/night neutrino flux analysis, and the small adiabatic solution.

Combined results from both Kamiokande-II and the ^{37}Cl (Homestake) experiment give the non-adiabatic solution, $\sin^2 2\theta \times \Delta m^2 \sim 10^{-7.5\pm0.2}$ and $\Delta m^2 \sim 10^{-6\pm1.2}$ eV^2, where the capture rate of ^{71}Ga experiments is predicted to be less than 80 SNU, which is consistent with the upper limit of 79 SNU (90% confidence level) from the ^{71}Ga (SAGE) experiment. Also this upper limit is assured in this paper by using results from Kamiokande-II and the Homestake experiment independent of uncertainties in the standard solar model.

Acknowledgement

The author would like to express his great appreciation to his adviser Professor Y.Nagashima and Professor Y.Totsuka for giving him the opportunity to participate in the Kamiokande-II experiment. Their excellent guidance and useful suggestions have been indispensable in his course. He will never forget that Professor M.Koshiba's deep insight, such as the production of huge 20" ϕ photomultiplier tube, which made the experiment successful.

He thanks Professor K.Nakamura who is the leader of the laboratory at Kamioka, for his management of the underground laboratory. He is also grateful to Professor Y.Suzuki and Dr.M.Takita for their many useful advises and suggestions.

He wishes to thank Professor A.Suzuki, Professor K.Miyano, Professor T.Suda, Professor T.Tanimori, Professor T.Kifune, Dr.M.Mori, Dr.Y.Oyama, Dr.K.Nishijima, Dr.H.Miyata, Dr.N.Sato, Dr.M.Yamada and Dr.K.S.Hirata for their advises.

He would like thank Dr.T.Kajita for many suggestions and discussions. The event reconstruction program was developed by him. He is particularly grateful to Dr.M.Nakahata. He was the first student of solar neutrinos at Kamiokande and Most of the early on-line program and a part of the off-line utilities used in the analysis were written by him. He gave his a lot of informations on solar neutrinos analysis.

He would like to express his appreciation to Professor K.Takahashi for his advice and support, and to KEK high energy national laboratory for financial support.

He is indebted to the stuffs of University of Pennsylvania for their collaboration to install the Pennsylvania electronics.

He owes thanks to the collaborations, who worked on the various stages of this experiment and helped him on many occasions, K.Kaneyuki, K.Kihara, Y.Yaginuma, K.Inoue, S.Ohara, T.Ishida, A.Sakai, H.Takei, T.Tajima, T.Kajimura, E.Kodera, and H.Yokoyama.

He thanks the cooperation of Kamioka Mining and Smelting Company. This experiment is supported by the Japanese Ministry of Education, Science and Culture, by the United States Department of Energy, and by the University of Pennsylvania Research Fund.

All of the analysis have been carried out using FACOM M780 and M380 at the Institute for Nuclear Study, University of Tokyo. He is also grateful to the staffs there for their help.

Contents

Chapter 1

Introduction

1.1 Solar Neutrino Experiment

Main-sequence stars like the Sun shine through the fusion reactions of light nuclei. These fusion reactions produce not only the thermal energy, which is released as photons from the surface of the Sun, but also solar neutrinos. The experiment of the solar neutrino detection has two important physical objectives.

One objective is to investigate the interior of the Sun. Created photons by nuclear fusion reactions take several millions of years to go out from the surface of the Sun. Therefore, the optical sighting of the Sun does not reflect the present interior temperature of the Sun. Neutrinos, on the contrary, have extremely low interaction probability with matter. Solar neutrinos created at the deep solar interior, therefore, carry real time information in the Sun. The detection of such solar neutrinos provides with some information of the stellar interior, which is important for the study of stellar evolution models.

The other is to investigate intrinsic properties of the neutrino as an elementary particle. It is usually assumed that neutrinos have no charge, no magnetic moment and no mass. However, an electroweak standard model can be extended to incorporate finite magnetic dipole moment as well as finite mass. If neutrinos possess such properties actually, some new yet-unknown phenomena, such as neutrino oscillations, might take place.

A muon neutrino (ν_μ) beam is artificially available at high energy accelerators from charged pion decay ($\pi^{\pm} \rightarrow \mu^{\pm} + \overset{(-)}{\nu}_{\mu}$) and an anti electron neutrino ($\bar{\nu}_e$) beam is also available at nuclear reactors. The Sun provides a beam of high-intensity (6.6×10^{10} cm^{-2} sec^{-1}) and uni-directional low energy (≤ 15 MeV) neutrinos that traverse 1.5×10^{11} m from the Sun to the Earth. Therefore, solar neutrinos are the unique high-intensity ν_e beam presently available.

1.2 Standard Solar Model

The standard solar model (SSM), which has been extensively developed by J.N.Bahcall and his colleagues, describes the mechanism of how the Sun burns [1]. In particular, the standard solar model provides energy spectra of neutrinos produced by nuclear fusion reactions in the solar interior.

Some principal assumptions are employed in constructing the standard solar model. This model assumes that the Sun is a spherically symmetric plasma in hydrostatic equilibrium maintained by the gravitational force balanced against the radiative and particle pressures, that the energy transport is primarily by photon diffusion in the deep interior, that the primary energy source for the radiative photons and neutrinos is given by nuclear fusion reactions, and that the initial solar interior is presumed to have been chemically homogeneous and changes in the local abundance of individual isotopes produced only by nuclear reactions. The pressure, density and temperature are related through the equation of state with the effect of radiation pressure and electron degeneracy and screening interactions. Moreover, the standard solar model requires chemical abundances, radiative opacity and cross section of nuclear reactions. The constraints for the standard solar model are precise values of the solar mass, radius, geometric shape, photon spectrum, total luminosity and age. These principal parameters are shown in Table.1.1.

The Sun evolves with loss of photons from the surface, which is balanced by the burning of 4 protons into an α-particle in the core of the Sun. This reaction can be represented by the relation,

$$4p \rightarrow \alpha + 2e^{+} + 2\nu_e + 25.14 \text{ MeV}. \tag{1.1}$$

Here, the last term of Eq.(1.1) is the thermal energy (average energy carried away by neutrinos is subtracted) released for four protons burned in the process, and the energy ultimately emerges from the surface of the Sun as sunlight.

The major nuclear reactions in the Sun, which generate 95% of the total energy, are presumed to be ***proton-proton*** (pp) chain as shown in Fig.1.1. Other minor reactions that produce 1.5% of total luminosity is called the Carbon-Nitrogen-Oxygen (CNO) cycle. At higher temperatures than that relevant for the solar interior, the CNO cycle involves side chains as shown in Fig.1.2. These side chains do not significantly affect the energy production, because the CNO cycle itself contributes a small fraction of the total solar luminosity.

The energy spectra and total flux of various solar neutrino sources calculated by Bahcall and Ulrich [1] based on the standard solar model are shown in Fig.1.3 and summarized in Table 1.2. These solar neutrinos carry 2.3% of the photon luminosity, which corresponds to an average energy of 0.572 MeV lost in pp chain.

There are theoretical uncertainties in the calculation of the neutrino flux and spectra based on the standard solar model. They are the nuclear reaction cross section, the present composition of the solar surface, the radiative opacity, the equation of state of stellar material and other solar parameters. In practice, the neutrino flux depends sensitively on such a number of input parameters. Explicitly, pp, ^{7}Be and ^{8}B neutrino flux are represented by the following expression [2];

$$\Phi(\mathrm{pp}) \propto S_{11}^{0.14} S_{33}^{-0.03} S_{34}^{-0.06} L_{\odot}^{0.73} (Z/X)^{-0.08} (\mathrm{age})^{-0.07} \approx const. \times T^{-1.2} , \quad (1.2)$$

$$\Phi(^7\mathrm{Be}) \propto S_{11}^{-0.97} S_{33}^{-0.43} S_{34}^{0.86} L_{\odot}^{3.4} R_{\odot}^{0.22} (Z/X)^{0.58} (\mathrm{age})^{1.3} \approx const. \times T^{8} , \quad (1.3)$$

$$\Phi(^8\mathrm{B}) \propto S_{11}^{-2.6} S_{33}^{-0.40} S_{34}^{0.81} S_{17}^{1.0} L_{\odot}^{6.8} R_{\odot}^{0.48} (Z/X)^{1.3} (\mathrm{age})^{1.3} \approx const. \times T^{18} , \quad (1.4)$$

where S is the nuclear cross section factor (the subscripts on S show the mass number of the interacting nuclei), $L_{\odot}$ is the solar luminosity, $R_{\odot}$ is the solar radius and (Z/X) is the initial chemical abundance ratio of heavy element to hydrogen, and T is the central temperature.

The nuclear reaction parameters for pp chain and CNO cycle are given in Table.1.3 with their estimated uncertainties at 1 standard deviation (1σ) limit. Here, pp and pep reactions have little uncertainties ($\sim 3\%$), so pp and pep neutrino flux are most reliably predicted in the calculation based on the standard solar model. The most important and crucial reaction for the detection of solar neutrinos is the ^{7}Be + p reaction, which produces the ^{8}B neutrinos. The low energy cross section for this reaction is uncertain by 22% (3σ), which translates into an equal uncertainty in the predicted flux of ^{8}B neutrinos. This limit is hard to improve significantly because the statistical and systematic difficulties exist in the measurement of the small interaction cross section. The reaction rates of the pp and ^{7}Be + e^- must be calculated, not measured. The uncertainties in these reactions are evaluated by considering different theoretical calculations.

The present composition of the solar surface is presumed to reflect the initial abundance of all the elements ($\gtrsim$ Carbon). The initial ratio of heavy element to hydrogen, Z/X, is one of crucial input parameters in the determination of solar models. The recent value of Z/X is estimated by about 0.27 and the uncertainty is estimated by about 19%.

The uncertainties in the radiative opacity has been estimated by comparing each neutrino flux that is calculated by using different opacity code. The calculated flux from the pp, pep, and ^{7}Be neutrinos agree to better than 10%, and for ^{8}B decay differ by about 16%.

The value of solar constants shows agreement with each other at the level of a percent. The systematic errors in some of the experiments appear to be larger than the statistical errors. A nominal value and the uncertainty are consistent with all of the recent measurements. For example, the solar luminosity is obtained as $L_\odot = 3.86(1 \pm 0.005) \times 10^{33}$ erg s^{-1}.

1.3 Solar Neutrino Problem

The chlorine-37 (^{37}Cl) radio-chemical (Homestake) experiment of R.Davis and his collaborators is the only solar neutrino detector which has been operating since 1968 in the Homestake Gold mine at South Dakota, USA [3]. They have claimed over the last 20 years that the measured neutrino flux is a quarter of the SSM prediction, and this is called the *solar neutrino problem*. Their long-term average neutrino capture rate is 2.3 ± 0.3 (1σ) SNU, while the value 7.9 ± 2.6 (effective 3σ) SNU was predicted by the

SSM calculated by Bahcall and Ulrich [1]. Here, one SNU (Solar Neutrino Unit) corresponds to one capture per 10^{36} atoms per second. The deficit in solar neutrinos has been interpreted as; (i) the neutrino detection efficiency of the Homestake experiment is incomplete, (ii) The SSM prediction is incorrect, and (iii) Electron neutrinos (ν_e's) on the way to the Earth are transformed into another kind of neutrinos, which are insensitive to the Homestake experiment.

At the beginning of 1987, KAMIOKANDE-II (KAM-II) detector which was originally constructed to search for the proton decays, started to detect solar neutrinos. The measured flux of solar neutrinos obtained from the data with $E_e \geq 9.3$MeV is $0.46 \pm 0.13(stat.) \pm 0.08(sys.)$ based on the first 450 days' data [4], and $0.46 \pm 0.05(stat.) \pm 0.06(sys.)$ based on KAM-II 1040 days' data [5] relative to the SSM prediction. This value was roughly twice as large as the one obtained from the Homestake experiment. However, the existence of the deficit has been confirmed by KAM-II, which uses a completely different experimental technique.

Many possible solutions have been proposed by theorists such as uncertainties of the standard solar model, non-standard solar models, neutrino oscillations, neutrino decays, WIMPs (Weakly Interactive Massive Particles) and so on. Possibilities for neutrino oscillations, neutrino decays and WIMPs will be discussed in the following subsections.

There are some uncertain parameters in the nuclear fusion processes as described in the previous section. For example, the Homestake experiment and KAM-II are sensitive mainly to relatively high-energy ($\lesssim$ 15 MeV) neutrinos emitted from the beta-decay of ^{8}B nuclei. Hence, the solar neutrino problem may be solved by reducing the production rate of ^{8}B nuclei. Unfortunately, it is one of the most uncertain predictions of the SSM. It depends sensitively on the temperature in the solar interior and the cross section of ^{7}Be + p reaction in the low-energy regions (see Eq.(1.4)). It has been argued that the solar neutrino problem may be solved by lowering temperature of the solar interior. However, the combined results from both KAM-II [5][6][7] and the Homestake experiment [8] disfavor models trying to lower the central temperature in the Sun. Moreover, a ^{71}Ga radio-chemical experiment (SAGE) at Baksan Neutrino Laboratory has presented a new result recently, suggesting a deficit in pp neutrinos [9]. They observed the neutrino capture rate to be 20 $^{+15}_{-20}$ (stat.) ± 32 (sys.) SNU, resulting in a limit of 79 SNU (90% C.L.). This is to be compared with the predicted capture rate of 132 $^{+20}_{-17}$ (3σ) SNU by the SSM [1]. The most significant contribution to the predicted capture rate by the ^{71}Ga experiment is pp neutrinos produced by the deuteron formation reaction. The prediction of pp neutrinos flux is considered to be reliable (±2% at 3σ). Therefore, if their result is indeed true, there remains only one possibility to solve the solar neutrino problem, that neutrinos produced in the solar interior might somehow disappear in transit to the Earth due to unknown properties of neutrinos as an elementary particle.

In the following subsections, some possible explanations based on this hypothesis will be presented.

1.3.1 Neutrino Oscillations

If neutrinos have finite masses and mixing angles, the eigenstates of the weak interaction (ν_e, ν_μ, ν_τ) are not necessarily identical with the mass eigenstates (ν_1, ν_2, ν_3) and the neutrino flavor oscillations are expected. For instance, an electron neutrino (ν_e) generated in the Sun is converted into another type of neutrino such as a muon neutrino (ν_μ) or tau neutrino (ν_τ) on its way to the Earth. The solar neutrino problem might be explained by neutrino oscillations, if Δm^2 (the difference between mass squared of the two eigenstates) is greater than $\sim 10^{-11}$ eV^2 and neutrino wave functions have a large mixing angle ($\sin^2 2\theta \gtrsim 0.5$) [10][11]. This is well-known as neutrino vacuum oscillation.

In 1985, S.P.Mikheyev and A.Yu.Smirnov pointed out the possible effect of the neutrino oscillations in the solar matter, based on the theory developed by L.Wolfenstein. [10]. This theory gives an attractive scenario that electron neutrinos are efficiently converted into muon or tau neutrinos by resonant oscillations in the solar matter, if Δm^2 is in the range of 10^{-4} $\sim 10^{-7}$ eV^2 even for a small value of the mixing angle ($\sin^2 2\theta \sim 10^{-4} - 10^{-3}$).

Theoretical explanation of these neutrino oscillations will be given in more detail in section 1.5.

1.3.2 Neutrino Magnetic Moment

If neutrinos have a large magnetic moment on the order of 10^{-11} μ_B, where μ_B is the Bohr magneton, and if the convective layer of the Sun possesses the solar magnetic field of a few thousand gauss, a left-handed neutrino (ν_L) might be converted into a right-handed one (ν_R) via its spin flip as it traverses the solar magnetic field. [13]. The right-handed neutrinos have no interaction with matter and thus are undetectable by solar neutrino experiments.

However, a natural extension of the standard electroweak theory predicts the neutrino magnetic moment on the order of 10^{-19} μ_B based on the experimental upper limit of 9 eV on the neutrino mass [14], since the magnetic moment operator has the same chiral structure as the mass operator. Therefore, the diagram that generates a large $\mu_\nu \sim O(10^{-11})\mu_B$ will naively also induce a large $m_\nu \sim O(\mathrm{keV})$ without fine-turning. Recently, M.Voloshin, M.Vysotskii and L.Okun made a suggestion that neutrinos have possible large magnetic moment while keeping neutrino mass naturally small [15]. If $\mu_\nu B \geq 6-12\times(10^{-10}\mu_B)\times(1\mathrm{kG})$, a reduction of the original ν_L-flux is desired and the azimuthal asymmetry of the electron scattered by the solar neutrinos is expected by real-time, large volume detector, such as KAM-II, but with sufficient angular resolution [16]. Also, the neutrino transitions due to a large magnetic interaction with the solar magnetic field might be a possible solution of the anti-correlation of the observed neutrino flux with the solar activities, which have been claimed by Homestake experiment [17]. However, KAM-II observed no significant time variation of neutrino flux during the 1040 days' measurement. Therefore, the hypothesis suggested by R.Davis is contradicted by the results from our measurement.

A Dirac-type magnetic moment is strongly suppressed by cosmological and astrophysical constraints. Existing experimental limits of neutrino magnetic moment are obtained by using $\bar{\nu}_e$ scattering experiment made with reactors [18]; $\mu_\nu \leq 2\times10^{-10}\mu_B$ and using ν_μ ($\bar{\nu}_\mu$) scattering experiment made with accelerators [19]; $\mu_\nu < 0.85\times10^{-9}\mu_B$ at 90% confidence level. Especially, the observations of neutrino burst from SN1987A by KAM-II [20] and IMB [21] give a strong constraint of $\mu_\nu < 10^{-12} \sim 10^{-13}$ μ_B [22]. Therefore, the Dirac-type magnetic moment seems difficult to explain the solar neutrino problem.

A Majorana-type magnetic moment in combination with the matter effect on the neutrino oscillations was proposed by C.S.Lim and W.J.Marciano [23], and by Akhmedov et al. [24], because the solution may explain the solar neutrino deficit as well as the anti-correlation between the sunspot numbers and the observed solar neutrino flux by Homestake experiment. In this case, the generated electron neutrinos (ν_e) should be converted into anti-muon neutrinos ($\bar{\nu}_\mu$). The recent analysis concluded that the best fit values which reconcile the results from KAM-II and Homestake experiment are $\Delta m^2 \sim 10^{-8}$ eV^2 and $\mu_\nu \sim 10^{-11}\ \mu_B$ [25]. Also, the converted $\bar{\nu}_\mu$'s may oscillate into $\bar{\nu}_e$'s in vacuum on their way to the Earth. The $\bar{\nu}_e$ non-observation at KAM-II will give a constraint on the explanation, because only KAM-II is sensitive to the $\bar{\nu}_e$ flux and the expected event rate will be approximately 20 times greater than all other neutrino interactions.

But, there are unfortunately several serious uncertainties in its assumption, such as the strength or the structure of solar magnetic field in the convective zone, and unnaturally requirements of large magnetic moment. Therefore, it is not necessary to discuss this case in any detail.

1.3.3 Neutrino Decays

Another possible solution for the solar neutrino problem is neutrino decay on their way from the Sun to the Earth [26]. However, the observation of $\bar{\nu}_e$ flux from SN1987A excludes the fast radiative decay ($\nu_e \rightarrow \nu_\mu + \gamma$) [27].

The only remaining possibility is ν_e decay during their trip [11]. This solution requires only two flavors of neutrinos, however, it also requires a new light boson or majoron. The neutrino decay branch is assumed to be;

$$\nu_2 \rightarrow \bar{\nu}_1 + \phi(M) \tag{1.5}$$

($\nu_2 \rightarrow \nu_1 + \phi(M)$ is disfavored since it induces a large rate for $\mu \rightarrow e + \phi(M)$), where ϕ is a scalar boson, especially M is the majoron which should have sufficient strong off-diagonal couplings with the neutrino mass eigenstate $\nu_{1,2}$, and the masses m_1 and $m_{\phi(M)}$ are taken to be much lighter than m_2. For majoron model, the most familiar candidate, the triplet majoron, has been ruled out by LEP data on Z-boson invisible width [28], whereas the singlet majoron is very weakly coupled to neutrinos. However, a variety of new singlet majoron models can be considered, in which the scale of lepton number violation can be sufficient low as to provide coupling constant in the proper range.

The ν_2 is assumed to be a mixture of ν_e and ν_μ with the convention for the mixing angle (θ) to be the same as for the usual oscillation case, that electron neutrino becomes the lower-mass eigenstate as the mixing angle $\theta \rightarrow 0$. Then the relevant average neutrino survival probabilities are given by;

$$P(\nu_e \rightarrow \nu_e) = \cos^4\theta + \sin^4\theta exp[-t/\tau(E)], \tag{1.6}$$

$$P(\nu_e \rightarrow \nu_\mu) = \sin^2\theta\cos^2\theta[1 + exp(-t/\tau(E))], \tag{1.7}$$

where $t = 480$ sec and $\tau(E) = (E/m^2)\tau_0$ with the neutrino energy (E) and the decay lifetime (τ_0). There are also two other survival probabilities which are physically relevant, the ones with anti-neutrinos in the final state. The probabilities for anti-neutrinos were evaluated in the calculations, however, it is found that in practice they are unimportant for present experiments. The final state anti-neutrinos have lower energies than the original neutrinos and give a negligible contribution to neutrino-electron scattering experiments such as KAM-II. The typical lifetime with an energy of 10 MeV given by the allowed region for the solar neutrino deficit is the same order or slightly larger than the propagation time of neutrinos, and the electron neutrino survival probability has an energy dependence in such a way that the lower energy neutrinos are reduced more heavily than the higher one.

This scenario concludes that typical 10 MeV neutrinos have a lifetime of 800 sec and the mixing angle in the range of $45° < \theta < 60°$. However, the assumption introduces an disfavored scalar boson ϕ or majoron with strong coupling constants, and is thought to be rather exotic.

1.3.4 WIMPs

Weakly interactive massive particles (WIMPs) were introduced to solve both the solar neutrino and the dark matter problem [29]. The WIMPs can be regarded as good thermal conductors which efficiently transfer heats from the core to the outer region of the Sun, because WIMP cross sections are small compared to typical photon cross section ($\gtrsim 10^{-24}$ cm^2). Thus the WIMPs lower the core temperature and reduce the ^{8}B neutrino flux. For instance, if WIMPs have a mass of 4 GeV/c^2, an elastic scattering cross section on protons of the order of 10^{-36} cm^2, and a relative mass fraction of the order of $\sim 10^{-8}$, the effective heat transport is expected and the desirable mean free path, λ, is $\lambda \sim R_\odot/20$ (the radial extent of the region in which ^{8}B neutrinos are produced). Hence, the solar neutrino problem can be solved by reducing ^{8}B neutrino flux. However, as described in the beginning of this section, the manipulation of the standard solar model by lowering the central temperature in the Sun can not account for the recent results. Therefore, it is not necessary to explain more about this possibility.

1.4 Present Status of Solar Neutrino Experiments

1.4.1 The ^{37}Cl Homestake Experiment

The chlorine-37 (^{37}Cl) radio-chemical (Homestake) experiment of R.Davis and his collaborators is the only solar neutrino detector which has been operating since 1968 in the Homestake Gold mine in South Dakota, U.S.A. [3]. The detector consists of 3.8×10^5 liters of liquid perchloroethylene (C_2Cl_4) contained in a tank which includes 2.16×10^{30} of ^{37}Cl atoms. The neutrino absorption reaction to the ground state of ^{37}Ar;

$$^{37}\mathrm{Cl} + \nu_e \;\rightarrow\; ^{37}\mathrm{Ar} + \mathrm{e}^-, E_{th} = 0.814\mathrm{MeV} \tag{1.8}$$

has a relatively low energy threshold (0.814 MeV) and a favorable cross section of the neutrino capture reaction (relatively small $ft_{1/2}$ value, log ft = 5). Assuming the standard solar model, ie., the neutrino fluxes calculated by Bahcall and Ulrich, the ^{37}Ar atom production rate is estimated to be 1.48 ± 0.49 atoms per day, which corresponds to 7.9 ± 2.6 (3σ) SNU. (The SSM calculated by Turck-Chièze et al. predicts 5.8 ± 1.3 (1σ) SNU for the Homestake experiment.)

The ^{37}Ar atoms produced by the neutrino capture reaction in the tank are extracted by circulating about 4×10^5 liter of helium (He) at intervals of one to three months. The recovery efficiency of the ^{37}Ar atoms is measured for each exposure using the isotope carrier gas ($\sim 10^{19}$ atoms of ^{36}Ar or ^{38}Ar) which was added into the tank at the beginning of each run. A typical extraction efficiency is more than 90%.

The ^{37}Ar counting was performed with a proportional counter which observed 282 keV Auger electrons from the electron capture decay of ^{37}Ar ($\tau_{1/2} = 35.0$ days) for a period of approximately eight months. This counter has a resolution of about 25% for electrons of this energy. The signal from the decay of ^{37}Ar is characterized by the deposited energy and the short rise time, which is distinct from slower pulses produced by beta-rays, cosmic rays and Compton electrons. The integrated charge during a short time (about 10 nsec) for a fast pulse like the ^{37}Ar decay signal is greater than that for a slower one with the same energy.

The main background source is caused by energetic cosmic ray muons that are produced in the upper atmosphere. In order to estimate the background rate, 600 gallons of C_2Cl_4 were exposed at shallow depth in the mine and the production rate of the ^{37}Ar atoms at the experimental site was obtained by extraporating the data. The average background rate is estimated to be 0.08 ± 0.03 ^{37}Ar atom production per day which corresponds to 0.4 ± 0.16 SNU.

Subtracting this background rate, the average net ^{37}Ar production rate due to solar neutrinos for an experimental period from 1970 to 1985 is 0.47 ± 0.04 atoms per day which corresponds to 2.1 ± 0.3 (1σ) SNU [16]. The most recent value of the averaged capture rate including the data up to 1990 is 2.3 ± 0.3 (1σ) SNU [8].

There is a large discrepancy of 6σ between the measured neutrino capture rate and the prediction (7.9 ± 2.6 (3σ) SNU) of the SSM. Approximately 77% of the whole capture rate (6.1 ± 2.2 (3σ) SNU) is ascribed to ^{8}B neutrinos and 14% (1.1 ± 0.2 (3σ) SNU) to ^{7}Be neutrinos. The theoretical uncertainty in the predicted neutrino capture rate is mostly caused by the uncertainty in the ^{8}B neutrino flux of 37% (3σ).

In addition to the deficit of neutrinos, it has been pointed out that the ^{37}Ar production rate may be anti-correlated with the 11-year period of sunspot activities and affected by large solar flares. Figure 1.4 shows the anti-correlation between the observed sunspot number and the averaged ^{37}Ar counting rate as a function of time. Apparently, one sees an anti-correlation between them. But there exist two difficulties to understand this anti-correlation.

^{8}B solar neutrinos are produced deep inside of the solar interior. The typical time scale for changing a physical condition in the Sun exceeds the Kelvin-Helmholz time, which is on the order of 10^7 years. Therefore, the neutrino flux should be constant for a period of roughly Kelvin-Helmholz time. The other is that the statistical accuracy is poor in the ^{37}Cl measurement. If their averaged neutrino capture rate is constant, the confidence limit of 3% is obtained.

Moreover, KAM-II, which has observed the ^{8}B solar neutrinos since the beginning of 1987, found no significant time variation of the neutrino flux. The correlation of the ^{8}B solar neutrino flux and the sunspot activities is shown in Fig.1.5 in which the data are divided into five time intervals, each of approximately 200 days of detector live time. The data-taking time extends over a period in which sunspot activities, reflecting the solar magnetic cycle, rose steeply from a minimum value at the end of solar magnetic cycle 21 to a maximum value approximately 15 times larger at the peak of solar cycle 22. There is no evidence for the time variation suggested by the Homestake experiment. The KAM-II also gives negative results on searches for neutrino bursts in a short time internal correlated with a solar flare [30] which has been claimed by the Homestake experiment.

In this way, the anti-correlation between the solar neutrino flux and the sunspot activities is ruled out by the result from the KAM-II 1040 days' data.

1.4.2 Kamiokande-II Experiment

The KAM-II detector is a large water Čerenkov calorimeter which is located 1000 m underground (2700 m water equivalent) in the Kamioka metal mine in Gifu prefecture of Japan, at 36.4°N, 137.3°E and 25.8°N geomagnetic latitude. The detector consists of an inner counter and an outer anti-counter. The inner main (Čerenkov) detector is contained in a cylindrical steel tank and has a volume of 14.4 m (in diameter) × 13.1 m (in height), containing 2142 tons of water. A total of 948 PMTs, each with 50 cm ϕ photosensitive area, cover 20% of the entire inner surface of the water tank. The fiducial mass for the ^{8}B solar neutrino measurement is 680 tons. A 4π solid-angle anti-counter surrounding the main detector is a water Čerenkov counter of total mass

1800 tons with 123 (50 cm ϕ) PMTs to detect any signals outside the main detector volume and to shield against gamma rays and neutrons from outside the detector. The entire inner surface of anti-counter section is covered by alminium sheets to obtain good light collection efficiency. The mean thickness of water in the anti-counter is 1.2 m, 0.8 m and 1.7 m at the bottom, top and barrel sections, respectively. The Čerenkov lights emitted from an electron via elastic scattering by a incident solar neutrino are detected by the inner counter.

The scattering angle of an electron via the relation;

$$\nu_e + e^- \rightarrow \nu_e + e^-, \tag{1.9}$$

is given by;

$$\cos\theta_c = \frac{1 + m_e/E_\nu}{\sqrt{1 + 2m_e/T_e}}, \tag{1.10}$$

where θ_c is the scattering angle, m_e is the electron mass, E_ν is the energy of incident neutrino and T_e is the kinetic energy of the recoil electron. The minimum detection energy of the neutrinos at KAM-II detector is above 7.5 MeV, so we are searching for only ^{8}B neutrinos from the Sun. The expected event rate due to ^{8}B neutrino reaction is 0.86 event per day per 680 ton for $E_e \geq 7.5$ MeV and 0.28 event per day per 680 ton for $E_e \geq 10$ MeV, according to the calculation of Bahcall and Ulrich [1].

Compared with a radio-chemical detector such as Homestake experiment, a water Čerenkov detector has an advantage of recording the direction, energy, and event vertex position of the recoil electron in real time. These advantages are very important for the measurement of the ^{8}B solar neutrino flux as well as the analysis of the MSW neutrino oscillations and the Day/Night effect (the neutrino regeneration effect in the Earth) which will be discussed in the next section. In the KAM-II experiment, we are interested only in $E_\nu \gg m_e$, so the incident neutrino direction is largely preserved in the recoiling electron direction. The detector has an angular resolution of 28° at 10 MeV which is mainly limited by multiple Coulomb scattering in water. The directional correlation of events with respect to the Sun provides a powerful tool to discriminate the solar neutrino events from the background events which are assumed to have a flat angular distribution.

Each event has information of electron energy and its arrival time. The energy resolution is 20% at 10 MeV, as approximated in the following formula;

$$\frac{\sigma(E_e)}{E_e} = \frac{0.63}{\sqrt{E_e}}, \tag{1.11}$$

where E_e is the electron total energy in MeV. If the event is caused by a solar neutrino, one can obtain the neutrino track passing through the Earth from the event arrival time. The MSW effect in the Sun predicts the distortion of the energy spectrum due to conversion of ν_e's into ν_μ's or ν_τ's. The Day/Night effect also predicts the regeneration of ν_e's from ν_μ's or ν_τ's which were converted in the Sun. Especially the strength of the regeneration depends on the path length and density gradient through which neutrinos pass in the Earth. Therefore, only the KAM-II detector can directly make a test for the MSW effect and the Day/Night effect.

The observed neutrino flux obtained by KAM-II 1040 day's data is as follows;

$$\frac{\text{Data}}{\text{SSM}} = 0.46 \pm 0.05(stat.) \pm 0.06(sys.)\,. \tag{1.12}$$

As described in the previous section, we found no significant time variation of the neutrino flux and no correlation between neutrino flux and solar flares. A more detailed description of the KAM-II detector will be given in Chapter 2.

1.4.3 The ^{71}Ga Solar Neutrino Experiments (SAGE and GALLEX)

The gallium (^{71}Ga) solar neutrino experiment is also a radio-chemical experiment. Two ^{71}Ga experiments are in progress in the Soviet Union (SAGE) and in Italy (GALLEX). They are the only experiments that can detect very low-energy pp neutrinos ($E_{pp} \leq 0.42$ MeV).

The neutrino capture reaction that is used in these radio-chemical experiments is;

$$^{71}\text{Ga} + \nu_e \rightarrow ^{71}\text{Ge} + e^-,\ E_{th} = 0.2332\text{MeV}. \tag{1.13}$$

The radioactive ^{71}Ge decays by electron capture, the inverse reaction of Eq.(1.13), with a lifetime of $\tau_{1/2} = 11.43$ days. The low energy threshold makes possible the detection of pp neutrinos.

The capture rate predicted by the SSM of Bahcall and Ulrich for the ^{71}Ga experiment is relatively well determined, because for the pp neutrino, which occupies 54% of the total capture rate, the capture rate and is the cross section for the ground state to the ground state transition are reliably calculated. About 26% of the capture rate comes from ^{7}Be neutrinos, whose contribution in SSM is also evaluated with good accuracy. The total capture rate derived from SSM is 132 $^{+20}_{-17}$ SNU [1], which corresponds to 1.17 events per day in a 30 ton target of gallium.

Table 1.4 shows the contribution of each neutrino source to the predicted capture rate. The dominant uncertainty is caused by the transition to excited states whose matrix elements are inferred from (p,n) measurements which have sizable errors. The maximum increase that could be caused by excited state transitions is +16 SNU and the corresponding extreme decrease is −8 SNU. Excited state transitions contribute 88% (12 SNU) of the total ^{8}B contribution. The shape of ^{8}B absorption cross section versus excitation energy has a broad peak in the range 3 MeV to 5 MeV, which contains about one-third of the total calculated transition strength. If one ignores all of the uncertainties associated with the excited state transition, then the remaining total calculated uncertainty should be only 9% (12 SNU) of the total capture rate. Excited state transitions cause a significant uncertainty (about 10% of the total capture rate) for SSM predictions, an uncertainty which seems unavoidable unless an unexpected major improvement is achieved in the accuracy with which GT matrix elements to excited states can be determined.

The cross section for absorption of neutrinos from a calibrating source of ^{51}Cr is

$$\sigma(^{51}\mathrm{Cr}\ on\ ^{71}\mathrm{Ga}) = 59(1 \pm 0.1) \times 10^{-46}\mathrm{cm}^2. \qquad (1.14)$$

Exited states contribute only 6% to the cross section; state above 0.5 MeV require too much energy to be populated by ^{51}Cr neutrinos. Therefore the calibration of the ^{71}Ga detector with a ^{51}Cr source can not remove the significant uncertainty in the sensitivity caused by transitions to highly excited states. The ^{51}Cr calibration is a test for the overall efficiency of the detecting system.

The GALLEX detector is placed in the Gran Sasso Underground Laboratory, Italy [31]. The detector consists of 30 tons of gallium in the form of a concentrated $GaCl_3$-

HCl solution. The neutrino-induced ^{71}Ge atoms become volatile molecule $GeCl_4$. A measured amount of inactive Ge carrier atoms, which also form $GeCl_4$, is added at the beginning of a run to provide a sufficiently so large sample for extraction that the efficiency can be determined experimentally after each run. At the end of an exposure, the $GeCl_4$ is swept out of the solution by bubbling air or nitrogen gas through the tank. The gas stream is then passed through two gas scrubbers where the $GeCl_4$ is absorbed in water. The $GeCl_4$ is then extracted and formed into gas germane, GeH_4. The GeH_4, together with xenon, is introduced into a small proportional counter (0.5 cm^3), where the number of ^{71}Ge atoms is determined by observing their radioactive decays. The energy deposition from Auger electrons and from X-rays emitted in the ^{71}Ge electron capture decay results in an energy spectrum with two peaks: an L peak at 1.2 keV and a K peak at 10.4 keV. The detection efficiency is estimated to be above 98%.

All provisions for low-level counting have to be applied in order to reach the low background rates required: such as ultra pure materials for the counter construction, an anti-coincidence shield with NaI and plastic scintillation detectors, and heavy passive shielding with lead and iron. The residual background in the L and K peak energy windows is of the order of 1 count per day. This remaining background is from beta-particles that are produced by natural radioactivity in the construction materials, from Compton electrons caused by external gamma-rays, and from electronic noise pulses. Fortunately, these background events produce pulse shape different from those of ^{71}Ge decays. The combination of pulse energy and rise time can, therefore, be used to count the ^{71}Ge with a very small background rate as discussed in the Homestake experiment. The most serious background reaction is ^{71}Ga(p,n)^{71}Ge, the protons being generated in the $GaCl_3$ solution as secondaries from (α,p) and (n,p) reactions and from cosmic ray muon interactions. The ^{71}Ge production by fast neutrons entering the solution from outside has been studied with a Pu-Be neutron source. This effect sets limits on the fast neutron flux at the detector site. Measurements suggest that the background from fast neutron is small ($< 2\%$).

The depth dependence of the ^{71}Ga production in $GaCl_3$ by cosmic ray muons has been derived from measurements and calculations on the same effect for Homestake experiment and from the measured cross section ratio (^{71}Ge from $GaCl_3$)/(^{37}Ar from

C_2Cl_4) for 225 GeV muons. For the shielding depth of the Gran Sasso Underground Laboratory, the ^{71}Ge production rate is estimated to be of order 0.01 atoms per day in 30 tons of gallium, corresponding to a muon background of a few SNU or less. The experiment has started last year and we are looking forward to their result.

The SAGE (Soviet-America Gallium Experiment) is carried out in an underground chamber that was excavated underneath a mountain. The excavation was carried out in the Andyrchi mountain massif of the North Caucus region in the Baksan river valley; the facility is known as the Baksan Neutrino Observatory. There are two main difference between the SAGE and GALLEX experiments: (i) the SAGE has chosen to use a metal gallium target, rather than $GaCl_3$ solution; and (ii) the SAGE target will contain 60 tons of gallium (now they use only 30 tons), [32]. After the initial extraction steps, experimental procedures including the chemical processing and the counting are similar in the two experiments.

The main advantages of SAGE are: (i) the metal target is less sensitive to the background reactions produced by radioactive impurities; (ii) a metal target has a smaller volume (which reduces some other backgrounds) because of its much larger density. The smaller volume also enhances the production rate in a laboratory calibration experiment with ^{51}Cr. The main disadvantage of the metal target is that each time the germanium is separated it is necessary to add fresh chemical reagents. Therefore, one must control strictly the germanium impurities. The greater complexity of the initial extraction procedure makes it more difficult to demonstrate that the chemical processing is free of unknown systematic effects.

Gallium metal melts at about 30°C, permitting the liquid (which has a density of 6.0 g cm^{-3}) to be mixed with dilute hydrochloric acid. To remove germanium, hydrogen peroxide is added to the dilute acid and the entire mass is mixed vigorously. The extracted solutions from the four (10 in the full scale experiment) separate reactors are combined and reduced in volume by vacuum evaporation. Additional HCl is then added and an argon purge is initiated which sweeps the Ge as $GeCl_4$ from the acid solution. The extracted Ge then forms gas germane GeH_4 and the GeH_4 is mixed with a measured quantity of xenon and is inserted into a low-background proportional counter (these procedures are similar to that described above for GALLEX experiment). The overall extraction efficiency is typically 80% with an uncertainty of ±6%. With a typical counter filled with an 80% Xe-20% GeH_4 mixture at 600 Torr, 37% of the decays are observed in the K peak at 10.4 keV and 34% in the L peak at 1.2 keV.

The first result for their five month exposures was published in 1991 [9]. The result is that the upper limit on the neutrino capture rate is 79 (55) SNU at 90 (68)% C.L. and the best fit value is 20 $^{+15}_{-20}$ (stat.) ± 32(sys.) SNU, assuming their extraction efficiency for ^{71}Ge atoms produced by solar neutrinos is the same as from the natural Ge carriers. Although the statistic and systematic errors are still large. This result, however, leads us to a very important conclusion.

Different standard solar models predict that the total capture rate in ^{71}Ga is in the range between $125 \pm 5(1\sigma)$ SNU [41] and 132 $^{+20}_{-17}(3\sigma)$ SNU [1], with dominant contribution (71 SNU) coming from the pp neutrinos. The minimum expected rate in Ga experiment, assuming only that the Sun is presently generating nuclear energy at the rate at which it is radiating energy, is 79 SNU [2]. Observation of significantly less than 79 SNU in a ^{71}Ga experiment is difficult to explain without invoking new neutrino properties.

1.5 Neutrino Oscillations

Neutrinos are electrically neutral, so that they have only weak (and gravitational) interactions. They may have finite masses, which should be zero in the standard model of elementary particle physics. However, if neutrinos are Majorana particles, their masses can be quite small. This idea was originally presented as the seesaw mechanism by T.Yanagida [33]. If a right-handed neutrino ν_R is introduced together with ν_L, they make mass eigenstates with Majorana mass M and $m^2/4M$, respectively, where m means a charged lepton mass. From the MSW solution which will be discussed later, the mass squared difference between ν_e and ν_μ is expected to be $10^{-2} \sim 10^{-3}$ eV, so that the ν_μ mass would be $10^{-3\pm0.5}$ eV, assuming the very small ν_e mass. Then the ν_τ mass could be around $10^{-2} \sim 1$ eV. Neutrino oscillations play an essential role in the solar neutrino physics if neutrinos masses are indeed in that range. Let us review the neutrino oscillations.

1.5.1 Neutrino Vacuum Oscillation

We assume two flavor oscillations between an electron neutrino (ν_e) and a muon neutrino (ν_μ). These eigenstates of the weak interaction are represented by a mixture of mass eigenstates (ν_1, ν_2) as follows [34];

$$\begin{pmatrix} \nu_e \\ \nu_\mu \end{pmatrix} = \begin{pmatrix} \cos\theta & \sin\theta \\ -\sin\theta & \cos\theta \end{pmatrix} \begin{pmatrix} \nu_1 \\ \nu_2 \end{pmatrix}, \tag{1.15}$$

where θ is the mixing angle. Let ν_i (i = e or μ) be generated at the time $t = 0$ and propagate in vacuum. Then the propagation obeys the Schrödinger equation;

$$i\frac{d}{dt}\begin{pmatrix} \nu_e \\ \nu_\mu \end{pmatrix} = H \begin{pmatrix} \nu_e \\ \nu_\mu \end{pmatrix}, \tag{1.16}$$

where H is the hamiltonian and the wave function at the time $t = t$ is expressed by;

$$\mid \nu_i(t) >= exp[-iHt] \mid \nu_i(0) > . \tag{1.17}$$

H is just the kinetic term and its eigenvalues are;

$$H_i = E_i = \sqrt{p^2 + m^2} \simeq p + \frac{m_i^2}{2p}, \tag{1.18}$$

where E_i and p show the neutrino energy and momentum, respectively, and $m_i \ll p$. The amplitude of conversion from initial state i to final state j is expressed as;

$$< \nu_j \mid \nu_i >= \sum_k U_{ik} U^*_{jk} exp[-iEt], \tag{1.19}$$

where U shows the mixing matrix in Eq.(1.15). The probability for a transition from the state $\mid \nu_i >$ to $\mid \nu_j >$ is;

$$P(\nu_i \to \nu_j) =\mid < \nu_j \mid \nu_i >\mid^2 = \sum_{k,l} U_{i,k} U^*_{j,k} U_{i,l} U^*_{j,l} exp[-i(E_k - E_l)]. \tag{1.20}$$

If the propagation length in the time interval of t is L, the probabilities are given as follows;

$$P(\nu_e \to \nu_e) = P(\nu_\mu \to \nu_\mu) = 1 - \sin^2 2\theta \sin\left(\frac{\pi L}{L_v}\right), \tag{1.21}$$

$$P(\nu_e \to \nu_\mu) = P(\nu_\mu \to \nu_e) = \sin^2 2\theta \sin\left(\frac{\pi L}{L_v}\right), \tag{1.22}$$

where L_v is the vacuum oscillation length and is defined as;

$$L_v \equiv \frac{4\pi E}{\Delta m^2}, \quad \Delta m^2 = m_2^2 - m_1^2. \tag{1.23}$$

A number of neutrino vacuum oscillation experiments have been carried out at reactors and at accelerators [35]. None of these experiments found evidence for neutrino oscillations. The excluded region on the oscillation parameter plane ($\sin^2 2\theta$,Δm^2) is shown in Fig.1.6. These experiments employ neutrinos with the ratio of the distance R measured in m to the energies E in MeV in the range of $R/E = 10^{-2}$–10^1 for accelerators and $R/E = 10^0 - 10^2$ for reactors (cf. $R/E = 10^{10} - 10^{11}$ for solar neutrinos). Therefore, the relevant mass difference lies in the range of 0.01 $\sim$ 10 eV^2.

The vacuum oscillations were claimed as a solution of the solar neutrino deficit. The solution exists in the region of $5 \times 10^{-11} \leq \Delta m^2 \leq 1.1 \times 10^{-10}$ eV^2 and $\sin^2 2\theta \geq 0.7$ [10][11] to account for both the KAM-II and the Homestake experiment.

1.5.2 Neutrino Matter Oscillations (MSW effect in the Sun)

When electron neutrinos propagate through matter instead of vacuum, they feel an extra potential energy of $\mathrm{V_e}$ in matter [10]. This potential energy is given by;

$$\begin{aligned} \mathrm{V_e} &= \sqrt{2}G_f N_e \text{ (charged current only)}, & (1.24)\\ \mathrm{V_e} &= \sqrt{2}G_f N_e + \sqrt{2}G_f[(2\sin^2\theta_W - \frac{1}{2})N_e + (-2\sin^2\theta_W + \frac{1}{2})N_p - N_n] & (1.25)\\ &\quad \text{(charged and neutral current)}, \end{aligned}$$

where G_f is the Fermi coupling constant, θ_W is the Weinberg angle, and N_e, N_p and N_n are the electron, proton and neutron number densities in the Sun, respectively. The neutrino evolution is expressed by the following equation;

$$i\frac{d}{dt}\begin{pmatrix} \nu_e \\ \nu_\mu \end{pmatrix} = H \begin{pmatrix} \nu_e \\ \nu_\mu \end{pmatrix}, \tag{1.26}$$

$$H = H_0 + \mathrm{V} \sim E + \frac{1}{2E}(M^2 + 2E\mathrm{V}), \tag{1.27}$$

where H_0 is the Hamiltonian in vacuum. The matrices V and M^2 in Eq.(1.27) are;

$$\mathrm{V} = \begin{pmatrix} \mathrm{V}_e & 0 \\ 0 & 0 \end{pmatrix}, M^2 = U^{-1} \begin{pmatrix} m_1^2 & 0 \\ 0 & m_2^2 \end{pmatrix} U, \tag{1.28}$$

where U is the mixing matrix. Note that we subtracted out the common potential energy for ν_e and ν_μ since it induces only a common phase factor which is irrelevant to observed phenomena. Thus the neutral-current contribution disappears and only the charged-current term remains. Now if the term A is defined as;

$$A = 2E\mathrm{V}_e = 2\sqrt{2}\mathrm{G_f}N_e E, \tag{1.29}$$

then the Hamiltonian can be expressed as follows;

$$H = \frac{1}{2E}(m_1^2 + m_2^2 + A) \begin{pmatrix} 1 & 0 \\ 0 & 1 \end{pmatrix} + \frac{1}{2E} \begin{pmatrix} A - \Delta m^2 \cos 2\theta & \Delta m^2 \sin 2\theta \\ \Delta m^2 \sin 2\theta & -A + \Delta m^2 \cos 2\theta \end{pmatrix}. \tag{1.30}$$

H is conveniently expressed as;

$$H = 2\pi \begin{pmatrix} \frac{1}{L_e} - \frac{\cos 2\theta}{L_v} & \frac{\sin 2\theta}{2L_v} \\ \frac{\sin 2\theta}{2L_v} & 0 \end{pmatrix}; \tag{1.31}$$

$$L_v = \frac{4\pi E}{\Delta m^2}, \quad L_e = \frac{\sqrt{2}\pi}{G_f N_e}. \tag{1.32}$$

If the electron density is not constant along the neutrino path, the matrix depends on time or position. Instantaneous eigenstate ν_{1m}, ν_{2m} can be represented by;

$$\begin{pmatrix} \nu_{1m} \\ \nu_{2m} \end{pmatrix} = \begin{pmatrix} \cos\theta_m & -\sin\theta_m \\ \sin\theta_m & \cos\theta_m \end{pmatrix} \begin{pmatrix} \nu_e \\ \nu_\mu \end{pmatrix}, \tag{1.33}$$

where θ_m is the effective mixing angle in matter and is defined by;

$$\sin^2 2\theta_m = \frac{\sin^2 2\theta}{\left[\sin^2 2\theta + \left(\frac{L_v}{L_e} - \cos 2\theta\right)^2\right]}. \tag{1.34}$$

If A is constant, in other words, the electron density is constant, the probability that neutrinos born as ν_e 's remain ν_e 's ,$\mathrm{P_m}(\nu_e \to \nu_e)$, at a distance L is written in a similar way to that of Eq.(1.21) in vacuum;

$$\mathrm{P_m}(\nu_e \to \nu_e) = 1 - \sin^2 2\theta_m \sin^2\left(\frac{\pi L}{L_m}\right), \tag{1.35}$$

where L_m is the oscillation length in the matter;

$$L_m = L_v \left[1 - 2\frac{L_v}{L_e}\cos 2\theta + \left(\frac{L_v}{L_e}\right)^2 \right]^{-\frac{1}{2}} . \tag{1.36}$$

If the following condition is satisfied,

$$L_v = L_e \cos 2\theta, \tag{1.37}$$

the resonance occurs and the amplitude of Eq.(1.34) becomes maximum as shown in Fig.1.7 even for the intrinsic mixing angle ($\sin^2 2\theta$) is small. This is the key point of the MSW effect. Numerically, the condition of Eq.(1.37) is rewritten by;

$$\frac{N_e}{N_A} \simeq 66 \times 10^5 \cos 2\theta \frac{\Delta m^2(\mathrm{eV}^2)}{E(\mathrm{MeV})}, \tag{1.38}$$

where N_A is Avogadro's number ($N_A = 6.02 \times 10^{23}$).

^{8}B solar neutrinos are produced at the core of the Sun as shown in Fig.1.8. They go out from high electron density region to the vacuum beyond the photosphere of the Sun. Figure 1.9 shows the electron density in the Sun as a function of radius calculated by Bahcall and Ulrich. If the neutrinos pass through the region where the condition of Eq.(1.37) is satisfied, they oscillate resonantly. Figure 1.10 shows an example of the survival probability $\mathrm{P}_m(\nu_e \rightarrow \nu_e)$ for ν_e created at the center of the Sun as a function of radius with $\sin^2 2\theta = 0.001$ and $E/\Delta \mathrm{m}^2 = 6\times 10^5$ MeV/eV^2. A clear resonance occurs at $R/R_\odot = 0.3$.

This resonant oscillation requires some conditions. At first, the resonant electron density has to be smaller than that of the center of the Sun ($\rho \sim 100$ gcm^{-3}), so neutrinos pass through the resonant region;

$$\Delta m^2 \cos 2\theta \leq 10^{-5} \times E \text{ [MeV]}. \tag{1.39}$$

If the gradient of electron density of the Sun at the resonant region is smaller than the oscillation length in matter (adiabatic condition);

$$\frac{1}{N_e}\left(\frac{dN_e}{dR}\right) \leq \frac{\Delta m^2 \sin^2 2\theta}{\cos 2\theta} \approx \frac{10^{-8}}{E}, \tag{1.40}$$

ν_e created at the center of the Sun satisfies the adiabaticity and the state follows the mass eigenstate $\mid \nu_2 >$, and finally ends up with $\mid \nu_\mu >$ at exit as shown in Fig.1.11.

There is another possibility. If the oscillation length in matter is sufficiently larger than the resonant width, the electron density changes so rapidly near the resonance that the flavor state can not adiabatically keep up with the mass eigenstate (non-adiabatic condition);

$$\frac{\Delta R}{L_{m,res}} = \frac{\Delta m^2 c^3 \sin^2 2\theta / \cos 2\theta}{2\pi\hbar \mid N_e^{-1} dN_e/dR \mid} \ll 1. \tag{1.41}$$

Then the transition from one mass eigenstate to another is dominant. The quantity of the probability of level crossing P_{jump} is calculated by using an approximation developed by Landau and Zenner in which the electron density varies linearly in the region near the resonant electron density, and represented as;

$$\begin{aligned} \mathrm{P}_{jump} &= exp[\frac{-\pi\Delta m^2 \sin^2 2\theta}{4E\cos 2\theta}(\frac{N_e}{\mid dN_e/dr \mid_{res}})], \; N_e > N_{res} \\ &= exp[-\frac{\pi^2(\Delta R)}{2L_{m,res}}]. \end{aligned} \tag{1.42}$$

Therefore, in the non-adiabatic limit, the probability P_{jump} is large and ν_e produced at the center of the Sun becomes finally ν_μ as shown in Fig.1.11. These two conditions define a triangular region on the oscillation parameter plane ($\sin^2 2\theta$, Δm^2).

Figure 1.12 shows the iso-SNU contour line (2 SNU) corresponding to the Homestake experiment. The horizontal line ($\Delta m^2 \sim 10^{-4}\mathrm{eV}^2$) and the vertical line represent solutions which satisfy the adiabatic criterion namely the width of resonance is large compared to the matter oscillation length. The diagonal line corresponds to a solution in which the level crossing probability is large.

^{8}B neutrino energy spectrum is distorted differently in the two regions. In the adiabatic region, lower energy neutrinos ($E \leq 5 \sim 7$MeV) are unaffected by the oscillation but higher energy neutrinos are strongly suppressed. On the other hand, in the non-adiabatic region, neutrinos in the whole energy range, especially in the low or intermediate energy range, are suppressed. More detailed description of the neutrino energy spectra will be given in Chapter 3.

1.5.3 Neutrino Regeneration in the Earth (Day/Night effect)

It is a natural idea that there should exist a matter oscillations in the Earth when the matter oscillations occur in the Sun. Electron neutrinos (ν_e's) which are oscillated out in the Sun may oscillate back in the Earth to their initial state of ν_e. In the adiabatic case, the wave function of neutrinos at the surface of the Sun is given by [36];

$$| \nu_2 >= \sin\theta \mid \nu_e > + \cos\theta \mid \nu_\mu > . \tag{1.43}$$

If the mixing angle ($\sin^2\theta$) is small, the $| \nu_2 >$ state is almost equal to the $| \nu_\mu >$, so ν_e is completely converted to ν_μ. However, $| \nu_e >$ can be regenerated by the neutrino matter oscillation in the Earth. Figure 1.13 shows the radial distribution of terrestrial density [37]. The resonant condition in this case is expressed as follows;

$$\frac{E(\mathrm{MeV})}{\Delta m^2(\mathrm{eV}^2)} \approx \frac{7 \times 10^6}{\rho(\mathrm{g/cm}^3) y_e} \cos 2\theta, \tag{1.44}$$

where ρ is the density of the matter and y_e is the number of electrons per amu ($y_e \sim 1/2$) [38]. For example, if the neutrino energy is 10 MeV, the oscillation parameters of $\Delta m^2 \sim 10^{-6}$ eV^2 and $\sin^2 2\theta \geq 0.1$ satisfy this condition. If $\sin^2 2\theta < 0.1$, the matter oscillation length becomes so long that no ν_e regeneration occurs.

For ^{8}B solar neutrinos, the regeneration effect in the Earth is expected in a region of $\Delta m^2 \leq 3 \times 10^{-6}$ eV^2 and $\sin^2 2\theta \geq 0.2$ for KAM-II ($E_e > 7.5$ MeV). If this is indeed the case, the event rate will differ between day and night. This regeneration effect is known as the Day/Night effect.

Chapter 2

THE KAMIOKANDE-II DETECTOR

2.1 Detector

The KAMIOKANDE-II (KAM-II) detector is an imaging water Čerenkov detector located 1000 m underground (2700 m water equivalent) in the Kamioka zinc mine in the Gifu prefecture of Japan, at 36.4°N, 137.3°E and 25.8°N geomagnetic latitude.

The detector consists of an main inner counter which detects physical phenomena and an outer anticounter. A schematic view of the detector is shown in Fig.2.1. The inner counter is contained in a cylindrical steel tank of 14.4 m in diameter × 13.1 m in height, containing 2142 metric tons of water. A total of 948 PMTs with 50 cm ϕ photo-cathode area cover 20% of the entire inner surface of the tank. The fiducial mass for the solar neutrino measurement is 680 tons, with boundaries 2.0 m (3.14 m) from the barrel and the bottom wall (the top wall). A 4π solid-angle anticounter surrounding the inner counter is also a water Čerenkov counter of total mass 1800 metric tons with 123 PMTs (21 on the bottom, 22 on the top, and 80 on the barrel) to detect any particles from outside to the inner counter and to shield against gamma-rays and neutron from outside the detector. The mean thickness of the water in the anticounter is 1.2 m, 0.8 m and 1.7m for the bottom, top and barrel section, respectively.

2.2 Water and Air Purification

There are several kinds of dusts in the water such as bacteria or heavy metal ions (F^{++}, Ni^{++}, Co^{++}) and so on. They make water transparency worse due to their absorption and cause loss of Čerenkov photons (see Fig.2.2). Therefore, the water transparency should be maintained at a high, constant value (attenuation length $\gtrsim$ 60 m) to minimize the loss of Čerenkov photons. In order to achieve the goal, the water is continually circulated through a purification system, even if the relative temperature ($\sim$ 11° C) of the water helps to prevent proliferation of bacteria. The another important background is radioisotopes in the detector water. At low energies, they dominate the trigger rate. The irremoval of them is one of the most important functions of the purification system. Special modifications were made to the purification system to remove heavy radioactive elements from the water, so that the level of radioactivity has been low enough to allow the solar neutrino data to be taken since January, 1987. Furthermore, air-tightening of the detector itself and of the water purification system, which was in place by the Spring of 1987, reduced the radioactive background from radon (Rn) in the air dissolving into the water of the detector.

The water purification system consists of the following part as shown in Fig.2.3; (a) 5 membrane filters; (b) a degasifier, (c) an ultra-violet sterilizer to destroy bacteria; (d) ion-exchange columns for removing uranium (CR-55); (e) a mixed-bet-type deionization system and (f) pumps. Water is circulated through the bottom anticounter, the inner counter, the top anticounter and the purification system. The flow rate is 4.5 tons per hour.

This system has reduced the uranium and radium content in the water to a level at less than 10^{-3} pCi/l, and suppressed the equilibrium radon content in the tank water by a factor of 10^3 relative to the water in the mine.

2.3 Electronics and Data Acquisition

The electronics is designed to implement multihit time and charge measurement of all PMTs in the detector, and to allow new trigger configuration to be set for a variety of physical events. The circuit reduces the dead time of the system to nearly the limit caused by the PMT recovery time (less than 50 nsec), and increases the ability of the detector to record a lot of event such as burst without events losing.

The block diagram of electronics is shown in Fig.2.4. The electronics system is organized into 272 boards of front end cards, each card has 4 channels of signal and 16 cards make a crate. Each crate for inner detector (total 15 crates) contains one trigger processing card and one control card. Each crate for anticounter contains only a control card, so that the information from this card is only used off-line. The control card continuously cycles through the channels in the crate searching for flags indicating the presence of signal to be digitized. When a channel flag is recognized, the time and charge are digitized and stored with the event number in a 512 word deep FIFO memory on the control card. When the event trigger occurs, the time and the event number are established by a timing card. A PDP 11/73 computer reads the time, and drains the FIFO (First in first out) memories in each control card until all of the memories in the crate are empty. The PDP 11/60 (replaced by a μ-VAX early in 1989) reads the information from the 11/73 and records the data on magnetic tape.

2.4 Event Trigger and Trigger Efficiency

The trigger system is designed to collect all events above approximately 6 MeV without dead time. If the PMT signal passing through the amplifier is above the threshold of approximately 0.18 photoelectron, which is controlled by the PDP 11/73, a rectangular discriminator output of $\sim$ 100 nsec width and $\sim$ 5 mV pulse height is produced and transmitted over the backplane of a crate to the trigger card in the same crate. The trigger card in each crate sums the 64 channels of discriminator outputs to make an analog pulse, and master trigger card finally sums the outputs from the 15 trigger cards. An event trigger is generated when the peak value of the final analog pulse is above the trigger threshold which is adjustable and set to 112 mV corresponding to $\sim$ 17 hits of PMT at the single photoelectron level. The trigger threshold was lowered to 100 mV in October, 1987 to take advantage of low trigger rate, then it was changed again to 112 mV in June, 1988 when the PMT gain was doubled. Note that the anticounter information is not taken into account in the event trigger formation, but it is useful to veto events such as cosmic ray muons, gamma-rays and neutrons from the outside rock in the off-line data reduction analysis.

The trigger efficiency as a function of electron total energy is obtained from Monte Carlo and shown in Fig.2.5. The initial trigger accepted 7.6 MeV (10 MeV) electrons with 50% (90%) efficiency over the 680 metric ton fiducial volume of the detector with a 112 mV trigger threshold. After October, 1987 and before the PMT gain doubling in June, 1988, the trigger accepted 6.7 (9.2) MeV electrons with 50% (90%) efficiency with 100 mV trigger threshold. After the gain doubling, the efficiency became 50% for 6.1 MeV electrons and 90% for 9.0 MeV electrons over the fiducial volume. The time dependence of trigger threshold (50% efficiency) is shown in Fig.2.6. The total rate of triggers in the detector was, for example since May 1989, $\sim$ 5 Hz at 5.2 MeV and $\sim$ 1 Hz at 6.1 MeV threshold, of which 0.37 Hz is due to cosmic ray muons. The remaining trigger rate is presumably due to radioactivity in the water of the inner detector such as the beta decay of ^{214}Bi (end point energy 3.26 MeV) or a daughter of ^{222}Rn, and in the detector materials.

2.5 Calibration

To observe the solar neutrinos clearly, it is necessary to understand the detector response such as detection energy, interaction (vertex) position, and direction of event. The main information obtained from the data acquisition system are digitized time and charge information of hit PMTs. The PMT timing information and the Čerenkov pattern of event are vital for reconstruction of the vertex position and direction of low energy electrons. The energy of scattered electrons is estimated using the number of hit PMTs. Therefore, an accurate calibration of the each PMT's response is necessary.

2.5.1 Energy Calibration

The low energy electrons scattered by incident neutrinos in the detector emit the Čerenkov light with a total intensity proportional to its total energy of the charged particle. In the energy range of the events discussed here ($\leq$ 15 MeV), a typical PMT response corresponds to the detection of one photoelectron. Thus, the energy of low-energy electrons can be estimated by an appropriate sum of the number of hit PMTs which respond to the signal.

In fact, the response of the detector depends on an attenuation of the Čerenkov light by absorption in water and the geometrical effect arising from event vertex position and the location of the PMTs. The number of hit PMTs corrected for these effect is expressed by the effective number of hit PMTs (N_{eff}), which is described in Appendix D. An electron of 10 MeV total energy gives an average 26 and 30 N_{eff} before and after the gain doubling, respectively. Thus, the total electron energy, E_e in MeV, of each event is estimated simply by dividing N_{eff} by 2.6 (3.) for the data of before (after) the gain doubling.

The energy calibration of the detector is performed using three independent methods. The first method uses gamma rays from a Ni thermal neutron capture reaction. The second method makes use of the continuous energy distribution of decay electrons from stopping cosmic ray muons. The third method makes use of beta spectra of radioactive nuclei(end point energies of 10 - 17 MeV) which are produced by spallation induced by cosmic ray muons. An detailed explanations are described as follows.

Ni-Cf Gamma-ray Calibration Gamma-rays emitted from the thermal neutron capture reaction by Nickel, Ni(n,γ)Ni, is used for the energy calibration. The energies of 9.0 7.8 and 6.8 MeV are released in fraction of 0.71, 0.16 and 0.13, respectively, where these values are given by the mass fraction and cross section for thermal neutron capture for each Nickel isotope. The calibration system utilizes ^{252}Cf as a neutron source. The calibration system is shown in Fig.2.7, which is enclosed in a water-filled nickel can with 9.5 cm in diameter, 16 cm in height and 1 mm in thickness. The amount of ^{252}Cf is 97 μCi in activity and it emits 4.6×10^5 neutrons per second at $\sim$ 2MeV which are slowed by interactions with the water in the nickel can.

Since ^{252}Cf itself emits gamma-rays, it needs to subtract them from the calibration data. Two sets of data are taken: one with ^{252}Cf only (without a nickel can) and the other with ^{252}Cf and Ni. The N_{eff} distribution of gamma-rays from the neutron capture reaction in Ni is obtained by subtraction and is shown in Fig.2.8. Also the same distribution obtained by the Monte Carlo simulation which was tuned to reproduce the peak of N_{eff} distribution of the ^{252}Cf/Ni calibration data within ± 1% is shown in Fig.2.9. The calibration yields;

$$\frac{\text{Monte Carlo}}{\text{Real Data}} = 1.000 \pm 0.01 \tag{2.1}$$

The shape of the obtained spectrum in Fig.2.9, in particular the width, which represents the energy resolution, is well reproduced by the Monte Carlo simulation. This ^{252}Cf/Ni calibration was performed by placing the source at various places in the detector fiducial volume. The Monte Carlo simulation reproduces the peak position of the N_{eff} distribution within ± 2% for these calibration data. The stability of the detector gain was monitored using ^{252}Cf/Ni calibration. The relative gain variation is shown in Fig.2.10. The gain is stable within ± 2% during 4 years of operation from 1987 to 1990.

Stopping Muon Decay Electrons from the stopping-muon decay are also used as an energy calibrator in a somewhat high energy range ($\sim$ 30 MeV). Comparison of the N_{eff} distribution between the measured data and the Monte Carlo simulation of the well-known muon decay (Michel) spectrum is shown in Fig.2.11 and yields,

$$\frac{\text{Monte Carlo}}{\text{Real Data}} = 1.011 \pm 0.03. \tag{2.2}$$

Spallation Event Beta-decays from high energy cosmic ray muon induced spallation products were obtained in conjunction with the information on the preceding muons.

The Monte Carlo events were generated to simulate the beta-decay of the short lived isotopes; ^{12}B ($\tau_{1/2}$ = 20.3 msec, E_{max} = 13.37 MeV) and ^{12}N ($\tau_{1/2}$ = 11.0 msec, E_{max} =16.38 MeV) in the ratio, 0.85:0.15, which accounted for an obtained half-life of 18.4 ± 0.8 msec shown in Fig.2.12. Comparison of the observed N_{eff} distribution of beta-rays from the short lived isotopes and the Monte Carlo simulation is shown in Fig.2.13 and gives;

$$\frac{\text{Monte Carlo}}{\text{Real Data}} = 0.98 \pm 0.01. \tag{2.3}$$

Combining the result of above three independent energy calibrations, one obtains;

$$\frac{\text{Monte Carlo}}{\text{Read Data}} = 1.00 \pm \lesssim 0.03, \tag{2.4}$$

so that the uncertainty in the absolute energy calibration is estimated to be less than 3%. This uncertainty is considered in the systematic error of obtained neutrino flux as described in the section 4.4. The energy resolution for low energy electrons is shown in Fig.2.14 before and after the gain doubling. The typical values of $\sigma(E_e)/E_e$ for after gain doubling are 21% at 8.5 MeV, 20% at 10.0 MeV and 18% at 15.0 MeV. The energy resolution after the gain doubling is approximately given by following formula;

$$\frac{\sigma(E_e)}{E_e} = \frac{20\%}{\sqrt{E_e/10\text{MeV}}}, \tag{2.5}$$

where E_e is the electron total energy in MeV.

The angular resolution of the detector was calibrated using a collimator with the Ni(n,γ)Ni source placed at the top of the detector. The observed data and the Monte Carlo simulation (EGS version 4) are shown in Fig.2.15. The angular resolution of the detector (σ_θ) is limited by multiple Coulomb scattering of electrons in water, so that this calibration indicates the validity of the simulation of the propagation for electrons and gamma-rays in water. The electron energy dependence of the angular resolution is shown in Fig.2.16 before and after the gain doubling and is expressed as;

$$\sigma_\theta(E_e) = \frac{28\text{deg}}{\sqrt{E_e/10\text{MeV}}}. \tag{2.6}$$

2.5.2 Timing Calibration

The timing calibration corrects for the variation of time response as a function of pulse amplitude, for the time delay due to the different high voltage applied to the PMT, and for the different cable lengths for the individual channels so that overall time synchronization may be achieved. The synchonization is described by calibration constants associated with the electronics and other constants associated with the remainder of the detector.

The timing calibration is achieved by a system which utilizes a nitrogen gas laser as a light source. It emits a light pulse with a wavelength of 337 nm with less than 3 nsec duration. A quartz plate splits the light pulse into two: one goes to PIN-diodes for the electronics trigger, and the other goes through a 6-bit attenuator. A combination of six attenuator components changes the intensity of the light from a few tenth of single photoelectrons to a few hundreds of photoelectrons in the tank. The laser light is guided along a long optical fiber to a diffusion ball which makes the light reasonably isotropic. Timing calibration data are taken with the diffusion ball at the center of the detector to synchronize all PMTs. Data which calibrate the electronics alone are taken by activating the discriminator of each channel with a test pulse from the timing cards and by stopping the activation with a delayed global trigger.

The time response as a function of pulse height, which is called as T-Q map, is obtained from the calibration data for each PMT channel. Timing calibration constants are calculated by determining the characteristic function for each obtained time response as a function of pulse height.

2.5.3 Calibration of Vertex Position Resolution

The range of a 10 MeV electron in water is about 5 cm, so that it is almost pointlike in the detector. The origin of an electron event is determined by reconstructing the vertex of Čerenkov cone utilizing relative timing and pulse height information from the hit PMTs.

For the best estimation of the vertex position, residual time of each hit PMT was calculated by subtracting the time of flight from the measured time. Fig.2.17(a) shows its distribution for one event, sharply peaked at zero when a correct vertex position is found. On the other hand, an incorrect vertex position leads to a broad distribution as shown in Fig.2.17(b).

The vertex position resolution was calibrated by gamma-rays from the Ni(n,γ)Ni source. The data were taken with the calibration source at the center of the detector and at other positions in the fiducial volume. The positions of the source were well reproduced by the reconstructed vertex position within 10 cm in each coordinate and were consistent with a Monte Carlo simulation. No systematic bias was found in the vertex reconstruction.

The vertex position resolution was obtained from the 1 standard deviation of the reconstructed position relative to the location of the source. The measured vertex position resolution of gamma-rays is shown in Fig.2.18 as a function of energy, and is compared with that of the Monte Carlo simulation. However, the resolution for electrons is much better because of conversion length of gamma-rays in water ($\sim$ 40 cm). The Monte Carlo simulation tuned for the gamma-ray calibration data was used to estimate the vertex position resolution of electrons. It is shown in Fig.2.19 and obtained as 1.2 m and 1.0 m for 10 MeV electrons for the data before and after the gain doubling, respectively.

2.6 Expected Signature

The neutrino energy spectrum of ^{8}B decay is given by the SSM prediction [39], and the cross section of ν_e e$^-$ scattering is provided by precise measurement of electroweak parameter. Hence, the energy distribution of the final state electrons can be calculated precisely. The response of the detector is obtained from the Monte Carlo simulation, in which the detailed detector properties of each component are taken into account. Thus, the expected energy distribution of recoil electrons can be obtained by the Monte Carlo simulation. The expected event rate for ^{8}B neutrinos is 0.86 events per day per 680 ton for $E_e \geq 7.5$ MeV, and 0.28 (0.29) events per day per 680 ton for $E_e \geq 10$ MeV for after (before) the gain doubling, when the calculation of Bahcall and Ulrich is used [1], and 35% lower when the calculation of Turck-Chièze et al [41] is used. The slight decrease ($< 3\%$) in the event rate after the gain doubling is due to the improvement in the energy resolution.

In the case of the neutrino oscillations, the expected energy spectrum of recoil electrons is different from the one predicted by SSM, and depends on the oscillation parameters ($\sin^2 2\theta$,Δm^2). Thus, it should be calculated in each case by the simulation program. The more detailed explanation of the simulation with the neutrino matter oscillations in the Sun and in the Earth will be described in the next chapter.

Chapter 3

Event Simulation

3.1 Calculation of the MSW Effect in the Sun

If neutrino matter oscillations occur in the Sun, an electron neutrino (ν_e) which is generated inside the Sun might be converted to a muon neutrino (ν_μ) as described in section 1.5. The survival probability for an electron neutrino, $P(\nu_e \rightarrow \nu_e)$, depends on both mixing angle θ and $E/\Delta m^2$ (MeV/eV^2), where E and Δm^2 are the neutrino energy and mass squared difference, respectively. Therefore, the calculation of the probability $P(\nu_e \rightarrow \nu_e)$ must be carried out at each point of the mixing angle and the mass squared difference.

In the first place, the data base of the electron neutrino survival probability is made by calculating on the oscillation parameter ($\sin^2 2\theta$,$E/\Delta m^2$) plane. The area specified by $10^{-4} \leq \sin^2 2\theta \leq 1$ and $10^4 \leq E/\Delta m^2 \leq 10^9$ MeV/eV^2 is divided into 41 × 251 grid points. For each grid, an exact numerical integration was employed for the calculation of the probability along the neutrino path through the Sun where the electron density varies and no approximate analytic calculation was used. The calculation was performed by the following steps.

1. An electron neutrino is produced at the center of the Sun.
2. The propagation of the neutrino is calculated by numerical integration from the center of the Sun to its surface.

3. The calculation is continued from the surface of the Sun up to the position of one vacuum oscillation length far away from the surface. During this step, the neutrino survival probability at every calculating points is recorded.

4. Averaging of the recorded probabilities;

$$\mathrm{P}(\nu_e \rightarrow \nu_e) = \frac{1}{2} \times (\mathrm{P}_{max} + \mathrm{P}_{min}),$$

   where P_{max} and P_{min} are the maximum and minimum values of the recorded probability, because the distance from the Sun to the Earth changes maximally by about 5×10^9 m due to the eccentricity of the Earth orbit (1.5×10^{11} m), which is much longer than a typical vacuum oscillation length (cf. $L_v = 2.5 \times 10^7$ m for $E/\Delta m^2 = 10^7$ MeV/eV^2) where the MSW effect is very effective.

Moreover, in the adiabatic region, it is necessary to take into account the position where neutrinos are originally generated, because the level crossing occurs near the center of the Sun (cf. $R \sim 0.05R_\odot$ for $\sin^2 2\theta = 0.1$ and $E/\Delta m^2 = 6.3 \times 10^4$ MeV/eV^2). The production point distribution of ^{8}B solar neutrinos is shown in Fig.1.8 as a function of solar radius. The probability $\mathrm{P}(\nu_e \rightarrow \nu_e)$ depends on the generation point even for the same neutrino energy. The probability in the adiabatic solution, in fact, is calculated for each point of $\sin^2 2\theta$ in the range of $10^{4.7} \leq E/\Delta m^2 \leq 10^{5.1}$ (MeV/eV^2). The spatial distribution of the production points is divided into 30 different points, which are at $\mid R/R_\odot \mid$ = 0.01, 0.03, 0.05, 0.07, 0.09 and 0.11 for each $\cos\Theta$ = -0.8, -0.4, 0.0, 0.4 and 0.8, where R is the distance from the center of the Sun, $R_\odot$ is the solar radius and Θ is the zenith angle. The probability $\mathrm{P}(\nu_e \rightarrow \nu_e)$ is determined by averaging the values obtained at each point with a weight of radial distribution of the production rate.

On the other hand, in the non-adiabatic region, the level crossing occurs in the outer region of the Sun (cf. $R \sim 0.3R_\odot$ for $\sin^2 2\theta = 0.01$ and $E/\Delta m^2 = 6 \times 10^5$ MeV/eV^2). The production point of ^{8}B solar neutrinos is, therefore, assumed to be located at the center of the Sun. Then, the probability $\mathrm{P}(\nu_e \rightarrow \nu_e)$ is given just by averaging the values obtained after the level crossing.

Now, the electron neutrino survival probability $\mathrm{P}(\nu_e \rightarrow \nu_e)$ at every oscillation parameter on ($\sin^2 2\theta$,$E/\Delta m^2$) is calculated from the center of the Sun to its surface.

The final step is to chase $P(\nu_e \rightarrow \nu_e)$ from the solar surface to the detector on the Earth. Outside the Sun, however, the neutrino oscillation obeys the vacuum criterion. The vacuum oscillation length at these oscillation parameters is much shorter than the changing distance from the Sun to the Earth due to the eccentricity of the Earth orbit. Hence, the probability can be obtained just by averaging the maximum and minimum values of the probability which are calculated at the outside of the Sun.

Figure 3.1 shows the probability $P(\nu_e \rightarrow \nu_e)$ in a typical case of $\sin^2 2\theta = 0.1$, 0.01 and 10^{-3} as a function of $E/\Delta m^2$ (MeV/eV^2), respectively. The energy distribution of ^{8}B neutrinos at every oscillation parameter of $(\sin^2 2\theta, \Delta m^2)$ plane at the surface of the Earth is obtained by following calculation;

$$f_B(E_\nu) = \Phi_B(E_\nu) \times P(\nu_e \rightarrow \nu_e), \tag{3.1}$$

where $\Phi_B(E_\nu)$ shows the energy distribution of ^{8}B solar neutrinos predicted by SSM. Figure 3.2 shows the energy spectra in a typical case of adiabatic, non-adiabatic and large-mixing-angle solutions which correspond to $(\sin^2 2\theta, \Delta m^2) = (2 \times 10^{-3}, 1.3 \times 10^{-4})$, $(1.6 \times 10^{-2}, 3.2 \times 10^{-6})$ and $(0.8, 3.2 \times 10^{-6})$, respectively. The original energy spectrum of ^{8}B solar neutrinos without neutrino oscillations is also shown in Fig.3.2. In the figure, one notices a conspicuous difference in shape. In the adiabatic solution, higher-energy neutrinos are efficiently suppressed (converted), while in the non-adiabatic solution, lower-energy neutrinos are preferentially converted and higher-energy ones partially suppressed. In the large-mixing angle solution, neutrinos in the whole energy range are converted.

3.2 Calculation of Neutrino Regeneration Effect in the Earth

When the MSW solution is discussed, it is also necessary to consider the regeneration effect induced by neutrino oscillations in the Earth. The complete calculation of the neutrino survival probability, $P(\nu_e \rightarrow \nu_e)$, must be performed from the center of the Sun to the entrance of the detector through the Earth. The exact calculation is made by the following steps.

1. An electron neutrino is produced at the center of the Sun.
2. The propagation of the neutrino is calculated from the center of the Sun to its surface.
3. The calculation is continued from the surface of the Sun up to the position one vacuum oscillation length away from the surface of the Sun. During this step, the neutrino wave function at every $0.1 \times L_v$ was recorded as Ψ_i (i=1,10).
4. The propagation of the neutrinos from the surface of the Earth to the detector is calculated with the initial wave function of Ψ_i (i=1,10). The probability, $\mathrm{P}_i(\nu_e \to \nu_e)$, is calculated for each initial wave function.
5. Averaging of P_i (i=1,10);

$$\mathrm{P}(\nu_e \to \nu_e) = \frac{1}{10} \times \sum_{i=1}^{10} \mathrm{P}_i(\nu_e \to \nu_e).$$

The steps of 1 ~ 3 are similar to those of the MSW effect in the Sun as described in the previous section. In the step 1, one does not have to take into account the spatial distribution of production point for ^{8}B neutrinos, because the position in the Sun where the resonant condition is satisfied is far away from the production points of ^{8}B neutrinos (cf. $R/R_\odot = 0.4$ for $\sin^2 2\theta = 0.1$ and $E/\Delta m^2 = 2 \times 10^6$ MeV/eV^2). Thus, the neutrino propagation from the surface of the Earth to the entrance of the detector was calculated by the numerical integration using the initial wave function obtained by the step 3.

The solution of neutrino regeneration in the Earth satisfies the the adiabatic criterion. Therefore, a simple analytic expression of initial wave function (Eq.(1.43)) is useful. In fact, the obtained probability by above steps is almost the same as the one using the approximate expression of Eq.(1.43). Therefore, all of the probabilities $\mathrm{P}(\nu_e \to \nu_e)$ in the Earth are calculated by using this expression of initial wave function.

Numerical integration in the Earth is similar to that of the MSW effect in the Sun. The density distribution in the Earth is shown in Fig.1.13. In this case, the regeneration effect of ν_e , which is converted to ν_μ by the MSW effect in the Sun should depend on its path length to the detector as well as the density gradient in the Earth. Therefore, the calculation of the probability $\mathrm{P}(\nu_e \to \nu_e)$ is performed at every oscillation parameter of ($\sin^2 2\theta$,$E/\Delta m^2$) for 21 cases of $\cos\delta_{sun} = 0.05$ - 1.0 with 0.05 pitch, where δ_{sun} is the angle between the neutrino direction to the Earth and z-axis of the detector with $\cos\delta_{sun} < 0$ corresponding to daytime. Figure 3.3 shows the neutrino survival probability as a function of $R/R_\oplus$, where $R_\oplus$ is the radius of the Earth, in case of $\cos\delta_{sun} = 1$, $\sin^2 2\theta = 0.1$ and $E/\Delta m^2 = 2 \times 10^6$ (MeV/eV^2). Also, the survival probability is shown as a function of the $E/\Delta m^2$ in Fig.3.4 for $\sin^2 2\theta = 0.1$.

The calculation above is performed in the region of the oscillation parameters of $10^{-2} \le \sin^2 2\theta \le 1$ and $10^5 \le E/\Delta m^2 \le 10^8$ (MeV/eV^2) which is divided into 41 × 151 mesh points with each point having 21 probabilities according to the value of $\cos\delta_{sun}$.

3.3 Simulation of Detector Response

The KAM-II detector observes energy and direction of recoil electrons scattered by neutral-current interactions of ν_e ν_μ or ν_τ and by charged-current interactions of ν_e as shown in Fig.3.5. The differential cross sections of these interactions in the laboratory system are given by [40];

$$\frac{d\sigma}{dy} = \frac{G_f^2 m_e E_\nu}{2\pi}[\mathrm{A}_0 + \mathrm{B}_0(1-y)^2 - \mathrm{C}_0 m_e y/E_\nu] \tag{3.2}$$

$$y \equiv T_e/E_\nu, T_e = E_e - m_e,$$

where G_f, E_ν, T_e, E_e and m_e are the Fermi coupling constant, incident neutrino energy, scattered electron kinetic energy and electron total energy, and electron mass, respectively, and A_0, B_0 and C_0 are constants.

For ν_μ and ν_τ , these constants are given by;

$$\begin{aligned}
\mathrm{A}_0 &= (g_V + g_A)^2, && (3.3)\\
\mathrm{B}_0 &= (g_V - g_A)^2, && (3.4)\\
\mathrm{C}_0 &= g_V^2 - g_A^2, && (3.5)\\
g_V &= 2\sin^2\theta_W - \frac{1}{2}, && (3.6)\\
g_A &= -\frac{1}{2}, && (3.7)
\end{aligned}$$

where θ_W is the Weinberg angle. The differential cross section of ν_e is given by the following replacement,

$$g_V \rightarrow g_V + 1, \tag{3.8}$$

$$g_A \rightarrow g_A + 1, \tag{3.9}$$

because the contribution of the charged current interaction must be taken into account.

The total cross section is given by integrating the differential cross section Eq.(3.2);

$$\sigma_{total} = \frac{G_f^2 m_e E_\nu}{2\pi}[\mathrm{A}_0 y_{max} + \frac{\mathrm{B}_0}{3}[1-(1-y_{max})^3] - \mathrm{C}_0\frac{m_e y_{max}^2}{2E_\nu}], \tag{3.10}$$

where y_{max} shows the kinematical upper limit of the recoil electron energy as follows;

$$y_{max} = \frac{2E_\nu}{2E_\nu + m_e}. \tag{3.11}$$

Since the value of $\sin^2\theta_w$ has been determined to be 0.23, the total cross sections are calculated by;

$$\begin{aligned}\sigma_{total}(\nu_e e^-)\ [\mathrm{cm}^2] &= 4.31\times10^{-45}E_\nu[2.13y_{max} + 0.07\times(1-(1-y_{max})^3) \\ &\quad - 0.67\times\frac{m_e y_{max}}{2E_\nu}], \qquad (3.12)\\ \sigma_{total}(\nu_\mu\ or\ \nu_\tau e^-)\ [\mathrm{cm}^2] &= 4.31\times10^{-45}E_\nu[0.29y_{max} + 0.21\times(1-(1-y_{max})^3) \\ &\quad + 0.25\times\frac{m_e y_{max}}{2E_\nu}], \qquad (3.13)\end{aligned}$$

where E_ν is the neutrino energy in MeV. As seen in Eq.(3.12) and (3.13), the total cross section of the ν_μ or ν_τ is approximately six times smaller than that of ν_e .

The energy distribution of the recoil electrons scattered by solar neutrinos is given by the following expression;

$$\begin{aligned}F(T_e)dT_e &= [\int_{E_{\nu min}}^{E_{\nu max}}\Phi(E_\nu)\frac{d\sigma(E)}{dy}\frac{dy}{dT_e}dE_\nu]dT_e, \qquad (3.14)\\ E_{\nu min} &= \frac{1}{2}[T_e + [T_e(T_e+2m_e)]^{1/2}], \qquad (3.15)\end{aligned}$$

where $\Phi(E_\nu)$, $E_{\nu max}$ and $E_{\nu min}$ show the energy distribution of ^{8}B solar neutrinos predicted by the standard solar model, the maximum energy of ^{8}B solar neutrinos, and the minimum neutrino energy when the electron is scattered in the forward direction of the incoming neutrino, respectively.

In case of neutrino oscillations, the contribution of ν_μ must also be considered. Then the differential cross section in Eq.(3.14) is modified as;

$$\frac{d\sigma}{dy} = \mathrm{P}(\nu_e \rightarrow \nu_e)\frac{d\sigma_{\nu_e}}{dy} + [(1 - \mathrm{P}(\nu_e \rightarrow \nu_e)]\frac{d\sigma_{\nu_\mu}}{dy}, \tag{3.16}$$

where $\mathrm{P}(\nu_e \rightarrow \nu_e)$ is the survival probability and $d\sigma_{\nu_e}/dy$, $d\sigma_{\nu_\mu}/dy$ are the differential cross sections of the $\nu_e e^-$, $\nu_\mu e^-$ scattering, respectively. The survival probability $\mathrm{P}(\nu_e \rightarrow \nu_e)$ is a function of the oscillation parameters of $\sin^2 2\theta$ and $E/\Delta m^2$ (MeV/eV^2). The integration of Eq.(3.14) is performed for each oscillation parameter ($\sin^2 2\theta$,Δm^2) according to the energy spectrum of ^{8}B neutrinos.

In order to introduce the response of the detector into the calculation, the energy resolution and the trigger efficiency must be taken into account. The energy resolution can be approximately expressed as follows;

$$\frac{\sigma(E_e)}{E_e} = \frac{\sigma_0}{\sqrt{E_e/10\mathrm{MeV}}}, \tag{3.17}$$

where σ_0 is the experimentally measured energy resolution of 22 (19.5)% at 10 MeV before (after) the gain doubling, E_e is the recoil electron energy in MeV. The trigger efficiency is given by Fig.2.5 as a function of electron total energy.

The energy distribution without the effect of the trigger efficiency expected in the detector is given by the following equation;

$$F'(T_e')dT_e' = [\int_0^{T_{emax}} \frac{1}{\sigma(T_e)\sqrt{2\pi}} exp(-\frac{(T_e - T_e')}{2\sigma^2(T_e)}) \times F(T_e)dT_e]dT_e', \tag{3.18}$$

where $\sigma(T_e)$ is the energy resolution as the function of electron kinetic energy, T_{emax} is the kinematical upper limit of recoil electron energy. The expected recoil electron energy spectrum is shown in Fig.3.6. The calculation is performed for two conditions before and after the gain doubling, and then the two calculations are combined. Figure 3.7 shows the normalized energy distribution in case of neutrino oscillations with $(\sin^2 2\theta, \Delta m^2)=$ $(6.3 \times 10^{-1}, 10^{-4})$ for the solid line, $(10^{-2}, 3.2 \times 10^{-6})$ for the dotted-dashed line and $(2 \times 10^{-3}, 1.4 \times 10^{-4})$ for the dashed line, which correspond to the large-mixing angle, non-adiabatic and adiabatic solution, respectively, when the ratio of the expected energy distribution in the neutrino oscillations to the one without neutrino oscillations is shown. The observed energy distribution (discussed in the next chapter) is also shown in Fig.3.7

with the data point. The difference in shape is clearly seen in these spectra. The spectrum of the adiabatic solution in Fig.3.7 is suppressed in higher-energy region, and other spectra are almost uniformly suppressed over the whole energy range observed by KAM-II.

The effect of trigger efficiency as shown in Fig.2.5 must also be considered. The trigger efficiency is 97% at $E_e = 9.3$ MeV (75% at $E_e = 7.5$ MeV) before (after) the gain doubling. In practice, the effect of the trigger efficiency is considered as follows;

$$F''(T_e) = F'(T_e) \times \epsilon(T_e), \tag{3.19}$$

where $\epsilon(T_e)$ is the trigger efficiency as a function of recoil electron kinetic energy.

In case of the simulation for the neutrino regeneration effect in the Earth, it is necessary to calculate the number of expected events as a function of $\cos\delta_{sun}$, where δ_{sun} has been defined as the angle between the neutrino direction to the Earth and z-axis of the detector with $\cos\delta_{sun} < 0$ corresponding to daytime. The number of expected events is calculated by integrating Eq.(3.18) over the kinetic energy range of recoil electron and expressed as $N_{MSW,\delta}(E_i,P_j)$, where E_i is the i-th electron energy bin in 0.5 MeV, P_j is the indicator of data whether before or after the gain doubling, and δ shows the $\cos\delta_{sun}$ bin. The corresponding number of events without neutrino oscillations is calculated by replacing $P(\nu_e \to \nu_e)$ in Eq.(3.16) by 1 and is expressed as $N_{SSM,\delta}(E_i,P_j)$. The fractional flux and its error are calculated by taking into account the number of background in each data samples as follows;

$$\begin{aligned} F_\delta(E_i,P_j) &\equiv f_\delta(E_i,P_j) \pm \sigma_\delta(E_i,P_j) \\ &\equiv \frac{N_{MSW,\delta}(E_i,P_j)}{N_{SSM,\delta}(E_i,P_j)} \pm \frac{\sqrt{N_{MSW,\delta}(E_i,P_j) + \alpha \times N_{obs}(E_i,P_j)}}{N_{SSM,\delta}(E_i,P_j)}, \end{aligned} \tag{3.20}$$

where $N_{obs,\delta}(E_i,P_j)$ is the number of background events in the i-th energy bin (E_i) and during the data taking period (P_j). α represents the fraction of the background events which exist in the signal region of solar neutrinos, and is estimated to ~ 0.1 (see Fig.4.2). Then the total flux in the direction of $\cos\delta_{sun}$ is calculated as follows;

$$F_{MSW}(\cos\delta_{sun}) = \frac{\sum_{i,j} f_\delta(E_i,P_j) \times 1/\sigma_\delta(E_i,P_j)}{\sum_{i,j} 1/\sigma_\delta(E_i,P_j)}. \tag{3.21}$$

The $\cos\delta_{sun}$ is chosen as 0.1, 0.3, 0.5, 0.7 and 0.9 in order to avoid bins with very small statistics in the real data analysis. Figure 3.8 shows the expected neutrino flux distribution as a function of $\cos\delta_{sun}$ in case of neutrino regeneration with $(\sin^2 2\theta,\Delta m^2)=$ $(0.11,3.5\times 10^{-6})$ for the solid line and $(0.05,7.9\times 10^{-6})$ for the dashed line. The observed neutrino flux distribution (described in the next chapter) is also shown in Fig.3.8 with the data point.

All of the calculations mentioned above are performed on each oscillation parameter of $(\sin^2 2\theta,\Delta m^2)$, which is limited in the range $10^{-4} \leq \sin^2 2\theta \leq 1$ and $10^{-8} \leq \Delta m^2 \leq 10^{-3}$ eV^2. The calculated data are classified into 41 × 51 grid points.

3.4 Comparison with the Monte Carlo Simulation

As mentioned above, the detector response has been incorporated by the analytic calculation, not by the Monte Carlo method. The reason is that the analytic expression give almost the same result as given by the Monte Carlo method. With the analytic expression, we could significantly save the computer CPU time. Figure 3.9 shows an example of the calculation made by the analytic and the Monte Carlo method in case of $(\sin^2 2\theta, \Delta m^2) = (0.01, 10^{-4})$. The two results are consistent within the statistical error of the Monte Carlo simulation.

3.5 Simulation of Other Solar Neutrino Experiments

The obtained data-base of the electron neutrino survival probability $P(\nu_e \rightarrow \nu_e)$ as a function of the oscillation parameter $(\sin^2 2\theta,E/\Delta m^2)$ are also useful for the radiochemical experiments such as the Homestake experiment and the SAGE.

KAM-II observes only ^{8}B solar neutrinos (also including very small contribution of hep neutrinos). Therefore, the simulation was performed solely with the ^{8}B neutrino energy spectrum. However, the Homestake experiment and the SAGE observe other neutrinos such as ^{7}Be, pep, pp neutrinos, which are shown in Table.1.4.

In case of the ^{37}Cl Homestake experiment, the largest contribution comes still from ^{8}B neutrinos. ^{7}Be neutrinos contribute next. (Two sources occupy approximately 91% of the total capture rate.) Thus, the created data-base for KAM-II are useful for the Homestake experiment. The energy threshold of the ^{37}Cl detector is 0.814 MeV.

Therefore, the data-base must be enlarged by adding the region of $E/\Delta m^2 \geq 10^3$ (MeV/eV^2). Fortunately, the neutrino survival probability P($\nu_e \rightarrow \nu_e$) is almost unity in the specified region of $\sin^2 2\theta \leq 10^{-1}$ and $E/\Delta m^2 \leq 10^4$ (MeV/eV^2). Hence, only for a small region of $\sin^2 2\theta \geq 10^{-1}$ and $10^3 \leq E/\Delta m^2 \leq 10^4$ (MeV/eV^2) must further be made.

The ^{71}Ga experiment has different characteristics in comparison with the above two experiments. The dominant contribution comes from pp neutrinos. As described in section 1.2, pp neutrinos have low energies ($E_\nu \leq 0.420$ MeV). Therefore, the obtained data-base are not useful. The energy threshold of ^{71}Ga detector is 0.23 MeV and the probability must be calculated in the range of $E/\Delta m^2 \geq 10^{2.4}$ (MeV/eV^2). However, it is not necessary to calculate the probability in the region of $\sin^2 2\theta \leq 10^{-1}$ and $E/\Delta m^2 \leq 10^4$ (MeV/eV^2) and in the region of $\sin^2 2\theta \geq 10^{-1}$ and $E/\Delta m^2 \leq 10^{3.5}$ (MeV/eV^2) because the probability P($\nu_e \rightarrow \nu_e$) equals unity.

Since these extra calculations of the capture rate for the two experiments correspond to the adiabatic solution, the spatial distribution of neutrino production rate for each neutrino source is taken into account. The spatial distribution of the production rate is divided into 50 and 75 different points, which are at $| R/R_\odot | = 0.02 \sim 0.20$ for ^{7}Be neutrinos and $0.02 \sim 0.30$ for pp neutrinos, for each $\cos\Theta$ case. (It is summarized in Table.3.1.) The regeneration effects in these detectors are also simulated by considering the detector location, because the neutrino path in the Earth of course depends on the latitude. Note that the radio-chemical experiments such as Homestake and SAGE are insensitive to the time of neutrino interactions event by event. Therefore, the expected capture rates are averaged over one year period. Figure 3.10(a), 3.10(b) and 3.10(c) show the contour lines on the oscillation parameter plane in case of KAM-II, the Homestake experiment and the SAGE, respectively.

Chapter 4

Analysis Procedure

4.1 Event Selection

The KAM-II detector began operating at the beginning of 1986. However, the radioactive background was too high and too variable to permit observation of solar neutrinos until December 1986. Measurement of ^{8}B solar neutrinos was carried out on 1040 detector live days of data with low radioactivity background, taken from January 1987 through April 1990. Two independent analyses were performed because of changing of the PMT's gain, in June 1988. Therefore, two data samples were obtained through the event selection as described below.

The event selection was performed by the following steps;

1. data reduction,
2. vertex reconstruction and fiducial volume cut,
3. elimination of muon induced background, and
4. remaining gamma ray cut.

The data reduction step rejects cosmic rays and selects events contained in the inner detector. The vertex positions of the reduced data are reconstructed and most external gamma-rays are rejected by the fiducial volume cut. Most of remaining high energy ($\gtrsim$ 8 MeV) events are electrons from beta-decay of spallation products. These events are rejected using spatial and time information. A fraction of external gamma-rays remain even after the fiducial cut. The fourth step therefore imposes a tighter criterion to reduce the remaining gamma-rays.

Figure 4.1 shows the trigger rates as a function of total electron energy for each step: (a) before the gain doubling, and (b) after the gain doubling. The solid curve shows the expected rate for the ^{8}B neutrinos calculated with SSM by Bahcall and Ulrich. The details of each step are described in Ref.[42].

4.2 Solar Neutrino Flux Measurement

The obtained final event samples after several reduction steps described in the previous section still contain non-removable background. To extract the ^{8}B solar neutrino signal, the final event sample is tested for a directional correlation with respect to the Sun. The test provides an additional order of magnitude discrimination against the isotropic background, which is described as follows.

As described in subsection 1.4.2, any correlation of direction of observed low-energy events with the direction from the Sun is made possible by the preservation of incident ν_e direction in the reaction $\nu_e + e^- \rightarrow \nu_e + e^-$, the moderate angle of multiple scattering of recoil electrons, and the observation in real time of each low-energy event.

Figure 4.2 shows the distribution in $\cos\theta_{sun}$ for $E_e \geq 9.3$ MeV for the entire 1040 days data sample, where $\cos\theta_{sun} = 1$ corresponds to the direction from the Sun to the Earth. The distribution for the data samples before and after the gain doubling are separately shown in Fig.4.3(a) and 4.3(b), respectively. The solid histograms in the figures give the shape of the signal expected from a Monte Carlo simulation based on the angular and energy resolution of the detector. All angular distributions show enhancement in the direction from the Sun above the isotropic background. However, the amount of th enhancement is less than that expected from calculation based on SSM [1][41].

The intensity of the signal relative to the SSM is obtained by the chi-squared method and by the maximum likelihood method with results differing by only a few percent. The likelihood function is defined by;

$$\begin{aligned} L(x) &= \prod_i \{\frac{1}{2}(1-\alpha(E_{e,i})x) + f_{solar}(\cos\theta_{sun,i})\alpha(E_{e,i})x\} \qquad (4.1) \\ \alpha(E_{e,i}) &\equiv \frac{N_{SSM}(E_{e,i})}{N_{DATA}(E_{e,i})}, \end{aligned}$$

where $N_{DATA}(E_e)$ and $N_{SSM}(E_e)$ are energy distributions of the final sample and the expected signal from SSM, and $f_{solar}(\cos\theta_{sun})$ is a normalized function which represents an expected angular distribution of the signal. The parameter x gives the intensity of the signal relative to the SSM prediction. The first term in $L(x)$ represents the isotropic background.

The energy spectrum of the final state electrons induced by solar ν_e is obtained by performing a maximum likelihood fit using in each energy bin, and also by a direct subtraction method in which the energy distribution of the isotropic background ($\cos\theta_{sun} \leq 0.8$) is subtracted from the energy distribution of events with $\cos\theta_{sun} > 0.9$. The resultant spectrum is essentially identical for both methods, and is shown in Fig.4.4 relative to the simulated spectrum based on $\sigma(\nu_e e^- \rightarrow \nu_e e^-)$, the known shape of the ν_e spectrum from ^{8}B decay, and the energy resolution of the detector. The best fit spectrum (dashed histogram) yields 0.46 × SSM [1] with reduced chi-squared of 1.05.

We note that the shape of the background (events with $\cos\theta_{sun} < 0.8$) electron energy distribution is compared with the shape of the background subtracted signal distribution in Fig.4.4(a) by means of a χ^2 test. The test yields a confidence level $< 1\%$ on the probability that the signal and background spectral shapes are the same.

Measurement of solar neutrino signal is carried out based on 1040 days data sample, consisting of subsamples of 450 days (January 1987 through May 1988) at $E_e \geq 9.3$ MeV and 590 days (June 1988 through April 1990) at $E_e \geq 7.5$ MeV. The flux value for the combined 450-day and 590-day data sample is

$$\frac{\text{Data}}{\text{SSM}} = 0.46 \pm 0.05(stat.) \pm 0.06(sys.) \qquad (4.2)$$

There is no significant difference between the relative flux values of 450- and 590- day's data samples, which are 0.48 ± 0.09 (stat.) ± 0.08 (sys.) ($E_e \geq 9.3$ MeV) and 0.45 ± 0.06 (stat.) ± 0.06 (sys.) ($E_e \geq 7.5$ MeV), respectively.

The possible sources of systematic error in the flux determination are uncertainties in absolute energy calibration , in angular resolution, and in calculated dead time of various cuts. The uncertainty in absolute energy calibration is estimated to be 3%, which corresponds to 12% of the obtained flux. The uncertainty in measurement of the angular resolution is less than 20%, which corresponds to 7% of the obtained flux. The dead time and uncertainty introduced by the various event selection criteria are estimated using a Monte Carlo simulation based on real data of known physical processes, such as spallation products. The estimated uncertainty is 4% of the measured flux. The quadratic sum of above uncertainties is 14% of the obtained flux, which corresponds to 0.06 × SSM.

4.3 Analysis of Neutrino Matter Oscillations in the Sun

In order to obtain quantitative information on neutrino matter oscillations in the Sun, three different fits are carried out using the measured energy spectrum of recoil electrons as described in the previous section and the calculated energy spectrum of recoil electrons obtained by the simulation as explained in section 3.3. The three fits are as follows.

1. Only the total flux was used in the fit. A systematic error, which is 0.06 times the flux predicted by the SSM [1] is taken into account in the χ^2 definition;

   $$\chi^2 \equiv \frac{(x - \alpha x_0)^2}{\sigma^2} + (\frac{\alpha - 1}{\sigma_\alpha})^2, \tag{4.3}$$

   where x, x_0 and σ are the measured total flux, the calculated total flux for one set of oscillation parameters ($\sin^2 2\theta$,Δm^2) and the statistical error, respectively. α is the normalization factor which is varied to reach the minimum χ^2 with the constraint of the systematic error of σ_α.

2. Both the energy spectrum and the total flux are used in the fit. The χ^2 is defined as;

   $$\chi^2 \equiv \sum_i \frac{(x_i - \alpha x_{0i})^2}{\sigma_i^2} + (\frac{\alpha - 1}{\sigma_\alpha})^2, \tag{4.4}$$

where x_i is the measured flux in the i-th energy bin, x_{0i} is the expected flux in the i-th energy bin for one set of oscillation parameters ($\sin^2 2\theta$,Δm^2), and σ_i is the statistical error in the i-th energy bin.

3. A χ^2 fit without the constraint of the normalization (of the total flux) is performed to see the effectiveness of the electron spectral shape more clearly. Namely, the second term in Eq.(4.4) is removed and α in the first term is treated as a free parameter.

These fits are performed on each neutrino oscillation parameter of ($\sin^2 2\theta$,Δm^2). The area specified by $10^{-4} \le \sin^2 2\theta \le 1$ and $10^{-8} \le E/\Delta m^2 \le 10^{-3}$ (MeV/eV^2) is divided into 41 × 51 grid points.

The χ^2 value obtained by the fits obey the normal χ^2 distribution with two free parameters. Therefore, the regions on the oscillation parameter plane with $\chi^2 \le \chi^2_{min}$ + 2.41, 4.61 and 5.99 are allowed at 68%, 90% and 95% confidence level (C.L.), respectively. The resultant allowed regions at 68%, 90% and 95% C.L. in case of 1, 2 and 3 are shown in Fig.4.5, Fig.4.6 and Fig.4.7.

Some special care should be taken to check possible biases which might affect the results of th electron spectrum shape fit. For example, the overall energy scale is shifted by ± 3%, which corresponds to the uncertainty of the energy scale, and the energy scale is accordingly shifted by ± 3% in one of two subsamples (data before and after the gain doubling) which are then combined. Other similar tests are performed, but there is no noticeable difference in the confidence contours. Therefore, the obtained allowed region in Fig.4.5, 4.6 and 4.7 are robust.

4.4 Analysis of Neutrino Regeneration Effect in the Earth (Day/Night Effect)

Any day/night difference induced by regeneration in the Earth depends on the path lengths and density profiles experienced by the neutrinos passing through the Earth as described in subsection 1.5.3. The KAM-II 1040 days' data sample are divided into daytime and nighttime subsample, where daytime (nighttime) sample is defined as the time region where the Sun is above (below) the horizon. Their data taking times by KAM-II detector are 500 and 540 live days, respectively. The observed neutrino flux of each data sample is obtained by using the maximum likelihood method as described in section 4.2, and is 0.91 ± 0.15 (stat.) for daytime and 1.07 ± 0.16 (stat.) for nighttime, respectively, relative to the averaged value (0.46 relative to the SSM prediction) as shown in Fig.4.9(a). The relative difference between the daytime and nighttime fluxes is expressed by;

$$\frac{\text{Day} - \text{Night}}{\text{Day} + \text{Night}} = -0.08 \pm 0.11(stat.) \pm 0.03(sys.), \tag{4.5}$$

where the systematic error will be discussed below. Within statistical errors, there is no significant difference between the daytime and nighttime fluxes.

A day/night difference would at some level be correlated with a semiannual variation of the solar neutrino flux, because the day and night durations vary with the time of year. A semiannual variation is possible because the solar equatorial plane and the ecliptic plane cross with an opening angle of $7°15'$ twice per year. Therefore, the strength of the interaction of a neutrino magnetic moment with the solar magnetic field would be less at the time when a line from the Earth to the center of the Sun crosses the equatorial plane and consequently a maximum modulation of the solar neutrino flux might occur. Figure 4.9(c) shows the semiannual difference of the observed neutrino flux. There is no evidence for a magnetic interaction of ν_e in the Sun within our experimental sensitivity. Moreover, we search for a semiannual variation using the day and night samples separately to distinguish any day/night effect from any semiannual variation. The resultant fluxes are shown in Fin.4.9(d) and (e), which confirm the negative result in Fig.4.9(c), and justify using the total data sample to extract the implication of null day/night result for the MSW effect.

More information on neutrino oscillations can be extracted from the solar neutrino data by dividing the total sample into subsamples with different paths through the Earth. The path length (and density profiles) has a one-to-one correspondence with the angle of the Sun relative to the detector coordinate. Hence, the data sample is divided into 6 subsamples based on $\cos\delta_{sun}$, which are $\cos\delta_{sun}$ = -1 - 0 (daytime sample), 0 - 0.2, 0.2 - 0.4, 0.4 - 0.6, 0.6 - 0.8 and 0.8 - 1.0. The data-taking time for each subsample is 92, 103, 138, 113, and 99 equivalent days, respectively. The angular distribution for each data sample is shown in Fig.4.8. The fluxes obtained from the data subsamples are shown in Fig.3.8. The reduced χ^2 calculated under the assumption of constant flux with respect to $\cos\delta_{sun}$ is 0.43 for 5 degrees of freedom, which corresponds to an 83% C.L. The result also indicates that there is no significant day/night difference of neutrino flux.

In the neutrino oscillation analysis, only the relative flux values are employed, and it is necessary to estimate carefully possible systematic errors in the relative values. A possible time variation of the gain of the detector has a negligible effect, because it affects equally all $\cos\delta_{sun}$ data subsamples. The dead time difference between such subsamples is also negligible. The most serious source of the systematic error is a possible small anisotropy in the $\cos\delta_{sun}$ distribution of the background in each of the relatively low statistics subsamples with respect to the direction of the Sun.

The background events which remain after all cuts are estimated to be composed of two sources. One is relatively lower energy events ($E_e \lesssim 8 \sim 9$MeV), which must be radioactivity in water, and another one is relatively higher energy events ($E_e \gtrsim 8 \sim 9$MeV), which must be external gamma-rays and spallation products which are not rejected by the present cuts. Therefore, for a quantitative estimate of the systematic error induced by the asymmetric distribution of the background events, we generate the background distributions using a Monte Carlo simulation for each $\cos\delta_{sun}$ data subsample, and then we obtain the neutrino flux of each $\cos\delta_{sun}$ data subsample using these simulated background angular distributions. The fluxes obtained from this calculation is shown in Table.4.1. Any systematic error from this cause is estimated to be less than 8% of the observed signal in that $\cos\delta_{sun}$ interval, which is much less than the statistical error in that interval.

Comparison of data and theory is performed with a standard χ^2 function defined by;

$$\chi^2 \equiv \sum_{\cos\delta_{sun}} \frac{(F_{obs}(\cos\delta_{sun}) - x \times F_{osc}(\cos\delta_{sun}))^2}{\sigma_F^2}, \tag{4.6}$$

where $F_{obs}(\cos\delta_{sun})$ and $F_{osc}(\cos\delta_{sun})$ are the observed and calculated fluxes, the latter for each oscillation parameter of ($\sin^2 2\theta$,Δm^2), and σ_F is the experimental error (quadratic sum of statistical and systematic errors) in the observed fluxes. The quantity x is the scale factor which is varied to reach a minimum χ^2. Note that this procedure exploits the null time dependence of the observed flux, and does not rely directly on the absolute value of the predicted flux.

The minimum χ^2 (χ^2_{min}) occurs at $(\sin^2 2\theta, \Delta m^2) = (0.13, 1.3\times10^{-5})$ with the value 1.20 for 3 degrees of freedom. The region $\chi^2 > \chi^2_{min} + 2.41$, 4.61 and 5.99 are excluded with 68%, 90% and 95% confidence by the analysis of the day/night effect alone, and the resultant excluded regions are shown in Fig.4.10.

Chapter 5

Result and Discussion

5.1 MSW Solutions from Kamiokande-II

The results from 1040 days' data of KAM-II show a possibility to solve the solar neutrino problem using neutrino matter oscillations (MSW effect in the Sun and the Earth), which give a strong constraint on the oscillation parameters ($\sin^2 2\theta$,Δm^2). But, are the neutrino matter oscillations really a unique solution to explain the solar neutrino deficit ? Unfortunately, the answer is no, based only on the present results. As described in Chapter 1, there is a variety of possibilities, namely the neutrino (just so) vacuum oscillation around $\sin^2 2\theta \geq 0.7$ and $4 \times 10^{-11} \leq \Delta m^2 \leq 10^{-10}$ eV^2 [10][11], the neutrino decay with mixture of mass eigenstates [11], and the spin flavor transition mechanism which includes also the MSW mechanism [18][19][20]. There are, however, also many difficulties in these solutions: (i) the allowed region by just so neutrino oscillations is fine-tuned in such a way that the oscillation length just happens to be nearly equal to one astronomical unit, (ii) the neutrino decay requires a new almost massless scalar particle with a strong coupling constant to neutrinos, and (iii) the spin flavor conversion requires an unnaturally large magnetic moment and also extremely large magnetic field in the convective layer of the Sun. Therefore, we believe that the MSW solution is the most viable solution.

As described in the previous chapter, the solar neutrino data from KAM-II have been analyzed for compatibility with the different types of the MSW formalism such as adiabatic and non-adiabatic solutions. The measured recoil electron energy spectrum restricts the allowed region on the plane of the oscillation parameters ($\sin^2 2\theta$,Δm^2) to a triangular region and disfavors the adiabatic solution of $7.2\times10^{-4} \leq \sin^2 2\theta \leq 6.3\times10^{-3}$ and $\Delta m^2 \sim 1.3 \times 10^{-4}$ eV^2 at 90% C.L. without employing the absolute flux value predicted by the SSM calculated by Bahcall and Ulrich.

The neutrino regeneration effect in the Earth enlarges the allowed region determined from solar neutrino flux integrated over 1040 days (the MSW effect in the Sun) to $7 \times 10^{-2} \leq \sin^2 2\theta \leq 6 \times 10^{-1}$ and $10^{-6} \leq \Delta m^2 \leq 10^{-5}$ eV^2. However, the $\cos\delta_{sun}$ distribution of the neutrino flux shows no dependence on $\cos\delta_{sun}$ as seen in Fig.4.9. Hence, the region of $\sin^2 2\theta \geq 0.02$ and $2 \times 10^{-6} \leq \Delta m^2 \leq 10^{-5}$ eV^2 is newly excluded (shaded region in Fig.5.1) at 90% C.L. Note that this new excluded region does not rely on the absolute flux value.

There still remains most of the non-adiabatic solution, the large-mixing-angle solution except the region which was excluded by the Day/Night effect and a part of adiabatic solution around $\Delta m^2 \sim 10^{-4}$ eV^2 as shown in Fig.5.1. To restrict the region, further analysis should be made by combining the KAM-II result with the ones from the ^{37}Cl Homestake experiment and the SAGE experiment.

Direct comparison between the solar neutrino fluxes obtained by various detectors is problematical, because different detectors have different neutrino energy thresholds. Also, there is an essential difference between the KAM-II and the others. The KAM-II measures the energy spectrum of recoil electrons, direction of neutrinos and their arrival time, while the others are radio-chemical experiments which have no ability like those. As described in Chapter 1, the Homestake experiment carefully estimates the amount of background events and subtracts them from the observed signal. At least, there is apparently no serious problem in their analysis procedure. Therefore, we will discuss the MSW solution obtained from the combined KAM-II and the Homestake data in the next section.

5.2 Comparison with the Homestake Experiment

The Homestake experiment is mostly sensitive to the 0.86 MeV monoenergetic ν_e from the electron capture reaction of ^{7}Be nuclei and to neutrinos with the continuous energy spectrum from 0 to 15 MeV from the decay of ^{8}B nuclei in the Sun. The averaged neutrino flux from 1970 to 1990 was 2.3 ± 0.3 SNU [8], which corresponds to 0.51 ± 0.05 ^{37}Ar atoms production per day. Also, the weighted average flux during the period of January 1987 through April 1990, which corresponds to the data-taking time of KAM-II, is 2.12 ± 0.34 SNU [42]. The predicted capture rate from the SSM calculated by Bahcall and Ulrich is 7.9 ± 2.6 SNU, among which 6.1 SNU is attributed to ^{8}B neutrinos, 1.1 SNU to ^{7}Be neutrinos, and the rest to other minor branches. Each flux is sensitive to the central temperature of the Sun (see Eq.(1.2) $\sim$ Eq.(1.4)). If the central temperature is so modified as to reproduce the flux obtained by KAM-II (in fact, the decrease of the central temperature is a mere 4%), the ^{7}Be neutrino flux is expected to decrease down to 0.71 relative to the SSM prediction. Therefore, the expected capture rate of the Homestake experiment should be;

$$\text{Capture rate} = 6.1\ (\text{SNU}) \times 0.46\ [^8\text{B}] + 1.1\ (\text{SNU}) \times 0.71\ [^7\text{Be}] = 3.6\ (\text{SNU}). \quad (5.1)$$

Taking into account the contribution of the other neutrino sources, the total capture rate must be 4.2 SNU, which is about 6σ away from the experimental result.

We are thus led to consider the neutrino matter oscillations in the Sun and the Earth again here. The allowed region from the Homestake experiment at 90% C.L. is obtained by a similar analysis employed by KAM-II as shown in Fig.5.2, where the solid line shows the allowed region of KAM-II and the dashed line of Homestake. Note that most of the adiabatic region of $\Delta m^2 \geq 10^{-4}$ eV^2 is completely excluded by non-overlapping of the two allowed regions. The neutrino regeneration effect in the Earth is also seen around the region of $10^{-1} \leq \sin^2 2\theta \leq 7\times10^{-1}$ and $1.5\times10^{-6} \leq \Delta m^2 \leq 5\times10^{-6}$ eV^2 in Fig.5.2. However, a large part of that region is excluded by null observation of the Day/Night effect by KAM-II. The resultant remaining region satisfying both of the experiments is mainly the non-adiabatic solution of $\sin^2 2\theta \times \Delta m^2 = 10^{-7.5\pm0.2}$ and $\Delta m^2 = 10^{-6\pm1.2}$ eV^2, and the large-mixing-angle region of $5 \times 10^{-1} \leq \sin^2 2\theta \leq 9 \times 10^{-1}$, $2 \times 10^{-7} \leq \Delta m^2 \leq 1.5 \times 10^{-6}$ and $5 \times 10^{-6} \leq \Delta m^2 \leq 10^{-4}$ eV^2.

5.3 Effect of Uncertainties in the Standard Solar Model

As described in section 1.2, the standard solar model itself has several uncertainties. The theoretical three-standard-deviation (3σ) error of the neutrino fluxes calculated by Bahcall and Ulrich are ±37% and ±15% for ^{8}B and ^{7}Be neutrinos, respectively. Therefore, the conclusion derived from the MSW solutions assuming the central value of the SSM prediction has to be tested for these uncertainties in the SSM calculation.

The predicted fluxes were (a) increased or (b) decreased by its theoretical 3σ error from the central value and then the similar analysis described in the previous section is performed. The total theoretical 3σ error is given by adding the errors of ^{8}B (37%) and ^{7}Be (15%) neutrino flux. The predicted ^{37}Cl capture rate for increased and decreased neutrino flux becomes (a) 10.3 and (b) 5.5 SNU, respectively. The KAM-II result becomes (a) 0.33 ± 0.04 (stat.) $\pm$ 0.04 (sys.) and (b) 0.73 ± 0.08 (stat.) $\pm$ 0.10 (sys.) relative to the SSM prediction, respectively. The resultant allowed region at 90% C.L. in each case is shown in Fig.5.3(a) and 5.3(b). Note that, in Fig.5.3(b), the allowed region of KAM-II exists outside the triangular region, because the observed flux is within the predicted flux at 90% C.L. From these figures, most part of the adiabatic solutions ($\Delta m^2 \geq 1.5 \times 10^{-4}$ eV^2) is still ruled out by non-overlapping of the two allowed regions, while the non-adiabatic solution is still a viable solution even if the ^{8}B and ^{7}Be neutrino fluxes are changed with the maximum permissible amount estimated by Bahcall and Ulrich. The overlapping region of the non-adiabatic solution allows the oscillation parameter of $\sin^2 2\theta \times \Delta m^2 = 10^{-7.6\pm0.5}$ and $6 \times 10^{-7} \leq \Delta m^2 \leq 10^{-5}$ eV^2 which includes the maximum theoretical error in the neutrino fluxes as shown in Fig.5.4. The large-mixing-angle solution survives in the case of flux increase, while it is restricted to $\sin^2 2\theta \geq 0.9$ in the case of flux decrease.

Another standard solar model recently calculated by Turck-Chièze et al. predicts different production rates of neutrinos. (see Table.5.1) If the neutrino flux by Turck-Chièze are employed instead of that by Bahcall and Ulrich, the measured flux by KAM-II is 0.70 ± 0.08 (stat.) $\pm$ 0.09 (sys.) relative to the predicted value. On the other hand, the predicted fluxes of ^{8}B and ^{7}Be neutrinos are 3.8×10^6 and 4.18×10^9 cm^{-2}sec^{-1}, respectively, and the predicted capture rate of the ^{37}Cl Homestake experiment is 5.8 ± 1.3 SNU. Using these fluxes, the comparison of the allowed region between KAM-II and Homestake was made. Figure 5.5 shows the allowed regions at 90% C.L. The allowed region from KAM-II is again outside the triangular region just as in Fig.5.3(b), hence, the non-adiabatic region is still allowed and narrow region of $\sin^2 2\theta \geq 0.9$ is also allowed.

In summary, even if the uncertainties in the calculation of the solar neutrino fluxes and/or the model dependence is taken into account, there are still allowed regions on the oscillation parameter ($\sin^2 2\theta$,Δm^2) plane.

5.4 Significance of the Gallium Experiment

There exist two ^{71}Ga experiments which are called SAGE and GALLEX. Recently, SAGE reported a new result [9]. Assuming that the extraction efficiency of ^{71}Ge atoms produced by solar neutrinos is the same as from the natural Ge carriers, they observed the capture rate of $20\,^{+15}_{-20}$ (stat.) ± 32 (sys.) SNU, corresponding to a 90% C.L. upper limit of 79 SNU. A calibration of the overall detection efficiency of the experiment is scheduled in 1992 with a 1 MCi ^{51}Cr neutrino source. Thus, the SAGE result also shows a large solar neutrino deficit compared to the predicted capture rate of $132\,^{+20}_{-17}$ SNU by the SSM calculated by Bahcall and Ulrich [1]. The minimum expected rate in a ^{71}Ga experiment, assuming only that the Sun is presently generating nuclear energy at the rate at which it is radiating energy, is 79 SNU [2]. This extreme case is achieved if only pp and pep neutrinos are produced by the Sun. The SAGE result, therefore, strongly suggests that the solar neutrino deficit should be caused by intrinsic properties of neutrinos but not by the uncertainties in the SSM.

From the simulation of the ^{71}Ga experiment as described in Chapter 3, the expected capture rate of solar neutrinos was obtained on the oscillation parameter plane. Figure 5.6 shows iso-SNU contours on the ($\sin^2 2\theta$,Δm^2) plane without the neutrino regeneration effect in the Earth. The contours from inside show 10, 20, 40, 60, 80, 100 and 120 SNU, respectively. Note that the adiabatic solution is mainly located at $\Delta m^2 \sim 10^{-5}$ eV^2, because pp neutrinos have energies lower than 0.42 MeV. The calculation has taken into account the production position dependence of neutrinos. Figure 5.7 shows both the ^{71}Ga iso-SNU contours and the allowed regions of KAM-II and the Homestake experiment. The overlapped allowed region in the non-adiabatic solution is located on the contours less than 100 SNU. Thus far the SAGE result is not sensitive enough to draw further conclusions.

The ^{71}Ga iso-SNU contour lines were also calculated with decreased and increased fluxes by the theoretical 3σ error of the ^{7}Be and ^{8}B neutrino fluxes. Figure 5.8(a) and 5.8(b) show the iso-SNU contours of the ^{71}Ga experiment and the allowed regions of KAM-II and the Homestake experiment for a ^{8}B neutrino flux increased by 37% and for a ^{7}Be neutrino flux increased by 15%, and decreased ones, respectively. The dotted contours from inside show 10, 20, 40, 60 and 80 SNU, respectively. The region corresponding to the capture rate of the ^{71}Ga experiment less than 79 SNU in each case disfavors the overlapping region of the non-adiabatic solution with $\Delta m^2 \geq 10^{-5}$ eV^2 and of the residual adiabatic solution with a large mixing angle ($\sin^2 2\theta \geq 0.1$). However, the present SAGE result does not provide additional constraints on the remaining allowed parameters.

So far, the Day/Night effect has not been taken into account in the discussion above. The regeneration effect in the Earth is expected in the region of $\sin^2 2\theta \geq 0.2$ and $10^{-8} \leq \Delta m^2 \leq 10^{-6}$ eV^2. The expected capture rate of the overlapping regions around these parameters, hence, should be affected by the regeneration effect. The predicted contours of the capture rate are shown in Fig.5.9. The contours from inside shows 10, 20, 30, 40, 60, 80, 100 and 120 SNU, respectively. As compared to Fig.5.6, there is an increase by about 10 SNU for the capture rate around the region of $0.1 \leq \sin^2 2\theta \leq 0.4$ and $5\times10^{-8} \leq \Delta m^2 \leq 6\times10^{-7}$ eV^2. The allowed regions of KAM-II and the Homestake experiment together with the SAGE iso-SNU contour lines are shown in Fig.5.11, and the same as Fig.5.8, but taking into account the regeneration effect, is also shown in Fig.5.10. Again, the present SAGE result does not provide any new information on the oscillation parameters.

5.5 Future Prospect

As is described in the previous section, the first result from the SAGE experiment gives a strong suggestion that the solar neutrino deficit should be caused by some intrinsic properties of neutrinos. To check the overall detection efficiency, the SAGE experiment is now planning a calibration in 1992 with a 1-M Ci ^{51}Cr neutrino source. On the contrary, the SAGE experiment has not added to the combined KAM-II and Homestake result any new information on the neutrino-oscillation parameters due to its large statistical and systematic errors. The GALLEX (^{71}Ga) experiment is currently taking data with lower background level and will soon present its first result, to which we are looking forward.

Then, what should we do next, in order to further restrict the allowed region on the oscillation parameter plane and to convince that the neutrino deficit is really caused by the MSW neutrino oscillations ? We should measure the neutral-current/charged current event ratio as well as the energy spectrum of solar neutrinos as precisely as possible with high-statistics and low-energy-threshold experiments. The present KAM-II can not afford to measure the energy spectrum precisely due to its poor statistics and its relatively high-energy analysis threshold (7.5 MeV). And the present KAM-II obviously can not measure the charged-current/neutral-current event ratio, as it can not distinguish neutral-current events from charged-current ones. In this chapter, two funded next-generation neutrino experiments challenging to disentangle the solar neutrino deficit, i.e., Super-Kamiokande and SNO which are now under construction will be described.

5.5.1 Super-Kamiokande

The Super-Kamiokande project [43] is based on all the achievements and experiences that have been obtained with the present Kamiokande experiment. The size of the detector will be 50,000 tons of total volume in which 32,000 tons is for inner volume, surrounded by the photomultipliers with the density 2 PMTs/m^2 (40% photosensitive area). The lowest detectable total energy is expected to be 5 MeV which is limited by backgrounds. Super-Kamiokande will start data-taking in 1996 and observe about

7,500 solar neutrino events per year, if the neutrino flux is 46% of the SSM prediction calculated by Bahcall and Ulrich. Main characteristics of Super-Kamiokande are shown in Table.5.2.

The high-statistics data will strongly constrain the solution of the solar neutrino problem, in particular, the MSW solution, by investigating the recoil electron energy spectrum in detail. Figure 5.12 shows the expected electron energy spectral from the MSW mechanism normalized by the SSM calculated by Bahcall and Ulrich in case of $(\sin^2 2\theta, \Delta m^2) = (0.01, 3 \times 10^{-6})$, $(0.1, 4 \times 10^{-7})$, $(0.5, 1 \times 10^{-7})$ and $(0.7, 5 \times 10^{-7})$. The statistical errors correspond to 5 year operation.

As seen in this figure, even among non-adiabatic solutions, there is a slight difference in shape which the precise measurement will be able to resolve independently of the absolute flux value.

5.5.2 Sudbury Neutrino Observatory

The Sudbury Neutrino Observatory (SNO) detector [44] will be installed in a deep mine (2070 m underground corresponding to 5900 meter water equivalent) near Sudbury 200 miles north of Tront in Canada. The detector consists of 1,000 tons of heavy water (D_2O) surrounded by 7,000 tons of purified light water (H_2O). The Čerenkov light emitted by recoil electrons is detected by photomultipliers which cover 40% of the detector surface.

The unique feature of this experiment is to detect the neutral-current reaction of the neutrino-deuteron scatterings. The expected reactions are as follows;

$$\nu_e + d \rightarrow e^- + p + p - 1.44\text{MeV} \tag{5.2}$$

$$\nu_x + d \rightarrow \nu_x + p + n - 2.33\text{MeV} \tag{5.3}$$

$$\nu_e + e^- \rightarrow \nu_e + e^-. \tag{5.4}$$

Eq.(5.2) (neutrino absorption by deuteron) and Eq.(5.4) show the charged-current reactions and Eq.(5.3) shows the pure neutral-current reaction. The signal from the reaction in Eq.(5.2) dominates over Eq.(5.4). The quasi-free neutron in reaction Eq.(5.3) is captured by a ^{35}Cl atom when NaCl is added in the D_2O reservoir and gives about 8 MeV gamma-ray by the (n,γ) reaction. In addition, the SNO experiment can measure the real neutrino (not recoil-electron) energy spectrum via the neutral-current reaction Eq.(5.3).

The expected rate for the reaction of Eq.(5.2) is about 2,500 events per year ($E_e > 5$ MeV) and of Eq.(5.3) about 1,000 events per year, if the ^{8}B neutrino flux is assumed to be 0.46 of the SSM prediction. If neutrino oscillations really occur, the ratio between neutral-current events and charged-current events (NC/CC) will increase and will observe the distortion of the neutrino energy spectrum by the MSW neutrino oscillations.

However, in the reaction of Eq.(5.3), the energy and direction of an incident neutrino can not be measured. Therefore, in fact, it will be difficult to measure the reactions of Eq.(5.3) unless the radio-active background in the detector materials is reduced sufficiently. The SNO experiment will start data-taking in late 1994.

Chapter 6

Conclusion

An analysis of the MSW effect using the KAM-II 1040 days' data has been presented in this paper. The measured total flux as well as the recoil electron energy spectrum of ^{8}B solar neutrinos provides a strong constraint on the oscillation parameters ($\sin^2 2\theta, \Delta m^2$). The allowed region on the oscillation-parameter plane is obtained by comparing the observed energy spectrum with the predicted one from the neutrino matter oscillations assuming the SSM calculated by Bahcall and Ulrich.

The adiabatic region of:

$$7.2 \times 10^{-4} \leq \sin^2 2\theta \leq 6.3 \times 10^{-3} \;\; \text{with} \;\; \Delta m^2\,(\mathrm{eV}^2) \cong 1.3 \times 10^{-4} \tag{6.1}$$

is excluded at 90% confidence level by the measured shape of the recoil-electron energy spectrum alone. Also, a region of:

$$\sin^2 2\theta \geq 0.02 \;\; \text{with} \;\; 2 \times 10^{-6} \leq \Delta m^2\,(\mathrm{eV}^2) \leq 10^{-5} \tag{6.2}$$

is excluded at 90% confidence level by null observation of the Day/Night effect without any assumption on the absolute value of the solar neutrino flux.

Assuming the central value of the ^{8}B neutrino flux predicted by the SSM of Bahcall and Ulrich, the region allowed by KAM-II alone is the non-adiabatic region of:

$$\sin^2 2\theta \times \Delta m^2 = 10^{-7.5\pm0.3} \;\; \text{with} \;\; 1.8 \times 10^{-8} \leq \Delta m^2\,(\mathrm{eV}^2) \leq 1.3 \times 10^{-4} \tag{6.3}$$

and the large-mixing-angle region of:

$$\sin^2 2\theta \geq 6 \times 10^{-1} \quad \text{with} \quad 5 \times 10^{-5} \leq \Delta m^2\,(\mathrm{eV}^2) \leq 1.0 \times 10^{-4} \tag{6.4}$$

and

$$\sin^2 2\theta \geq 6 \times 10^{-1} \quad \text{with} \quad 1 \times 10^{-8} \leq \Delta m^2\,(\mathrm{eV}^2) \leq 1.5 \times 10^{-6}. \tag{6.5}$$

Combining the present KAM-II result with the result from Homestake experiment, a further constraint is obtained on the allowed region of the oscillation parameters. In this case, the theoretical 3σ uncertainties of the solar neutrino flux calculated by the SSM of Bahcall and Ulrich are properly taken into account.
The almost adiabatic region of:

$$1.2 \times 10^{-4} \leq \sin^2 2\theta \leq 6 \times 10^{-1} \text{ with } 2 \times 10^{-5} \leq \Delta m^2\,(\mathrm{eV}^2) \leq 2 \times 10^{-4} \tag{6.6}$$

is then ruled out. Also allowed are the regions in the non-adiabatic region of:

$$\sin^2 2\theta \times \Delta m^2 = 10^{-7.6\pm0.5} \text{ with } 6 \times 10^{-7} \leq \Delta m^2\,(\mathrm{eV}^2) \leq 10^{-5}. \tag{6.7}$$

and in the large-mixing-angle region of:

$$\sin^2 2\theta \geq 4 \times 10^{-1} \quad \text{with} \quad 1.5 \times 10^{-6} \geq \Delta m^2\,(\mathrm{eV}^2) \tag{6.8}$$

and

$$\sin^2 2\theta \geq 4 \times 10^{-1} \quad \text{with} \quad 3.5 \times 10^{-5} \leq \Delta m^2\,(\mathrm{eV}^2) \leq 1 \times 10^{-4}. \tag{6.9}$$

The recent result from the SAGE experiment, 79 SNU (90% C.L. upper limit) compared to the SSM prediction of 132 $^{+20}_{-17}$ SNU calculated by Bahcall and Ulrich, gives small constraints on the oscillation parameter; (i) a narrow region of the non-adiabatic solution with $\Delta m^2 \geq 10^{-5}$ eV^2 and (ii) a residual region of the adiabatic solution with a large mixing angle ($\sin^2 2\theta \geq 0.1$) are disfavored by taking into account the theoretical uncertainties of the neutrino flux. However, the present SAGE result does not constrain the above regions due to the limited statistics and the large systematic errors. It is stressed that high-precision and high-statistics experiments (Super-Kamiokande and SNO) are clearly needed to further study the uniqueness of the MSW solution. And if the MSW solution is indeed correct, these next-generation solar neutrino experiments will squeeze the allowed region of underlying oscillation parameters ($\sin^2 2\theta$,Δm^2).

Appendix A

Standard Solar Model

The standard solar model describes the structure of the Sun by means of the following four equation.

Hydrostatic equilibrium between the gravitational force and the radiative and particle pressures;

$$\frac{dP(r)}{dr} = -\rho\frac{GM(r)}{r^2}, \tag{A.1}$$

where r is a distance from the center of the Sun, $P(r)$ is the pressure, ρ is the density, G is the constant of gravitation and $M(r)$ is the mass in a sphere within the radius r.

Energy transport by radiation or convective motion;

$$-\frac{dT}{dr} = \frac{3\kappa\rho L(r)}{4acT^3 4\pi r^2} \;(radiation), \tag{A.2}$$

$$-\frac{dT}{dr} = -(1-\frac{1}{\gamma})\frac{T}{P}\frac{dP}{dr} \;(convection), \tag{A.3}$$

where T is the temperature, κ is the Rosseland mean opacity, a is the Stefan-Boltzmann constant, c is the light velocity, and γ is the ratio of the specific heats C_p/C_v. These two equations are exclusive. One can calculate $\frac{dT}{dr}$ and $\frac{dP}{dr}$ from Eqs.(A.1) and (A.2) in every layer of the Sun, and if

$$-\frac{dT}{dr} < -(1-\frac{1}{\gamma})\frac{T}{P}\frac{dP}{dr} \tag{A.4}$$

then the layer is stable against convective motions and the temperature gradient is given by Eq.(A.2). If it is not the case, the convective motions occur and the temperature gradient is given by Eq.(A.3). In the deep interior, the energy transport is primarily by photon diffusion and is described in Eq.(A.2). For layers that are unstable against convective motions, the temperature gradient is taken to be the adiabatic gradient (Eq.(A.3)) except near the surface where mixing length theory is employed.

Energy generation by nuclear reactions and conservation ;

$$\frac{dL(r)}{dr} = 4\pi r^2 \rho\epsilon, \tag{A.5}$$

where ϵ is the energy released from nuclear reactions, $L(r)$ is the luminosity. Equation (A.5) shows that the luminosity is balanced by the energy generation of nuclear reactions. The standard solar model includes departures from nuclear equilibrium that are caused by the fusion processes themselves, for example, in the abundance of ^{3}He.

Mass continuity ,

$$\frac{dM(r)}{dr} = 4\pi r^2 \rho. \tag{A.6}$$

Together with these four differential equations, the calculation of the solar evolution employs. Three explicit relations which characterize the behavior of the interior gasses, i.e., the equation of state, the equation for opacity, and the equation for energy production by nuclear reactions. They are formalized by;

$$\begin{aligned} P &= P(\rho, T, X, Y, Z) && \text{(A.7)} \\ \kappa &= \kappa(\rho, T, X, Y, Z) && \text{(A.8)} \\ \epsilon &= \epsilon(\rho, T, X, Y, Z), && \text{(A.9)} \end{aligned}$$

where X, Y, and Z are the fractional abundance of hydrogen, helium and the heavier elements, respectively $(X + Y + Z = 1)$. If one use the relations of Eqs.(A.7) - (A.9) to eliminate ρ, κ and ϵ from the differential equations Eqs.(A.1) - (A.6), these equations contain five variables P, $M(r)$, $L(r)$, T and r. Thus, the problem of stellar structure is reduced to four simultaneous non-linear first order differential equations for four variables where all four variables are a function of the fifth variable. All variables of

$P(r)$, $M(r)$, $L(r)$, $T(r)$, $\rho(\mathrm{r})$, X, Y, and Z are a function of time, t. The boundary conditions are the solar mass $M_\odot$, luminosity $L_\odot$, and radius $R_\odot$ at the present age of 4.6×10^9 year.

The standard solar model adopts two assumption as regards the chemical composition of the Sun.

1. The Sun was chemically homogeneous at $t = 0$, and changes in the local abundance of each isotope occurred only by nuclear fusion processes.
2. The composition of the present solar surface reflects the initial abundances of elements heavier than helium.

Thus, the initial value of X can be calculated by using these assumptions and the boundary conditions. Subsequently, the evolution and structure of the Sun are solved. Some of the characteristic parameters of the Sun, which are measured or calculated, are shown in Table.1.1.

Appendix B

Nuclear Fusion Reaction

The reaction rate of nuclear fusion reaction is described by;

$$Rate_{ij} = \frac{n_i n_j}{(1+\delta_{ij})} < \sigma v >_{ij}, \tag{B.1}$$

where n_i, n_j are number density of type i and j, σ is their interaction cross section, v is the magnitude of their relative velocity, and δ is the Kroneker delta prevents double counting of identical particles.

The rates of nuclear fusion reactions in the solar interior are dominated by Coulomb barriers. The typical thermal energy of particles in the solar interior is a few keV, which is much smaller than the typical height of Coulomb barriers of a few MeV among light elements. Therefore, the nuclear fusion released in the Sun are caused by the quantum mechanical effect of tunneling through a potential barrier.

The fusion cross section is represented by a formula with the geometrical factor, (the De Broglie wavelength squared). The barrier penetration factor, and a residual factor of $S(E)$ as follows;

$$\sigma(E) \equiv \frac{S(E)}{E} exp(-2\pi\eta), \tag{B.2}$$

where

$$\eta = z_i z_j (e^2/\hbar v). \tag{B.3}$$

The quantity $exp(-2\pi\eta)$ is known as the Gamow penetration factor. The value of $S(E)$ at zero energy is known as the cross section factor, S_0.

At the temperatures and the densities relevant to the solar interior, the interacting particles obey a Maxwellian distribution in a time that is infinitesimal compared to the mean lifetime for a nuclear reaction. Therefore, one can average $< \sigma v >$ in Eq.(B.1), assuming a Maxwell-Boltzmann distribution, as following;

$$< \sigma v >= (\frac{8}{\pi\mu(k_BT)^3})^{1/2} f_0 \int_0^\infty S(E) exp(-2\pi\eta - E/k_BT)dE, \tag{B.4}$$

where μ is the reduced mass of the interacting particles, f_0 is a factor representing the electron screening as $f_0 = exp(0.188z_iz_j\zeta\rho^{1/2}T_6^{-3/2})$, where T_6 is the temperature in unit of 10^6K,$\zeta = [\Sigma_i(X_iZ_i^2/A_i + X_iZ_i/A_i)]^{1/2}$ and X_i is the mass fraction of nuclei of type i.

The average product of cross section terms velocity is given by

$$< \sigma v >= 1.3005 \times 10^{-15}[\frac{z_iz_j}{AT_6}]^{1/3} f_0 S_{eff} exp(-\frac{3E_0}{k_BT}), \tag{B.5}$$

where

$$S_{eff} = S_0[1 + \frac{Sk_BT}{36E_0} + \frac{S'(E_0 + \frac{35}{36}k_BT)}{S}]_{E=0}, \tag{B.6}$$

and $E_0 = 1.22(z_i^2z_j^2AT_6^2)^{1/3}$ MeV si a most probable energy of interaction. Here, $A = \frac{A_iA_j}{A_i+A_j}$ is the reduced atomic number. The temperature dependence of non-resonant thermonuclear reactions is determined by the above equation. An approximate dependence of nuclear reactions on the temperature is expressed by;

$$Rate \propto T^n \tag{B.7}$$

and the exponent n is;

$$n = (\frac{3E_0}{k_BT} - 2)/3. \tag{B.8}$$

The effective exponent by which a nuclear reaction rate or neutrino flux depends on temperature will differ from the value given in Eq.(B.7), in which E_0 is assumed to be calculated at a specific point in the Sun (e.g., the center). The effective exponent results from an average over the temperature-density profile of the Sun. The energy dependence of pp, ^{7}Be and ^{8}B neutrinos are shown in Eqs.(1.2) - (1.4).

Appendix C

Uncertainties in the Solar Standard Model

The calculation of the solar neutrino fluxes depends on the input parameters of the solar model such as nuclear reaction rate (e.g., S_{11}, S_{34} and S_{17}), solar radiative opacities and primordial abundances of heavy elements (Z). S_{11}, S_{34} and S_{17} are the cross section factors for the reactions of p+p, ^{3}He + ^{4}He and ^{7}Be + p, respectively, where subscripts on S defined by Eq.(B.2) represents the mass number of the interacting nuclei. What one really needs is the S factor around the energy near the Gamow peak (a few tens of keV). However, it is not able to measure the value in a laboratory, because the Coulomb potential barrier is too high ($\sim$ a few hundred keV). Therefore, the value is obtained by extrapolating the experimental data at a few hundred keV to the energy of the Gamow peak.

Table C.1 presents the logarithmic deviations of the neutrino fluxes with respect to each of the significant parameters. The deviations for the cross section factor, S_{17} which is related only to the ^{8}B neutrino flux are not listed. The only deviative that is significantly different from zero is $S_{17} = 1.00$ for ^{8}B neutrinos. For example, the ^{8}B neutrino flux has the dependence of Eq.(1.4). Table C.2 gives the fractional uncertainty (3σ) in each of solar neutrinos derived from the SSM calculated by Bahcall and Ulrich that is caused by each of the principal sources of uncertainty. In case of ^{8}B solar neutrinos, the main sources of uncertainty are S_{17} and Z/X.

Recently, Turck-Chièze proposed a new SSM independently of Bahcall and Ulrich.

Two SSM calculations obtained by Bahcall and Ulrich [1], and Turck-Chièze et al. [39] are shown in Table.5.1. The two SSM are in reasonably good agreement except of the ^{8}B neutrino flux. The main sources of their difference originate from choice of the S_{17} factor and the small difference of the central temperature which affect the ^{8}B neutrino flux (see Eq.(1.4)).

Appendix D

Definition of Effective Number of Hit PMTs

The effective number of hit PMTs (N_{eff}) is defined by;

$$N_{eff} = \frac{948 - N_{dead}(t_0)}{948 - N_{dead}(t)} \Sigma_i \mathrm{exp}(\frac{r_i}{l_m}) \mathrm{exp}(-\frac{R}{L_{abs}}) \frac{\cos\theta_i}{f(\theta_i)} \times \rho_{wall}, \qquad \text{(D.1)}$$

where r_i is the distance between PMT$_i$ and the vertex position of an event, l_m is the observed absorption length of the water, θ_i is the angle of the incident Čerenkov light with respect to the PMT$_i$ axis, and $f(\theta_i)$ represents the acceptance of PMT$_i$. ρ_{wall} is the relative density of PMTs on the each wall; defined by ρ_{wall}=1 for the barrel, and ρ_{wall}=1.06 for the top and bottom planes. R (=7.22m) and L_{abs} (=35m)are constants which shows the dimension of the detector and an arbitrary chosen standard of water transparency. The summention is performed for the PMTs with the residual time (t_i - time of flight from vertex to PMT) within ±20 nsec, where t_i is the measured time of PMT$_i$. This time width is determined by the time response of the PMT at the single photoelectron level (13 nsec FWHM).

The first factor in the definition of N_{eff} is the correction factor for the number of dead PMTs (no signal from its PMTs) where t and t_0 are the time when the event is detected and a chosen standard time (June,1988).

Figure Captions

Fig.1.1 : Proton - proton chain.

Fig.1.2 : CNO cycle.

Fig.1.3 : The energy spectrum of solar neutrinos predicted by the standard solar model (SSM) calculated by Bahcall and Ulrich. Most of the neutrinos have their energy less than 2 MeV.

Fig.1.4 : A possible correlation between the number of sunspots and the measured ^{37}Ar production rate by Homestake experiment.

Fig.1.5 : Plot showing the time variation of the ^{8}B solar neutrino signal in the KAM-II detector. Threshold for two earlier points is $E_e \geq 9.3$ MeV, while for the three later points $E_e \geq 7.5$ MeV. Each data point corresponds to approximately 200-day data.

Fig.1.6 : Present status of various $\nu_e \leftrightarrow \nu_\mu$ vacuum oscillation experiments at accelerators and reactors. So far, there is no compelling evidence for neutrino oscillations.

Fig.1.7 : The amplitude of $\sin^2 2\theta$ in matter near the resonant condition. The resonance width corresponds to $L_e/L_v = \cos 2\theta$.

Fig.1.8 : Fractional production rate of the solar neutrino as a function of radius from the center of the Sun. The ^{8}B neutrinos are generated inside the Sun compared to other sources.

Fig.1.9 : Electron density (N_e in unit of the Avogadro number N_A) in the Sun as a function of radius from the center of the Sun.

Fig.1.10 : The neutrino survival probability in case of $\sin^2 2\theta$=0.001 and $E/\Delta m^2$=6 $\times$ 10^5 MeV/eV^2 as a function of radius from the center of the Sun. One sees a sudden drop of the probability caused by resonant oscillation at R/R$_\odot$=0.3.

Fig.1.11 : The flavor eigenstate $\mid \nu_e >$ created at high density is nearly the same as the heavier mass eigenstate $\mid \nu_{2m} >$. As the electron density decrease slowly enough, the flavor state remains close to the mass eigenstate $\mid \nu_{2m} >$, the flavor state essentially becomes $\mid \nu_\mu >$ when it emerges from the Sun to a vacuum, because the effective mixing angle θ_m is close to the vacuum mixing angle θ.

Fig.1.12 : The contour line corresponding to 2 SNU on the plane of oscillation parameters ($\sin^2 2\theta$, Δm^2). The horizontal and vertical line represent the solutions which

satisfy the adiabatic criterion that the width of the resonance is large compared to the matter oscillation length, and the diagonal line satisfy the non-adiabatic solution in which the level crossing occurs between the mass eigenstates.

Fig.1.13 : Radial density in the Earth.

Fig.2.1 : Schematic view of the KAM-II detector with the water purification system, anti-counter and electronics hut.

Fig.2.2 : The attenuation length of light in pure water for wavelengths from 390 nm to 700 nm. Also shown is the Rayleigh scattering limit for short wavelength.

Fig.2.3 : Block diagram of the water purification system.

Fig.2.4 : Block diagram of the data acquisition electronics.

Fig.2.5 : Trigger efficiency as a function of total electron energy in the solar neutrino fiducial mass of 680 tons before and after the gain doubling.

Fig.2.6 : Change in the electron energy threshold during the period January, 1987 through April, 1990. The decreasing threshold energy is due to improvement of the sensitivity in that period. After May 1989, two different energy thresholds are used for the trigger. The lower threshold is 5.2 MeV.

Fig.2.7 : Schematic of the Nickel calibration system using gamma rays emitted from the reaction of Ni(n,γ) Ni.

Fig.2.8 : The measured gamma-ray spectra from the Cf + Ni (filled circle) and Cf source only (solid histograms) as a function of N_{eff}.

Fig.2.9 : The observed gamma-ray spectrum obtained by subtraction of the spectrum of the Cf source spectrum from the Cf + Ni spectrum. The solid histogram shows the corresponding spectrum calculated by the Monte Carlo simulation.

Fig.2.10 : The gain stability plotted is the relative value of the Ni(n,γ)Ni calibration runs in the interval between October, 1986 and April, 1990. The gain is stable within ± 2%.

Fig.2.11 : N_{eff} distribution of electrons from stopping muon decays (data points) together with that of the Monte Carlo simulation (solid histograms) which includes the energy resolution of the detector.

Fig.2.12 : The event rate as a function of time interval ΔT from the proceeding muon event. The solid line is the life time (18.4 ± 0.8 msec) obtained from the mixture

of short-lived spallation beta-decay products ^{12}B and ^{12}N. The spallation events with $E_e \geq 10$ MeV accompanied by the proceeding muons with pulse height above 20000 p.e. are selected.

Fig.2.13 : Energy distribution of the beta decays from the short-lived spallation products. The solid histogram shows the Monte Carlo simulated spectrum of beta decays for a mixture of ^{12}B and ^{12}N with a relative ratio of 0.85:0.15 consistent with the life time in Fig.2.12.

Fig.2.14 : Energy resolution as a function of total electron energy obtained by the Monte Carlo simulation before (dashed) and after (solid) the gain doubling.

Fig.2.15 : Measured distribution of collimated gamma rays as a function of $\cos\theta$ compared with that of the Monte Carlo simulation. The angle θ is defined as the angle between the reconstructed electron and the downward direction.

Fig.2.16 : Angular resolution as a function of total electron energy before (dashed) and after (solid) the gain doubling.

Fig.2.17 : (a) Distribution of the number of PMTs per unit of time residual as a function of the residual time for a typical well-reconstructed event. If all the measured times of the PMTs in one event are properly corrected for the time of flight from a correct vertex position, the distribution should peak sharply at the mean time residual.

(b) Same distribution as (a) but for one event with an incorrect vertex position.

Fig.2.18 : Vertex position resolution (1σ) of gamma rays from the Ni(n,γ)Ni source as a function of total electron energy before (open circle) and after (filled circle) the gain doubling, compared with the Monte Carlo simulation before (dashed) and after (solid) the gain doubling.

Fig.2.19 : Vertex position resolution of electrons generated by the Monte Carlo simulation before (dashed) and after (solid) the gain doubling.

Fig.3.1 : Neutrino survival probability P($\nu_e \rightarrow \nu_e$) as a function of $E/\Delta m^2$ obtained from the calculation of the MSW effect in the Sun in the case of $\sin^2 2\theta = 0.1$ (solid), 0.01 (dashed) and 0.001 (dotted).

Fig.3.2 : Energy spectrum of ^{8}B solar neutrinos at the Earth in the case of no oscillation (solid) and in the case of neutrino oscillation with ($\sin^2 2\theta$,Δm^2): (2×10^{-3},1.3×10^{-4}) for dashed line, (1.6×10^{-2},3.2×10^{-6}) for dotted line and (0.8,3.2×10^{-6}) for dotted-

dashed line.

Fig.3.3 : Neutrino survival probability that a neutrino born as a ν_e at the center of the Sun remains as ν_e, at each point in the Earth for $\sin^2 2\theta = 0.1$ and $E/\Delta m^2 = 2 \times 10^6$ MeV/eV^2. In the figure, the Sun is just under the observer.

Fig.3.4 : Neutrino survival probability as a function of $E/\Delta m^2$ for the case of $\sin^2 2\theta$ = 0.1, where a neutrino is assumed to be born as a ν_e at the center of the Sun. The solid line is obtained by taking into account only the MSW effect in the Sun. On the other hand, the dashed line includes the regeneration effect in the Earth.

Fig.3.5 : Feynman diagrams for the neutrino-electron scattering via the charged-current and the neutral-current.

Fig.3.6 : Energy distributions of recoil electrons scattered by ^{8}B solar neutrinos expected from the Monte Carlo simulation. The solid histograms take into account the energy resolution of the detector and the dashed ones do not include the effect.

Fig.3.7 : Expected energy spectra relative to the SSM prediction calculated by Bahcall and Ulrich in the case of neutrino oscillation parameters with ($\sin^2 2\theta$,Δm^2): (6.3×10^{-1},10^{-4}) for the solid line, (10^{-2},3.2×10^{-6}) for the dotted-dashed line, and (2×10^{-3},1.4×10^{-4}) for the dashed line, together with the data point.

Fig.3.8 : Expected relative neutrino fluxes as a function of $\cos \delta_{sun}$ in the case of ($\sin^2 2\theta$,Δm^2): (0.11,3.5×10^{-6}) for the solid line and (0.05,7.9×10^{-6}) for the dashed line, together with the data point.

Fig.3.9 : Calculated energy spectra of recoil electrons by ^{8}B solar neutrinos by the analytic expression of the energy resolution of the detector (solid histograms) and by the Monte Carlo simulation (filled circles).

Fig.3.10 : The contours on the oscillation parameter plane in the case of (a) KAM-II, (b) Homestake, and (c) the SAGE experiment. Each contour line corresponds to $0.1 \times$ SSM $\times$ i (i = 1,10) where SSM is the central value of the Bahcall and Ulrich's calculation. The calculation take into account the regeneration effect in the Earth as well as the MSW effect in the Sun.

Fig.4.1 : The observed event rate as a function of total electron energy for all events (○), events in fiducial volume (●), after spallation cut (◇) and after the remaining gamma-ray cut (◆): (a) before the gain doubling, (b) after the gain doubling. The solid curve

shows the expected event rate for ^{8}B solar neutrinos predicted by SSM calculated by Bahcall and Ulrich.

Fig.4.2 : Plot of the angle between the electron direction and a radius vector from the Sun ($\cos\theta_{sun}$) showing the signal from the Sun plus an isotropic background. This plot is for $E_e \geq 9.3$ MeV, and time period January,1987 through April, 1990. a total of 1040 detector-live days.

Fig.4.3 : (a) Same as Fig.4.2 but for the period January, 1987 through May, 1988, a total of 450 detector-live days. (b) Same as Fig.4.2 but for the period June, 1988 through April, 1990, a total of 590 detector-live days.

Fig.4.4 : (a) Differential electron energy distribution of the events scattered by ^{8}B solar neutrinos. The point in the interval above 14 MeV is sum of all events above 14 MeV. The dashed histogram is the best fit to the data of Monte Carlo simulation based on $\sigma(\nu_e e \rightarrow \nu_e e)$, the known shape of the neutrino flux from ^{8}B decay, and the energy resolution of the detector. The solid histogram has the area predicted by the SSM of Bahcall and Ulrich.

(b) The flux value relative to the SSM as a function of total electron energy (E_e). The plot shows the stability of the solar neutrino signal with electron energy, and is not dependent on the total flux prediction of the SSM, which is consequently indicated by SSM.

Fig.4.5 : The confidence-level contours at the 68% (hatched), 90% (solid line) and 95% (dashed line) for the allowed regions of the MSW solutions which are obtained by the only the total flux measured by KAM-II, relative to the central value of the SSM prediction calculated by Bahcall and Ulrich. Only the MSW effect in the Sun is folded in the figure and the theoretical uncertainty of the ^{8}B solar neutrino flux (37%) is not taken into account.

Fig.4.6 : Same as Fig.4.5 but obtained from both the total flux and the measured recoil electron energy spectrum.

Fig.4.7 : The "excluded" region obtained by the analysis of the shape of the recoil electron energy spectrum alone. These contours show the 68% (dashed) and 90% (solid) confidence levels for the "excluded" region which does not depend on the absolute flux value predicted by the SSM. The hatched region shows the allowed region.

Fig.4.8 : Same as Fig.4.2 but for (a) the daytime, (b) $\cos\delta_{sun}$ = 0.0 - 0.2, (c) $\cos\delta_{sun}$ = 0.2 - 0.4, (d) $\cos\delta_{sun}$ = 0.4 - 0.6, (e) $\cos\delta_{sun}$ = 0.6 - 0.8, (f) $\cos\delta_{sun}$ = 0.8 - 1.0.

Fig.4.9 : Measured solar neutrino fluxes relative to the averaged value (0.46 relative to the SSM prediction of Bahcall and Ulrich); (a) daytime, nighttime; (b) spring, summer, fall, winter; (c) periods I and II; (d) periods I and II, daytime; (e) periods I and II, nighttime.

Fig.4.10 : The "excluded" region obtained by KAM-II from the nighttime flux $\cos\delta_{sun}$ distribution (Fig.3.8). These contours show the 68% (dashed), 90% (solid) and 95% (hatched) confidence levels for the "excluded" region on the oscillation parameter plane. Note that these regions do not depend on the absolute value of the expected solar neutrino flux.

Fig.5.1 : The dotted region shows the 90% confidence level contour for the "allowed" region which is obtained from the total flux and the recoil-electron energy spectrum, measured in the KAM-II detector. The theoretical uncertainty of ^{8}B solar neutrino flux (37%) is not taken into account, and the central value of the ^{8}B solar neutrino flux by the SSM prediction of Bahcall and Ulrich is adopted in the analysis. The neutrino regeneration effect effect adds the allowed region of $7 \times 10^{-2} \leq \sin^2 2\theta \leq 6 \times 10^{-1}$ and $10^{-6} \leq \Delta m^2 \leq 10^{-5}$ eV^2. The hatched region shows the "excluded" region at 90% C.L. obtained by null Day/Night effect as shown in Fig.3.8 without any assumption on the absolute value of the solar neutrino flux. (Some following figures will be shown together with this excluded region.)

Fig.5.2 : The 90% C.L. allowed region obtained by the KAM-II (solid line) and Homestake experiment (dashed line). As the capture rate of the Homestake experiment, 2.3 ± 0.3 SNU is adopted. The adiabatic region of $\Delta m^2 \geq 10^{-4}$ eV^2 is mostly excluded by the non-overlapping of the two allowed regions.

Fig.5.3 : The 90% C.L. allowed region obtained by KAM-II (solid line) and the Homestake experiment (dashed line) for (a) with the expected ^{8}B solar neutrino flux increased by 37% and the expected ^{7}Be solar neutrino flux also increased by 15%, and (b) with the expected ^{8}B solar neutrino flux decreased by 37% and the expected ^{7}Be solar neutrino also decreased by 15%. Note that the allowed region for KAM-II in (b) is outside the triangular of the solid line (shaded region).

Fig.5.4 : The 90% C.L. allowed region obtained by the overlapping regions of KAM-II and Homestake experiment. The central value of each solar neutrino flux predicted by the SSM of Bahcall and Ulrich is assumed including the theoretical 3σ error of each neutrino flux. See Figs.5.2 and 5.3.

Fig.5.5 : The 90% C.L. allowed region obtained by KAM-II (shaded region) and Homestake experiment (dashed line), assuming the central value of each neutrino flux from the SSM calculated by Turck-Chièze. The measured neutrino fluxes relative to the SSM prediction are 0.70 ± 0.08(stat.) $\pm$ 0.09(sys.) for KAM-II and 0.40 ± 0.05 (stat.) for Homestake experiment.

Fig.5.6 : The iso-SNU contours of the ^{71}Ga experiment on the oscillation parameter plane without the neutrino regeneration effect in the Earth. The contour from inside shows 10, 20, 40, 60, 80, 100 and 120 SNU.

Fig.5.7 : The iso-SNU contours (10, 20, 40, 60, 80 and 100 SNU from inside) of the ^{71}Ga experiment (dotted), together with the 90% C.L. allowed regions of KAM-II (solid) and Homestake experiment (dashed) without the neutrino regeneration effect. The shaded region shows overlapping region allowed by KAM-II and the Homestake experiment. The SSM of Bahcall and Ulrich is assumed here.

Fig.5.8 : The iso-SNU contours of the ^{71}Ga experiment (dotted) together with the 90% C.L. allowed regions of KAM-II (solid) and Homestake experiment (dashed) for (a) with the ^{8}B solar neutrino flux increased by 37% and the ^{7}Be solar neutrino flux also increased by 15%, and for (b) with the ^{8}B solar neutrino flux decreased by 37% and the ^{7}Be solar neutrino flux also decreased by 15%. The contours of the ^{71}Ga experiment from inside shows 10, 20, 40, 60 and 80 SNU. The shaded region shows overlapping region allowed by KAM-II and the Homestake experiment. The SSM of Bahcall and Ulrich is assumed here.

Fig.5.9 : The iso-SNU contours of the ^{71}Ga experiment (SAGE) on the oscillation parameter plane with the neutrino regeneration effect in the Earth. The contours from inside shows 10, 20, 30, 40, 60, 80, 100 and 120 SNU. In the region of $\sin^2 2\theta \geq 0.1$ and $10^{-8} \leq \Delta m^2 \leq 10^{-6}$ eV^2, the expected neutrino flux is increased by about 10 SNU compared to Fig.5.6 due to the regeneration effect.

Fig.5.10 : The 90% C.L. allowed region obtained by KAM-II (solid line) and Homes-

take experiment (dashed line) with the neutrino regeneration effect in the Earth for (a) with the expected ^{8}B solar neutrino flux increased by 37% and the expected ^{7}Be solar neutrino flux also increased by 15%, and (b) with the expected ^{8}B solar neutrino flux decreased by 37% and the expected ^{7}Be solar neutrino also decreased by 15%. Note that the allowed region for KAM-II in (b) is outside the triangular of the solid line. The shaded region shows overlapping region allowed by KAM-II and the Homestake experiment.

Fig.5.11 : The iso-SNU contours of the ^{71}Ga experiment (dotted) and 90% C.L. allowed region of KAM-II (solid) and the ^{37}Cl experiment (dashed) with the neutrino regeneration effect in the Earth. The shaded region shows overlapping region allowed by KAM-II and the Homestake experiment.

Fig.5.12 : The expected energy spectrum of recoil electrons for Super-Kamiokande, assuming only the MSW effect in the Sun in the case of ($\sin^2 2\theta$, Δm^2): (1)($0.01, 3\times10^{-6}$), (2)($0.1, 4\times10^{-7}$), (3)($0.5, 1\times10^{-7}$) and (4)($0.7, 5\times10^{-7}$). The expected statistical error bars in the figure are estimated, assuming 5 years of Super-Kamiokande operation with the SSM prediction of Bahcall and Ulrich.

References

[1] J.N.Bahcall and R.L.Sears, Annu. Rev. Astron. Astrophys. **10**(1972)25, J.N.Bahcall , Rev. of Mod. Phys. **50**(1978)881., J.N.Bahcall et al., Rev. of Mod. Phys. **54**(1982)767., J.N.Bahcall and R.K.Ulrich, Rev. of Mod. Phys. **60**(1988)297.

[2] J.N.Bahcall, *Neutrino Astrophysics* (Cambridge Univ. Press, Cambridge, 1989).

[3] R.Davis, Jr. et al., Phys. Rev. Lett. **20**(1968)1205.

[4] K.S.Hirata et al., Phys. Rev. Lett. **63**(1989)16.

[5] K.S.Hirata et al., Phys. Rev. Lett. **65**(1990)1297.

[6] K.S.Hirata et al., Phys. Rev. Lett. **65**(1990)1301.

[7] K.S.Hirata et al., Phys. Rev. Lett. **66**(1990)9.

[8] K.Lande, in Proceedings of XXVth International Conference on High Energy Physics, Singapore, 1990. edited by K.K.Phua and Y.Yamaguchi (World Scientific, Singapore, 1991).

[9] A.I.Abazov et al., Phys. Rev. Lett. **67**(1991)3332.

[10] V.Barger, R.J.N.Phillips and K.Whisnant, Phy. Rev. Lett. **65**(1990)3084.

[11] A.Acker, S.Pakvasa and J.Pantaleone, Phy. Rev. **D43**(1991)1754.

[12] S.P.Mikheyev and A.Yu.Smirnov, Sov. J. Nucl. Phys. **42**(1985)913., L.Wolfenstein, Phys. Rev. **D17**(1978)2369; ibid. **D20**(1979)2634.

[13] E.L.Cicernos, Astro. Space Sci. **10**(1971)87.

[14] J.F.Wilkerson et al., *in Neutrino 90*, Proceedings of the 14th International Conference on Neutrino Physics and Astrophysics, Geneva, Switzerland, 1990, edited by J.Panam and K.Winter (North-Holland, Amsterdam 1990).

[15] M.B.Volshin, M.I.Vysotskii and L.Okun, Sov. J. Nucl. Phys. **44**(1986)440.

[16] B.Barbieri and G.Fiorentini, Nucl. Phys. **304** (1988)909.

[17] R.Davis, Jr. Proceedings of Seventh Workshop on Grand Unification ICOBAN'86 Toyama, Japan, edited by J.Arafune (World Scientific, Singapore).

[18] A.V.Kyuldjev, Nucl. Phys. **B243**(1984)387.,

[19] L.A.Ahrens et al., Phys.Rev. **D41**(1990)3301.

[20] K.Hirata et al., Phys. Rev. Lett. **58**(1987)1490.

[21] R.M.Bionta et al., Phys. Rev. Lett. **58**(1987)1494.

[22] I.Goldmann et al., Phys. Rev. Lett. **60**(1988)1789., J.M.Lattimer et al., Phys. Rev. Lett. **61**(1988)23., R.Barbieri and R.N.Mohapatra, Phys. Rev. Lett. **61**(1988)27.

[23] C.S.Lim and W.J.Marciano, Phys. Rev. **D37**(1988)1368.

[24] E.Kh.Akhmedov et al., Phys. Lett. **231B**(1988)64.

[25] K.S.Babu, R.N.Mohapatra and I.Z.Rothstein, University of Maryland Report UMDHEP-91-246 (1991).

[26] J.N.Bahcall, N.Cabibbo and A.Yahil, Phys. Rev. Lett. **28**(1972)316.

[27] K.S.Hirata et al., Phys. Rev. Lett. **58**(1987)1490.

[28] F.Dydak, in Proceedings of XXVth International Conference on High Energy Physics, Singapore, 1990. edited by K.K.Phua and Y.Yamaguchi (World Scientific, Singapore, 1991).

[29] J.Faulkner and R.L.Gilliland, Astro. Phys. J. **299**(1985)994., L.M.Krauss et al., Astro. Phys. J. **299**(1985)1001.

[30] K.S.Hirata et al., Astro. phys. J. **359**(1990)574.

[31] T.Kirsten, *in Neutrino 90*, Proceedings of 14th International Conference on Neutrino Physics and Astrophysics, Geneva, Switzerland, 1990, edited by J.Panam and K.Winter (North-Holland, Amsterdam, 1990).

[32] V.N.Gavrin, *in Neutrino 90*, Proceedings of the 14th International Conference on Neutrino Physics and Astrophysics, Geneva, Switzerland, 1990, edited by J.Panam and K.Winter (North-Holland, Amsterdam, 1990).

[33] T.Yanagida, in Proceedings of the Workshop on Unified Theory and Baryon Number in the Universe, edited by O.Sawada and A.Sugamoto (KEK, Tsukuba, 1979), M.Gell-Mann, P.Rammond and S.Slansky: *Supergravity* edited by P.van Nieuwenhuizen and D.Freedman (North-Holland, Amsterdam, 1979).

[34] V.Barger et al., Phys. Rev. **D22**(1980)2718., P.Langacker et al., CERN-TH-4421 (1986).

[35] K.E.Bergkvist, Proceedings of the 1985 International Symposium on Lepton and Photon Interactions at High Energies. (Kyoto, Japan).

[36] S.Hiroi, H.Sakuma, T.Yanagida and M.Yoshimura, KEK-TH-166(1987).

[37] T.H.Jordan and D.L.Anderson, Geophys. J. R. Astr. Soc. **36**(1974)411.

[38] A.J.Baltz et al., Phy. Rev. **D35**(1987)528.

[39] J.N.Bahcall and B.R.Holstein, Phys. Rev. **C33**(1986)2121.

[40] E.D.Commins and P.H.Buckshaum, *Weak Interactions of Leptons and Photons*, (Cambridge University Press, 1983).

[41] S.Turck-Chièze et al., Astrophys. J., **335**(1988)415.

[42] K.S.Hirata et al., Phys. Rev. **D44**(1991)2241.

[43] Y.Totsuka, Tokyo Univ. Report No. ICRR-Report-227-90-20 (1990). *(unpublished)*

[44] Sudbury Neutrino Observatory Proporsal, SNO-87-12, (1987).

Table 1.1 Solar Parameters

Luminosity	3.86×10^{33} erg/sec
Mass ($M_\odot$)	1.99×10^{33} g
Radius ($R_\odot$)	6.96×10^{10} cm
Moment of Inertia	7.00×10^{53} gcm^2
Depth of convective zone	$0.26 \times R_\odot$
Age	4.6×10^9 year
Central density	148 g/cm^3
Central temperature	1.56×10^7 K
Central hydrogen abundance	$0.340 \times M_\odot$
Surface temperature	5.77×10^3 K
Primordial helium abundance (Y)	0.271
Primordial heavy element (Z/X)	0.0277
Fraction of energy from pp chains	0.984
Fraction of energy from CNO cycle	0.016

Table 1.2 Total neutrino fluxes

Neutrino Source	Flux (10^{10} cm^{-2} sec^{-1})
pp	6.0 (1 ± 0.02)
pep	0.014 (1 ± 0.05)
hep	8×10^{-7}
^{7}Be	0.47 (1 ± 0.15)
^{8}B	5.8×10^{-4} (1 ± 0.37)
^{13}N	0.06 (1 ± 0.50)
^{15}O	0.05 (1 ± 0.58)
^{17}F	5.2×10^{-4} (1 ± 0.46)

Table 1.3 Reaction parameter for the pp cheain and CNO cycle

Reaction	Q (MeV)	S_0 (keV barns)	dS/dE (barns)
$p(p,e^{+}\ \nu_e)^{2}H$	1.442	$4.07(1 \pm 0.051) \times 10^{-22}$	4.52×10^{-24}
$p(p,e^{-},\nu_e)H$	1.422		
$^{2}H(p,\gamma)^{3}He$	5.494	2.5×10^{-4}	7.9×10^{-6}
$^{3}He(^{3}He,2p)^{4}He$	12.860	$5.15(1 \pm 0.17) \times 10^{3}$	-0.9
$^{3}He(^{4}He,\gamma)^{7}Be$	1.586	$0.54(1 \pm 0.06)$	-3.1×10^{-4}
$^{7}Be(e^{-},\nu_e)^{7}Li$	0.862		
	0.384		
$^{7}Li(p,\alpha)^{4}He$	17.347	$52(1 \pm 0.5)$	0
$^{7}Be(p,\gamma)^{8}B$	0.137	$0.0243(1 \pm 0.22)$	-3×10^{-5}
$^{8}B(e^{+},\nu_e)^{8}Be^{*}$	17.980		
$^{8}Be^{*}(\alpha)^{4}He$			
$^{3}He(p,e^{+}\nu_e)^{4}He$	19.795	8×10^{-20}	
$^{12}C(p,n)^{13}N$	1.943	$1.45(1 \pm 0.15) \times 10^{-3}$	2.45×10^{-3}
$^{13}N(e^{+},\nu_e)^{13}C$	2.221		
$^{13}C(p,\gamma)^{14}N$	7.551	$5.50(1 \pm 0.15) \times 10^{-3}$	1.34×10^{-2}
$^{14}N(p,\gamma)^{15}O$	7.297	$3.32(1 \pm 0.12) \times 10^{-3}$	-5.91×10^{-3}
$^{15}O(e^{+},\nu_e)^{15}N$	2.754		
$^{15}N(p,\gamma)^{16}O$	12.128	$6.4(1 \pm 0.09) \times 10^{-2}$	3×10^{-2}
$^{15}N(p,\alpha)^{12}C$	4.966	$78.0(1 \pm 0.17)$	351
$^{16}O(p,\gamma)^{17}F$	0.600	$9.4(1 \pm 0.16) \times 10^{-3}$	-2.3×10^{-2}
$^{17}F(e^{+},\nu_e)^{17}O$	2.762		

Table 1.4 The capture rate of ^{37}Cl and ^{71}Ga detector

Detector	^{37}Cl	^{71}Ga
Neutrino Source	Capture rate (SNU)	Capture rate (SNU)
pp	0.0	70.8
pep	0.2	3.0
hep	0.03	0.06
^{7}Be	1.1	34.3
^{8}B	6.1	14.0
^{13}N	0.1	3.8
^{15}O	0.3	6.1
^{17}F	0.003	0.06
Total	7.9	132

Table 3.1 **Fraction of the production rate for solar neutrinos**

$R/R_\odot$	pp neutrino	^{7}Be neutrino	$R/R_\odot$	^{8}B neutrino
0.02	0.008	0.051	0.01	0.070
0.04	0.034	0.116	0.02	0.310
0.06	0.106	0.259	0.03	0.350
0.08	0.204	0.301	0.04	0.190
0.10	0.179	0.153	0.05	0.06
0.12	0.146	0.074	0.06	0.02
0.14	0.111	0.032	0.08	0.0
0.16	0.063	0.009	0.09	0.0
0.18	0.039	0.003	0.10	0.0
0.20	0.038	0.001	0.11	0.0
0.22	0.029	0.0	0.12	0.0
0.24	0.016	0.0	0.13	0.0
0.26	0.010	0.0	0.14	0.0
0.28	0.008	0.0	0.15	0.0
0.30	0.012	0.0	0.16	0.0

Table 4.1 Comparison neutrino flux of day-night sample

$\cos\delta_{sun}$	Flux (isotropic background)	Flux (M.C.)	difference
< 0 (Day)	0.91 ± 0.15	$0.94^{+0.16}_{-0.15}$	+3.6%
0 - 0.2	$1.23^{+0.41}_{-0.37}$	$1.28^{+0.41}_{-0.38}$	+3.5%
0.2 - 0.4	$1.03^{+0.37}_{-0.34}$	$1.08^{+0.36}_{-0.34}$	+5.3%
0.4 - 0.6	$0.98^{+0.32}_{-0.30}$	$0.99^{+0.32}_{-0.28}$	+1.1%
0.6 - 0.8	$0.70^{+0.33}_{-0.30}$	$0.69^{+0.34}_{-0.29}$	-0.16%
0.8 - 1.0	$1.24^{+0.37}_{-0.35}$	$1.15^{+0.38}_{-0.35}$	-7.9%

Table 5.1 Comparison between Bahcall and Ulrich and Turck-Chièze

	Bahcall and Ulrich	Turck-Chièze et al.
S factor	keV barn	keV barn
S_{11}	4.07×10^{-22}	4.07×10^{-22}
S_{34}	0.54	0.54
S_{17}	0.0243	0.021
Solar parameter		
$R/R_\odot$ bottom convective zone	0.723	0.730
$M/M_\odot$ bottom convective zone	0.980	0.981
T (K) at center	1.56×10^7	1.55×10^7
T (K) bottom convective zone	2.11×10^6	2.04×10^6
ρ (g/cm^3) at center	148	147.7
ρ (g/cm^3) bottom convective zone	0.154	0.153
Neutrino Flux	$\times 10^{10}$cm^{-2}	$\times 10^{10}$cm^{-2}
pp	$6.0(1 \pm 0.02)$	$5.98(1 \pm 0.03)$
pep	1.40×10^{-2}	1.30×10^{-3}
^{7}Be	4.7×10^{-2}	4.18×10^{-1}
^{8}B	$5.8 \times 10^{-4}(1 \pm 0.37)$	$3.8 \times 10^{-4}(1 \pm 0.24)$

Table 5.2 **Parameters for Super-Kamiokande and for KAM-II**

Parameters	Super-Kamiokande	KAM-II
Total size	41m (height) × 39m (ϕ)	16m (height) × 19m (ϕ)
Total mass	50,000t	4,500t
Fiducial mass	22,000t	680t
Tickness of anti-counter	2m	1.2-1.5m
Number of PMTs	11,200	948
Photosensitive coverage	40%	20%
Energy resolution	$14\%/\sqrt{E/10MeV}$	$20\%/\sqrt{E/10MeV}$
Position resolution	50cm for 10MeV e^-	110cm for 10MeV e^-
Angular resolution	27 deg for 10MeV e^-	27 deg for 10MeV e^-
Trigger energy	4~5MeV	5.2MeV
Analysis energy threshold	5MeV	7.5MeV

Table C.1 Calculated partial derivations of neutrino fluxes

Source	S_{11}	S_{33}	S_{34}	S_{14}	$L_\odot$	$R_\odot$	Z/X	Age
pp	+0.14	+0.03	-0.06	-0.02	+0.73	+0.01	-0.08	-0.07
pep	-0.17	+0.05	-0.09	-0.02	+0.87	+0.21	-0.17	+0.00
hep	-0.08	-0.45	-0.08	-0.01	+0.12	-0.09	-0.22	-0.11
^{7}Be	-0.97	-0.43	+0.86	-0.00	+0.34	+ 0.22	+0.58	+0.69
^{8}B	-2.59	-0.40	+0.81	+0.01	+6.76	+0.48	+1.27	+1.28
^{13}N	-2.53	+0.02	-0.05	+0.85	+5.16	+0.28	+1.86	+1.01
^{15}O	-2.93	+0.02	-0.05	+1.00	+5.94	+0.49	+2.03	+1.27
^{17}F	-2.94	+0.02	-0.05	+0.01	+6.25	+0.37	+2.09	+1.29

(c.f. $\partial \ln\phi_{pp}/\partial \ln S_{11} = +0.14$)

Table C.2 Uncertainties for the neutrino fluxes

Source	Total	pp	^{3}He+^{3}He	^{3}He+^{4}He	^{7}Be+p	^{14}N+p	Z/X	Opacity
pp	0.02	0.01	0.00	0.00	0.00	0.01	0.01	0.00
pep	0.05	0.01	0.00	0.01	0.00	0.01	0.03	0.02
hep		0.00	0.07	0.00	0.00	0.00	0.03	0.00
^{7}Be	0.15	0.05	0.07	0.05	0.00	0.00	0.11	0.04
^{8}B	0.37	0.12	0.06	0.05	0.22	0.00	0.25	0.08
^{13}N	0.50	0.12	0.00	0.00	0.00	0.30	0.38	0.03
^{15}O	0.56	0.14	0.00	0.00	0.00	0.36	0.42	0.06
^{17}F	0.46	0.14	0.00	0.00	0.00	0.00	0.44	0.06

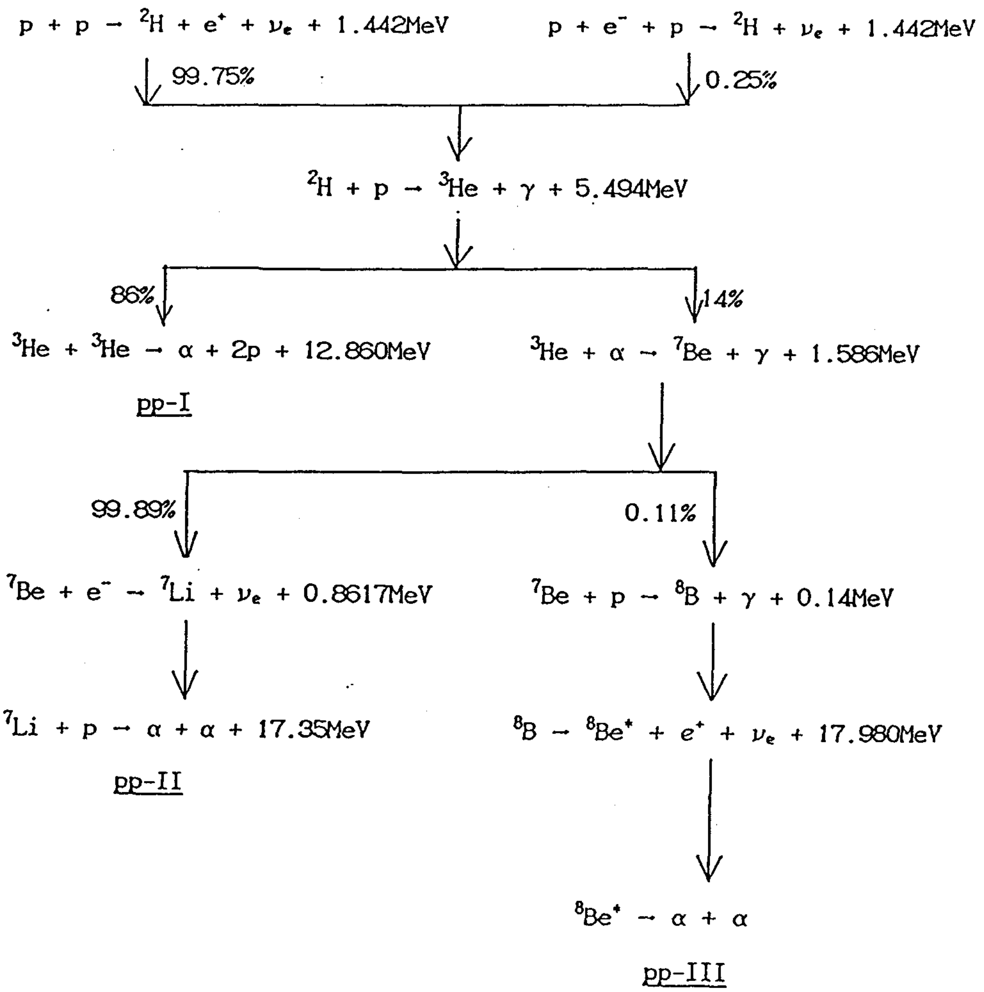
p + p → ²H + e⁺ + νₑ + 1.442MeV
p + e⁻ + p → ²H + νₑ + 1.442MeV
99.75%
0.25%
²H + p → ³He + γ + 5.494MeV
86%
14%
³He + ³He → α + 2p + 12.860MeV
pp-I
³He + α → ⁷Be + γ + 1.586MeV
99.89%
0.11%
⁷Be + e⁻ → ⁷Li + νₑ + 0.8617MeV
⁷Be + p → ⁸B + γ + 0.14MeV
⁷Li + p → α + α + 17.35MeV
pp-II
⁸B → ⁸Be* + e⁺ + νₑ + 17.980MeV
⁸Be* → α + α
pp-III

Fig. 1.1

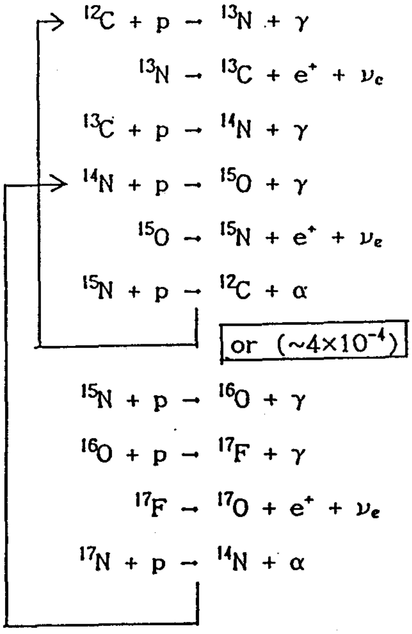
$^{12}C + p \rightarrow {}^{13}N + \gamma$
$^{13}N \rightarrow {}^{13}C + e^+ + \nu_e$
$^{13}C + p \rightarrow {}^{14}N + \gamma$
$^{14}N + p \rightarrow {}^{15}O + \gamma$
$^{15}O \rightarrow {}^{15}N + e^+ + \nu_e$
$^{15}N + p \rightarrow {}^{12}C + \alpha$
or $(\sim 4\times 10^{-4})$
$^{15}N + p \rightarrow {}^{16}O + \gamma$
$^{16}O + p \rightarrow {}^{17}F + \gamma$
$^{17}F \rightarrow {}^{17}O + e^+ + \nu_e$
$^{17}N + p \rightarrow {}^{14}N + \alpha$

Fig. 1.2

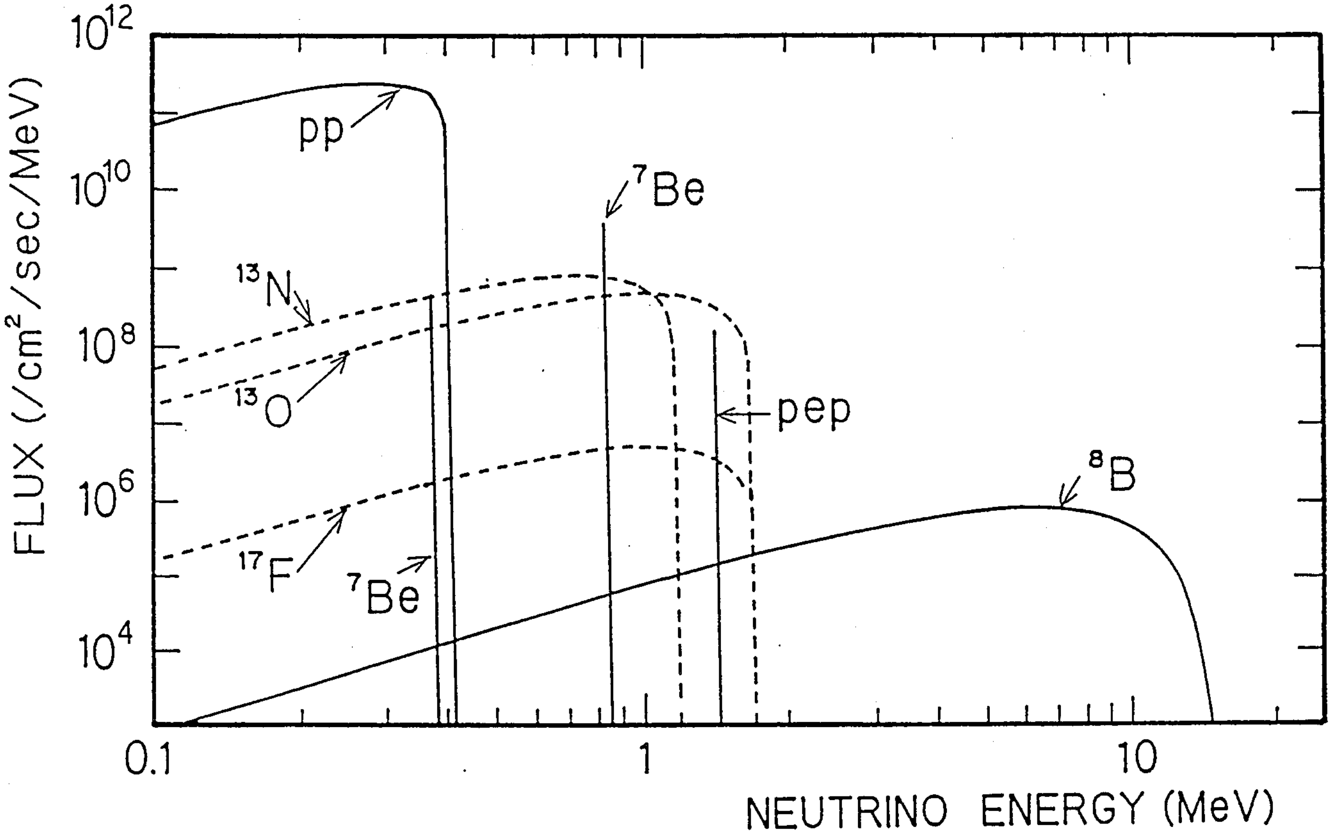
10^{12}
10^{10}
10^{8}
10^{6}
10^{4}
FLUX (/cm^2/sec/MeV)
0.1
1
10
NEUTRINO ENERGY (MeV)
pp
^{7}Be
^{13}N
^{13}O
pep
^{8}B
^{17}F
^{7}Be

Fig. 1.3

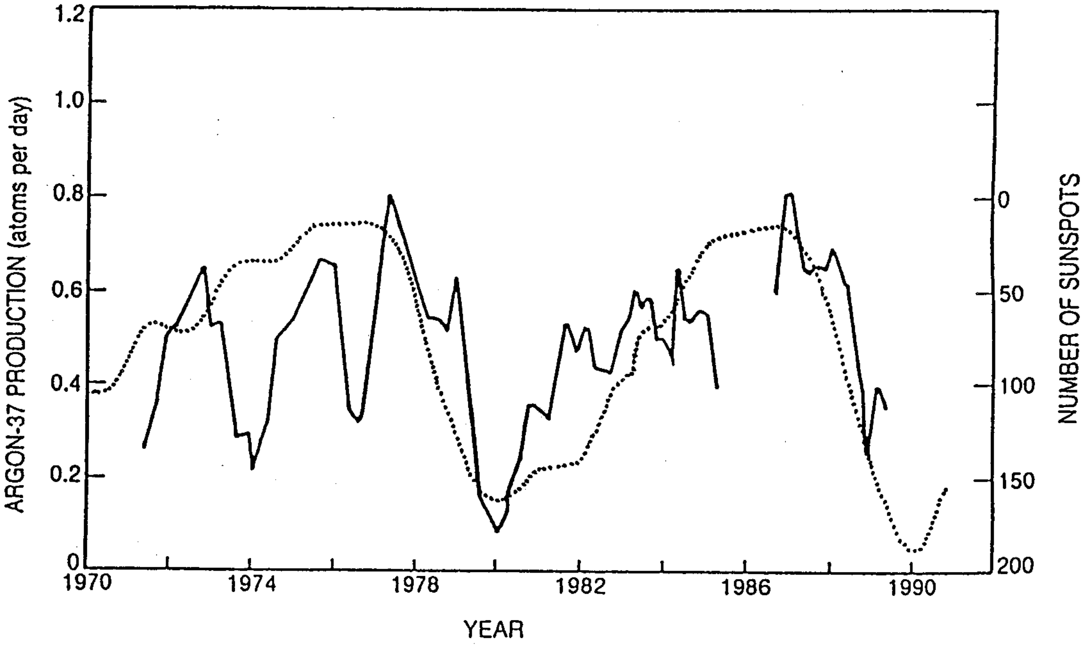

1.2
1.0
0.8
0.6
0.4
0.2
0
ARGON-37 PRODUCTION (atoms per day)
1970
1974
1978
1982
1986
1990
YEAR
0
50
100
150
200
NUMBER OF SUNSPOTS

Fig. 1.4

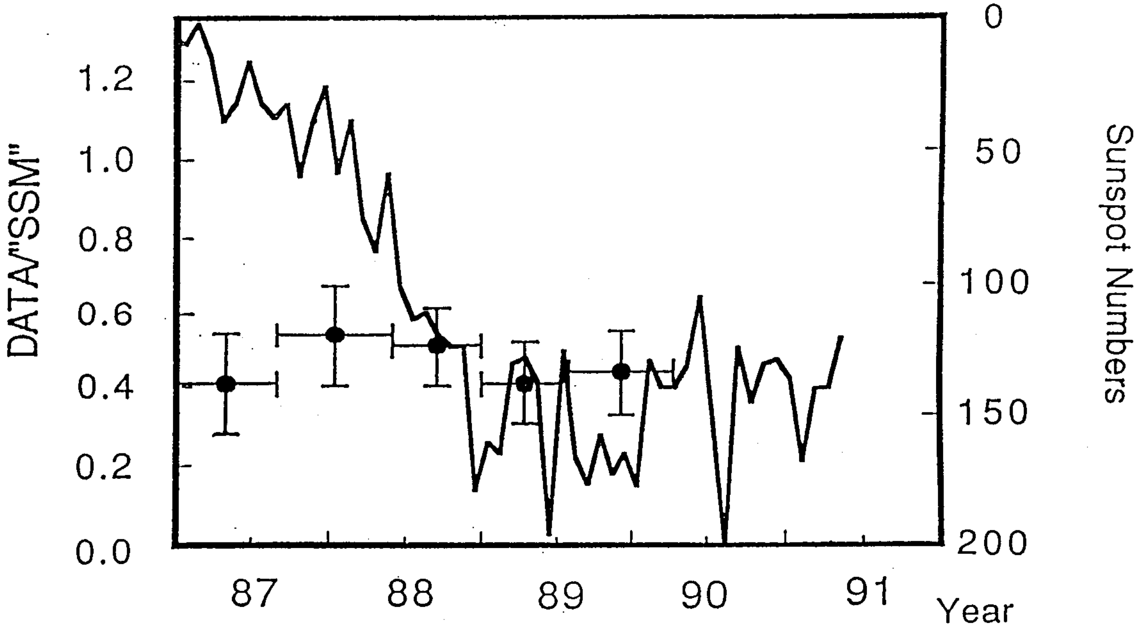
DATA/"SSM"
1.2
1.0
0.8
0.6
0.4
0.2
0.0
0
50
100
150
200
Sunspot Numbers
87
88
89
90
91
Year

Fig. 1.5

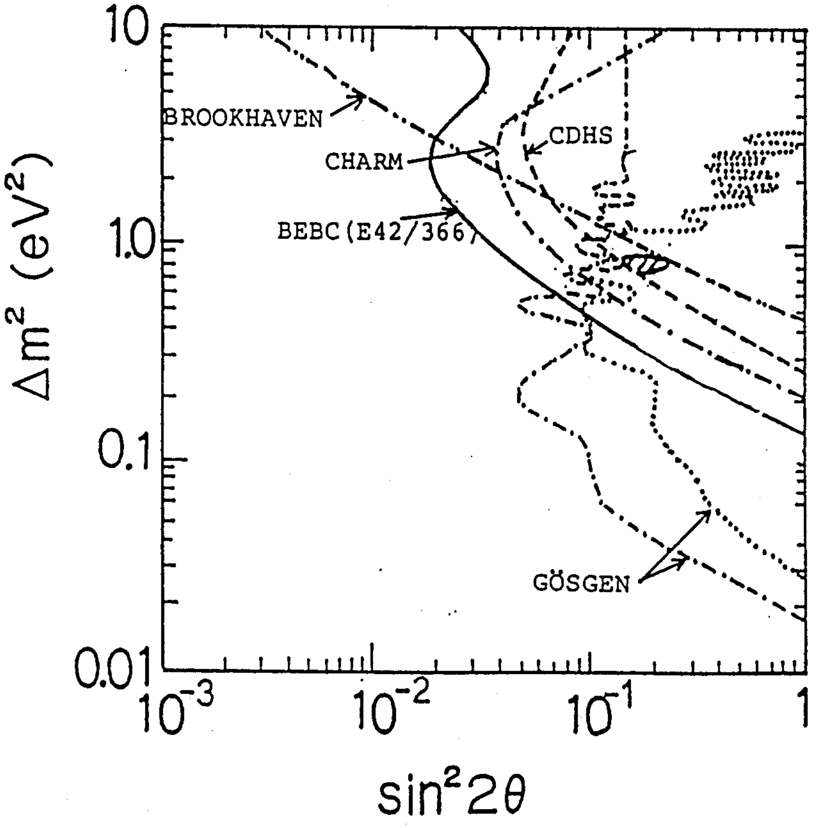
10
1.0
0.1
0.01
Δm^2 (eV^2)
10^{-3}
10^{-2}
10^{-1}
1
$\sin^2 2\theta$
BROOKHAVEN
CHARM
BEBC (E42/366)
CDHS
GÖSGEN

Fig. 1.6

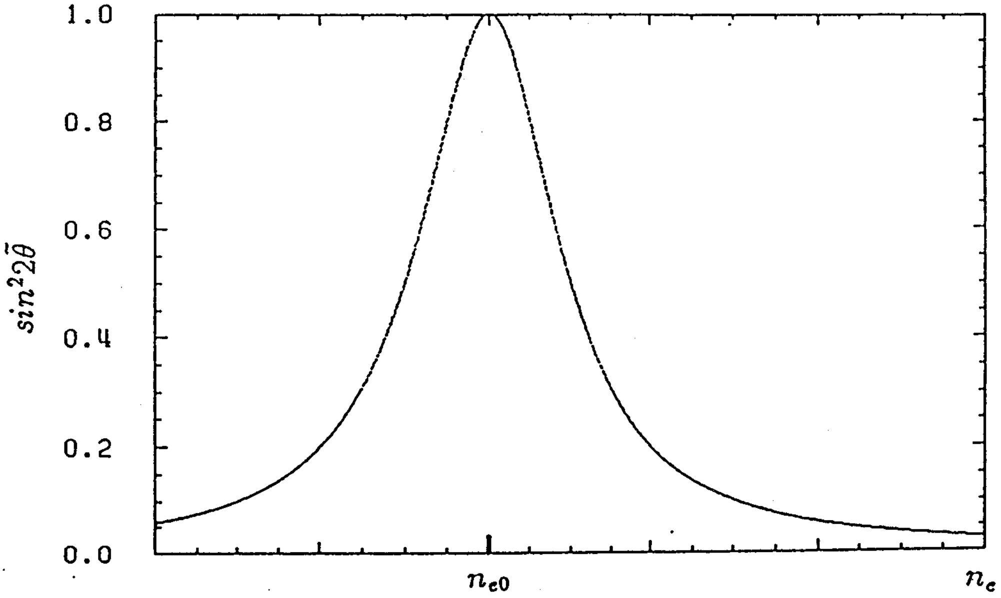

Fig. 1.7

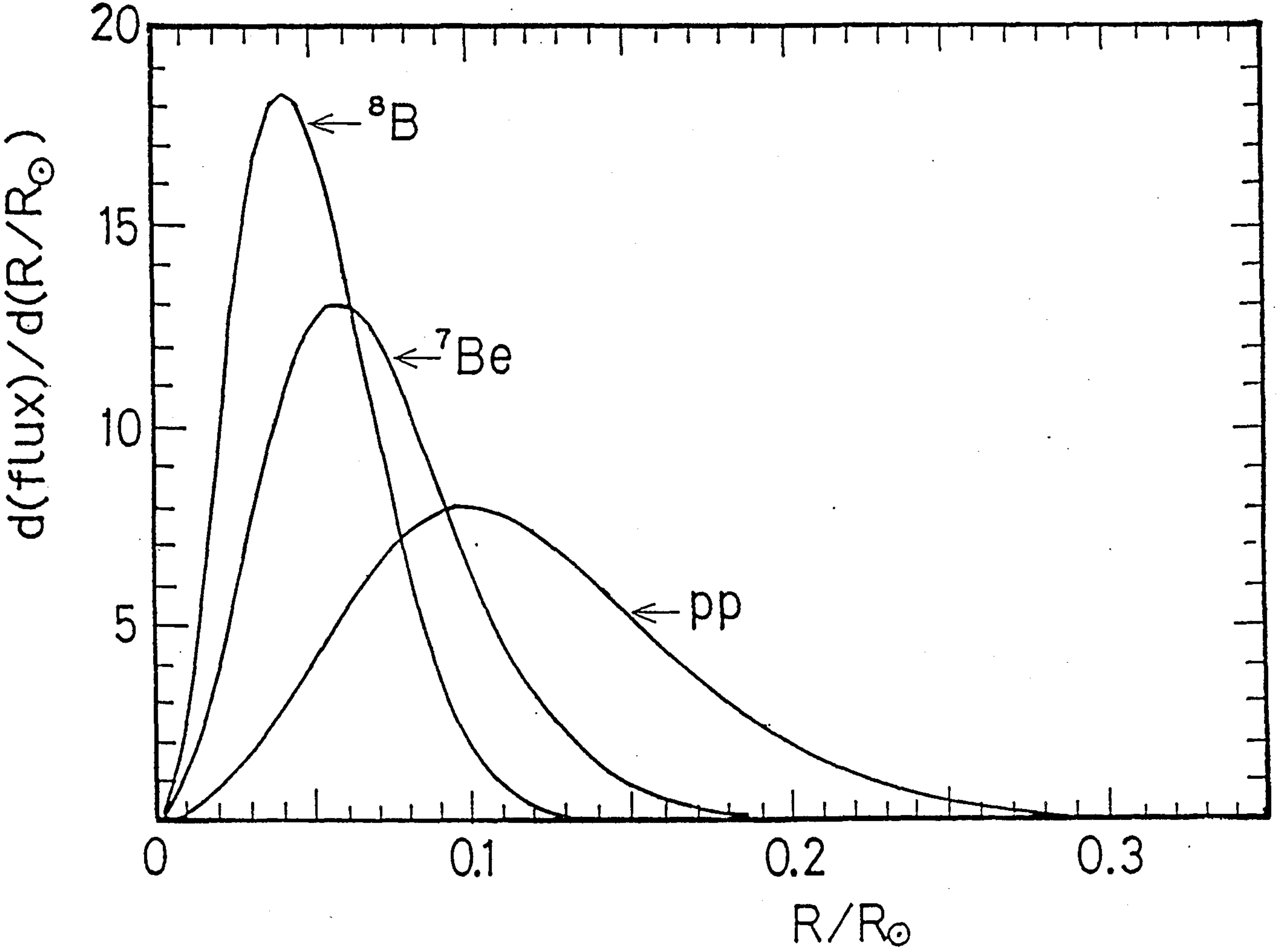

Fig. 1.8

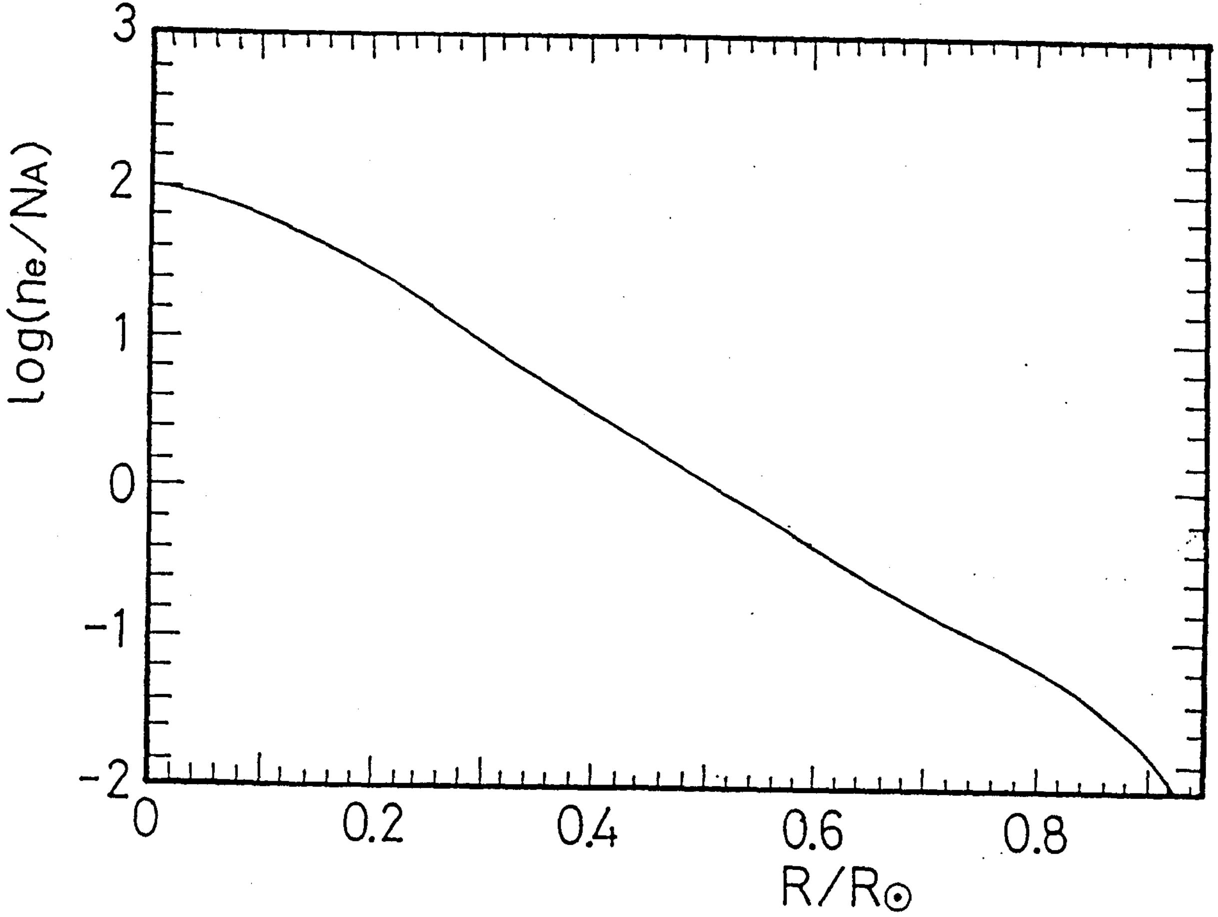

Fig. 1.9

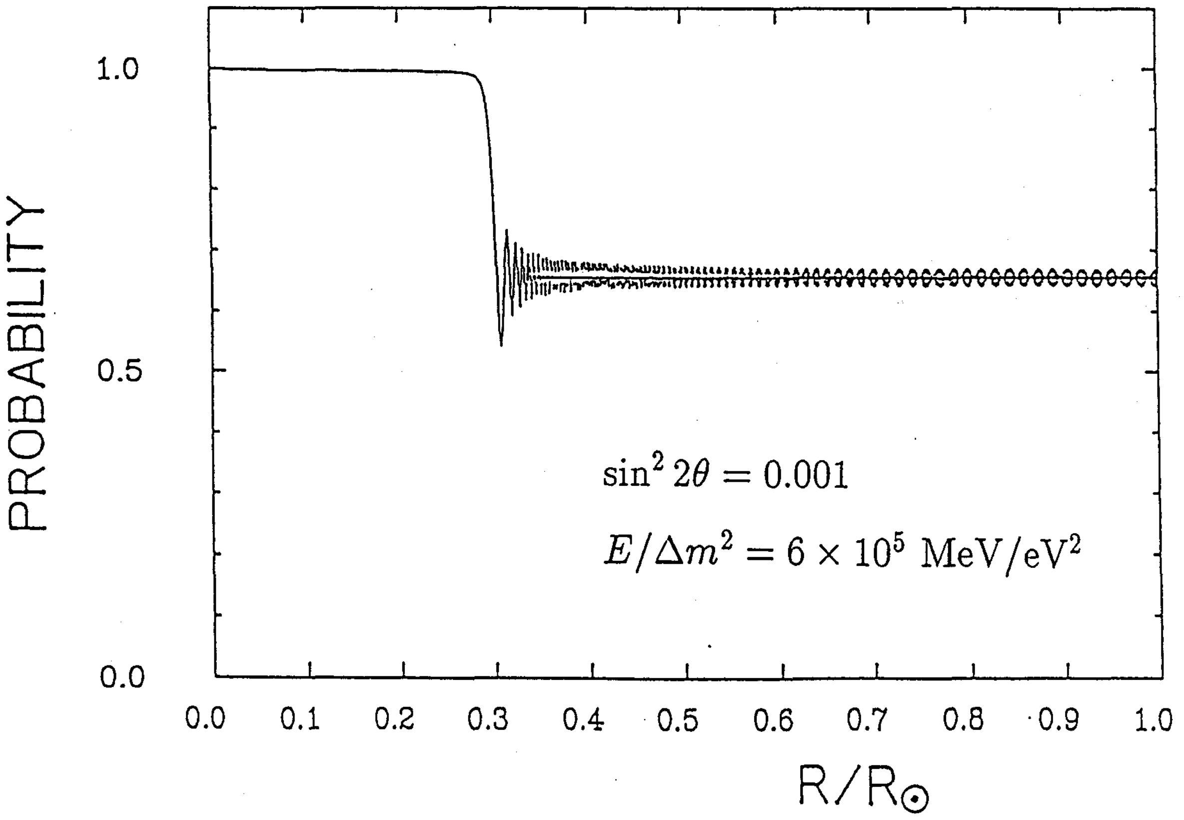
PROBABILITY
1.0
0.5
0.0
0.0
0.1
0.2
0.3
0.4
0.5
0.6
0.7
0.8
0.9
1.0
$R/R_\odot$
$\sin^2 2\theta = 0.001$
$E/\Delta m^2 = 6 \times 10^5$ MeV/eV^2

Fig. 1.10

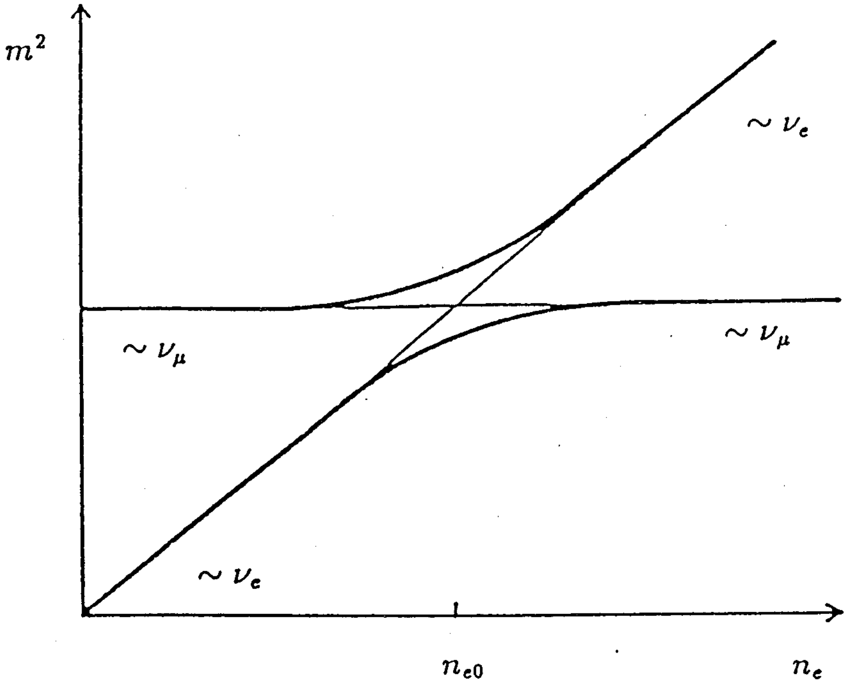

Fig. 1.11

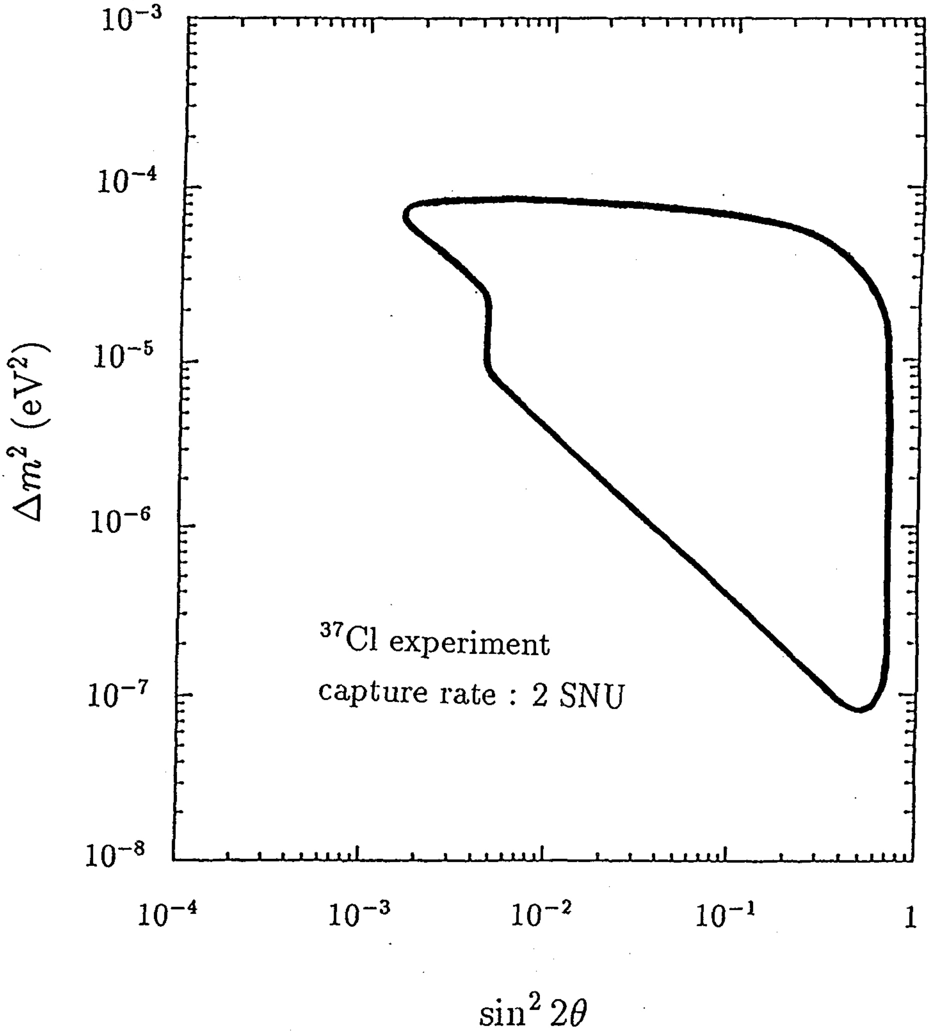
10^{-3}
10^{-4}
10^{-5}
10^{-6}
10^{-7}
10^{-8}
Δm^2 (eV^2)
^{37}Cl experiment
capture rate : 2 SNU
10^{-4}
10^{-3}
10^{-2}
10^{-1}
1
$\sin^2 2\theta$

Fig. 1.12

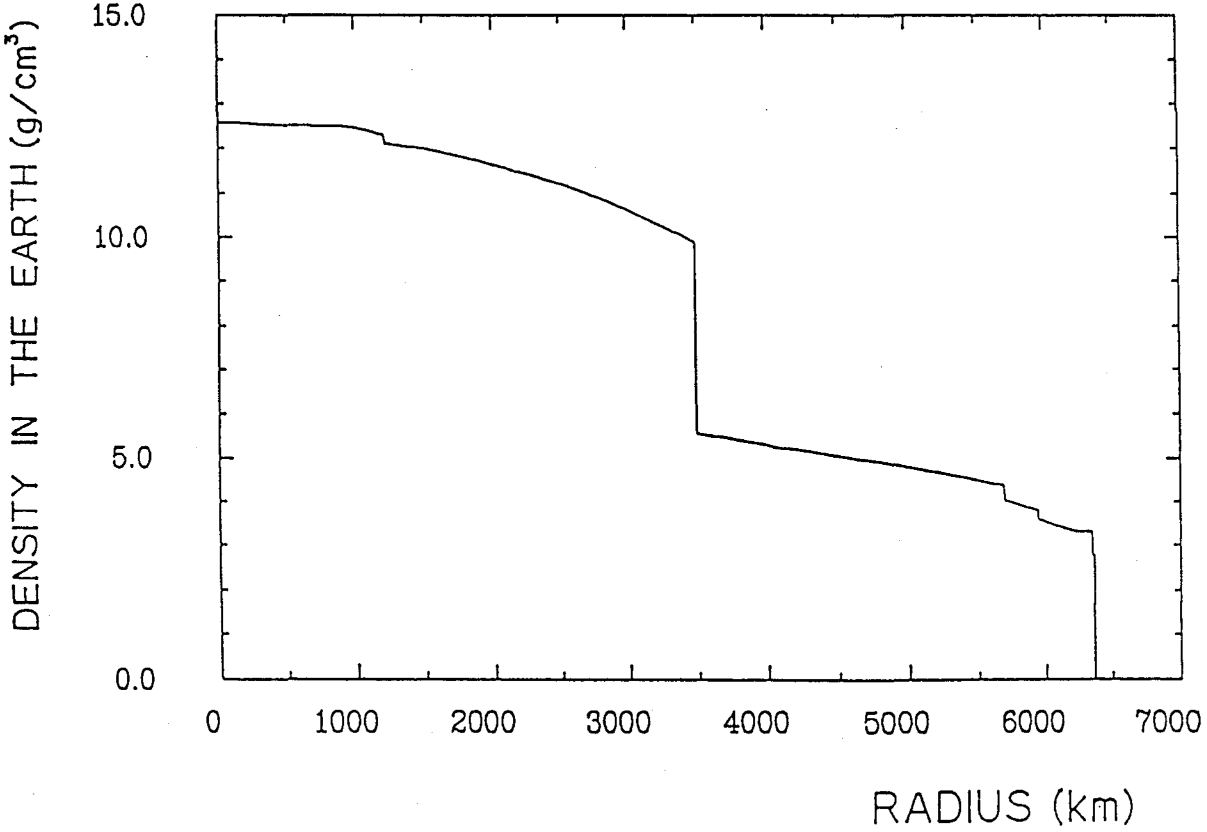
DENSITY IN THE EARTH (g/cm³)
15.0
10.0
5.0
0.0
0
1000
2000
3000
4000
5000
6000
7000
RADIUS (km)

Fig. 1.13

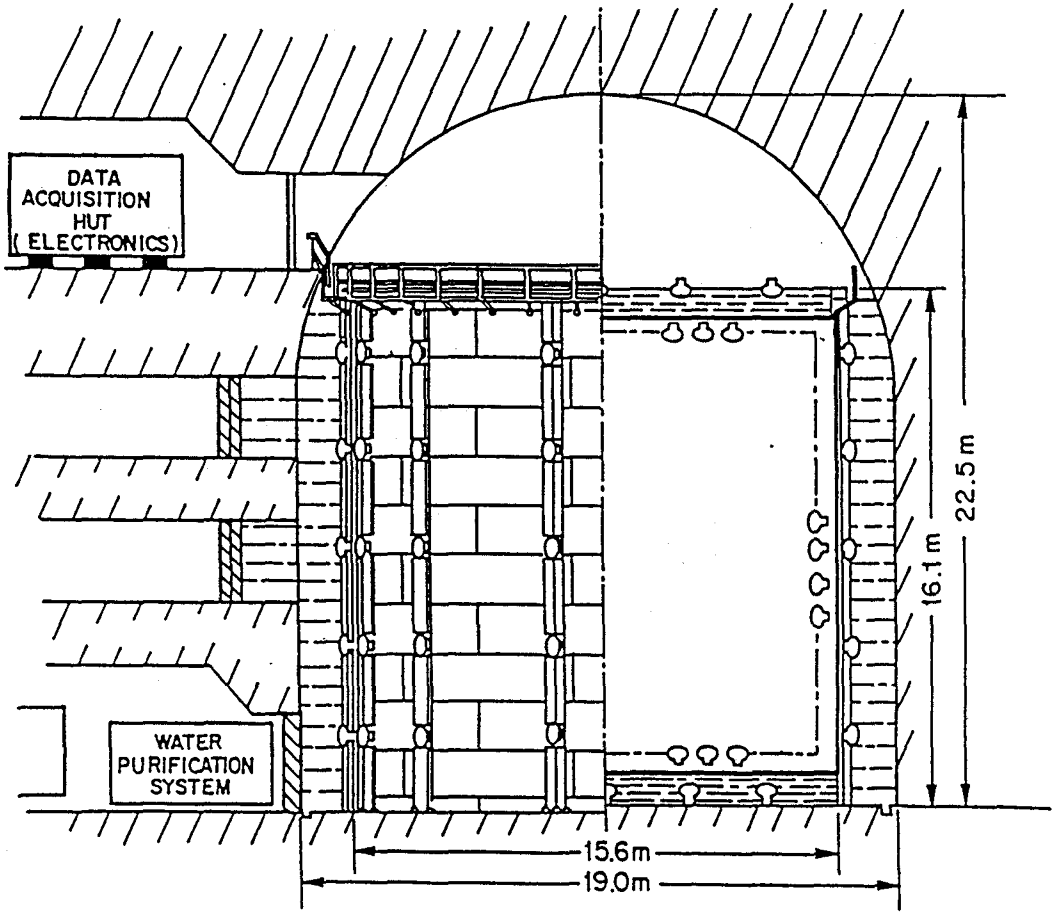
DATA ACQUISITION HUT (ELECTRONICS)
WATER PURIFICATION SYSTEM
22.5 m
16.1 m
15.6m
19.0m

Fig. 2.1

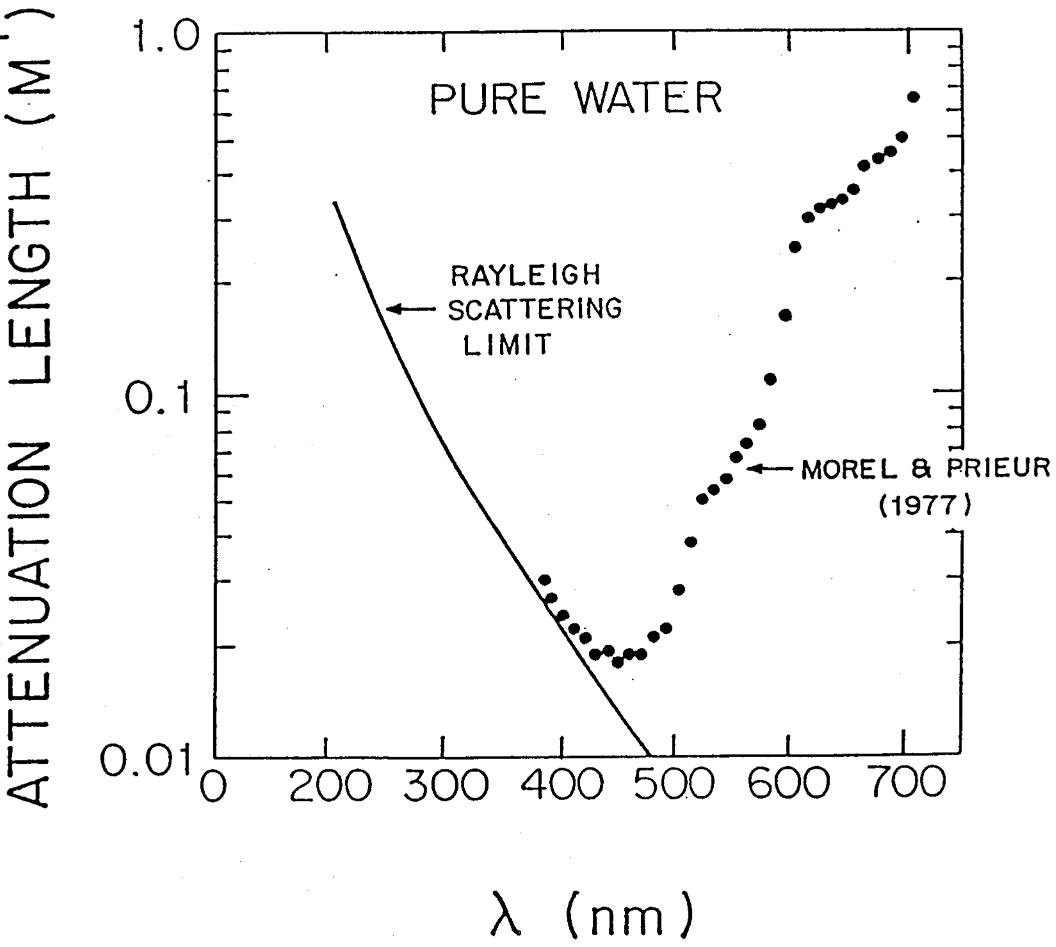

PURE WATER
RAYLEIGH SCATTERING LIMIT
MOREL & PRIEUR (1977)
ATTENUATION LENGTH (M^{-1})
1.0
0.1
0.01
0
200
300
400
500
600
700
λ (nm)

Fig. 2.2

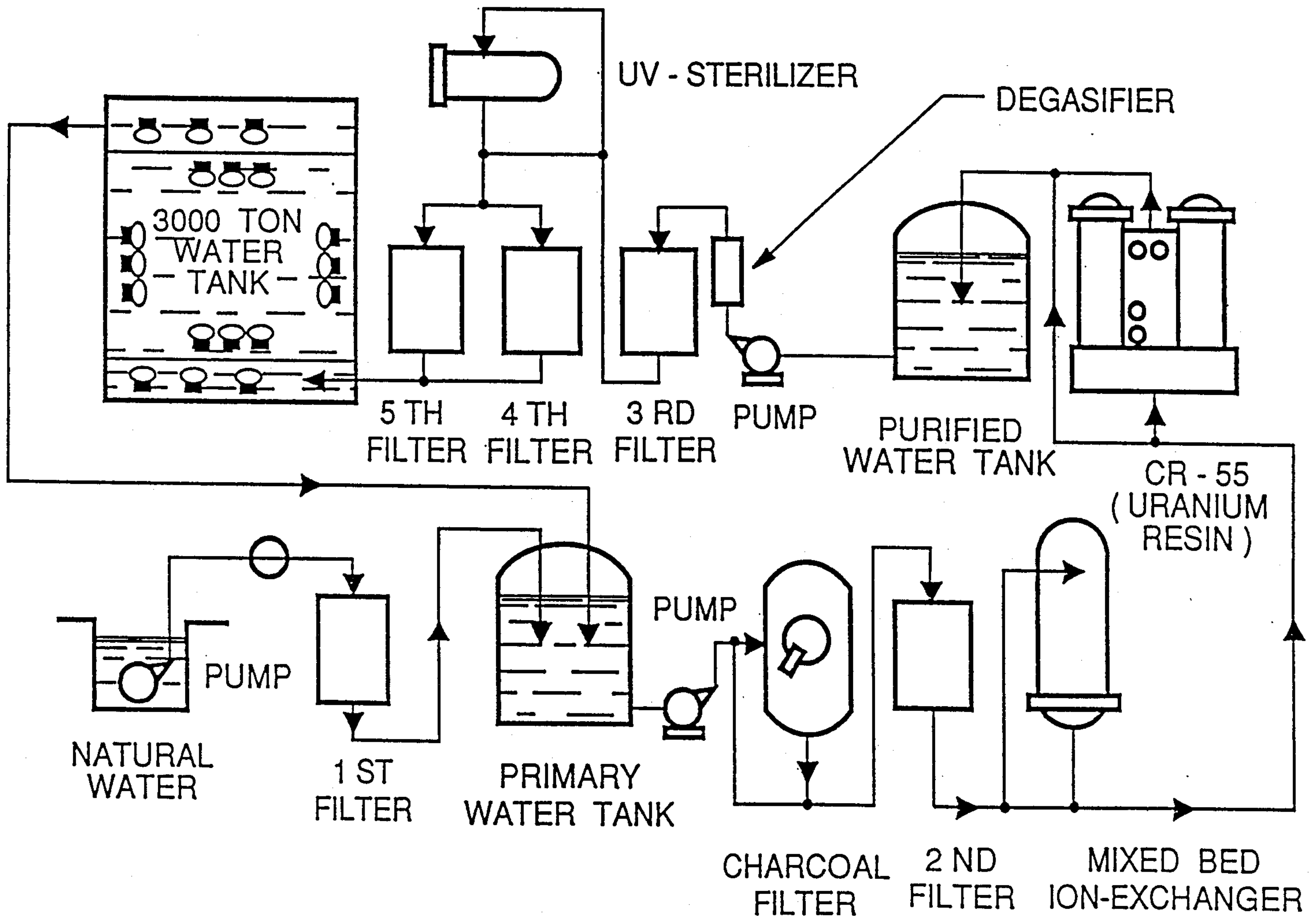
UV - STERILIZER
DEGASIFIER
3000 TON WATER TANK
5 TH FILTER
4 TH FILTER
3 RD FILTER
PUMP
PURIFIED WATER TANK
CR - 55 (URANIUM RESIN)
NATURAL WATER
PUMP
1 ST FILTER
PRIMARY WATER TANK
PUMP
CHARCOAL FILTER
2 ND FILTER
MIXED BED ION-EXCHANGER

Fig. 2.3

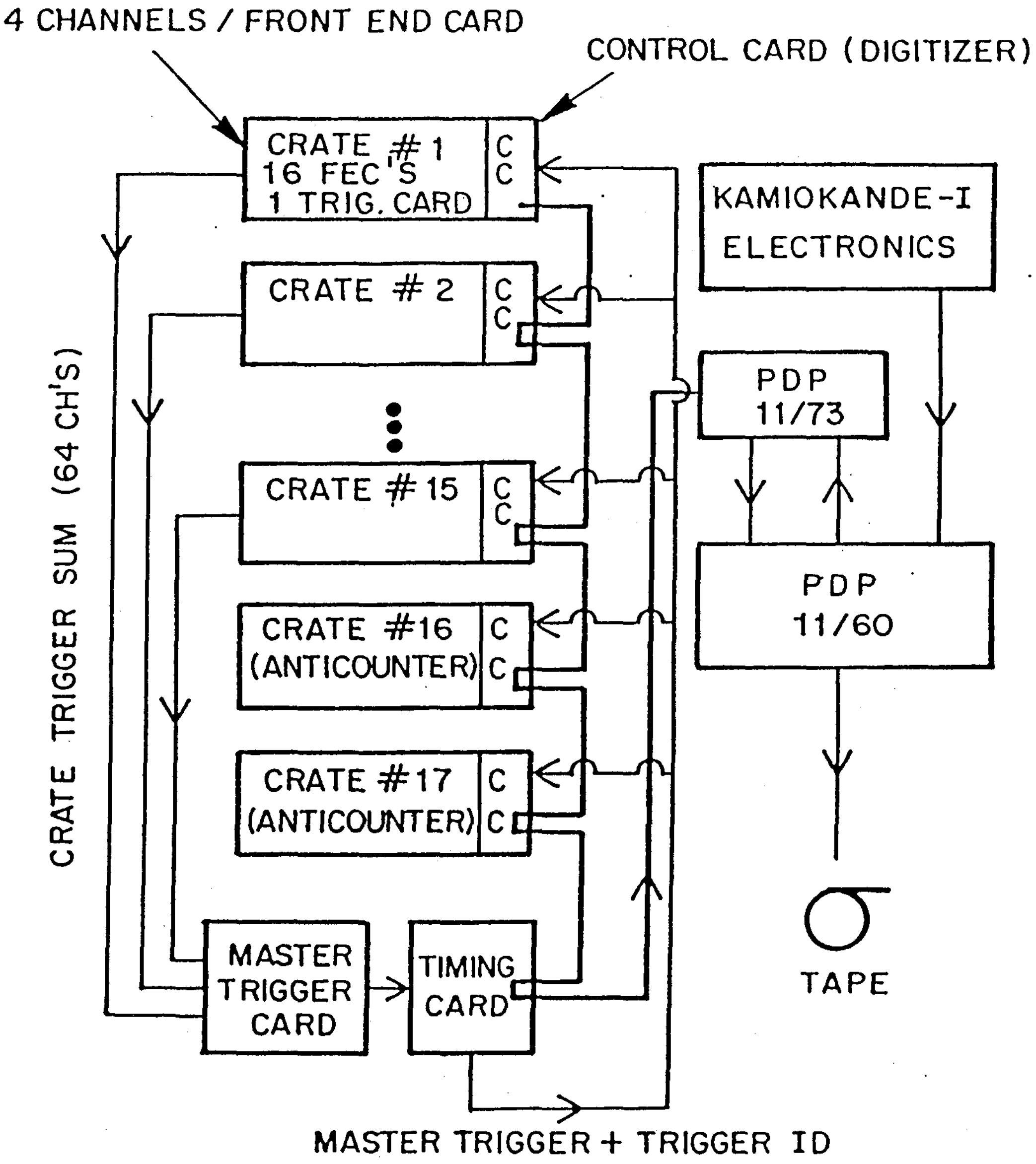
4 CHANNELS / FRONT END CARD
CONTROL CARD (DIGITIZER)
CRATE #1
16 FEC'S
1 TRIG. CARD
C C
CRATE #2
C C
CRATE #15
C C
CRATE #16
(ANTICOUNTER)
C C
CRATE #17
(ANTICOUNTER)
C C
KAMIOKANDE-I
ELECTRONICS
PDP
11/73
PDP
11/60
TAPE
CRATE TRIGGER SUM (64 CH'S)
MASTER
TRIGGER
CARD
TIMING
CARD
MASTER TRIGGER + TRIGGER ID

Fig. 2.4

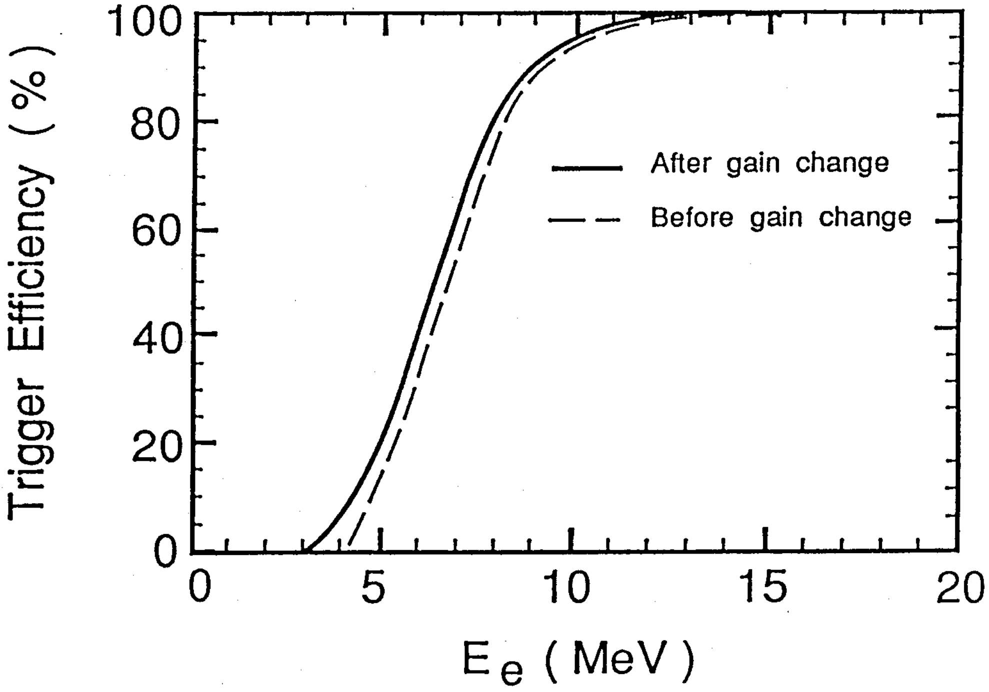
Trigger Efficiency (%)
100
80
60
40
20
0
0
5
10
15
20
E$_e$ (MeV)
After gain change
Before gain change

Fig. 2.5

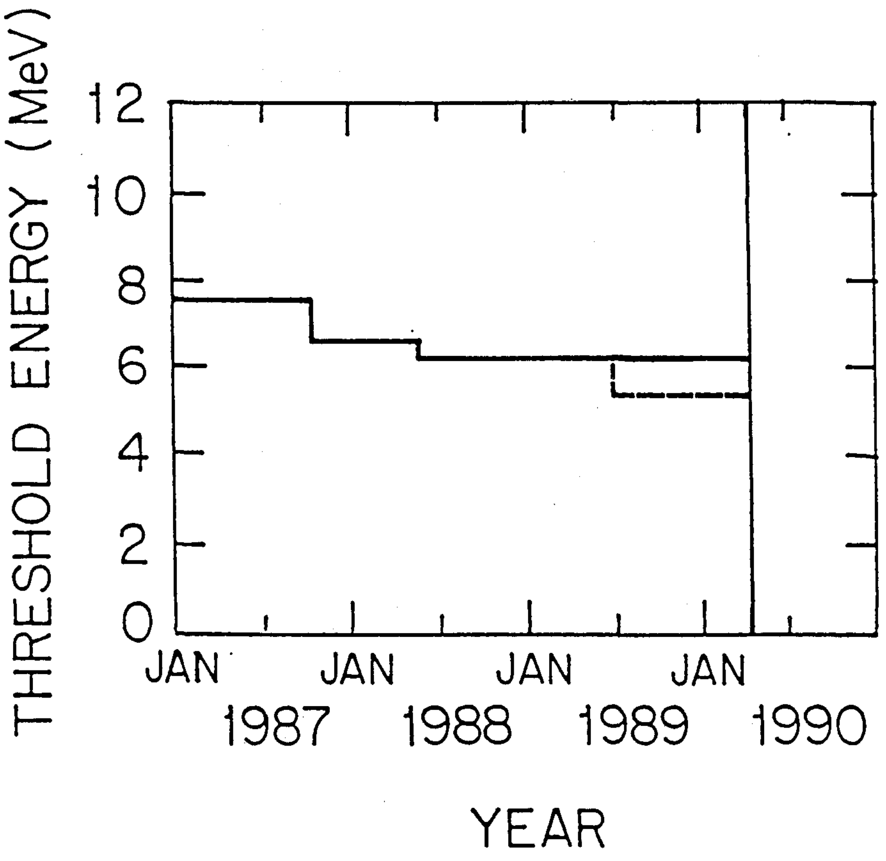
THRESHOLD ENERGY (MeV)
12
10
8
6
4
2
0
JAN
1987
JAN
1988
JAN
1989
JAN
1990
YEAR

Fig. 2.6

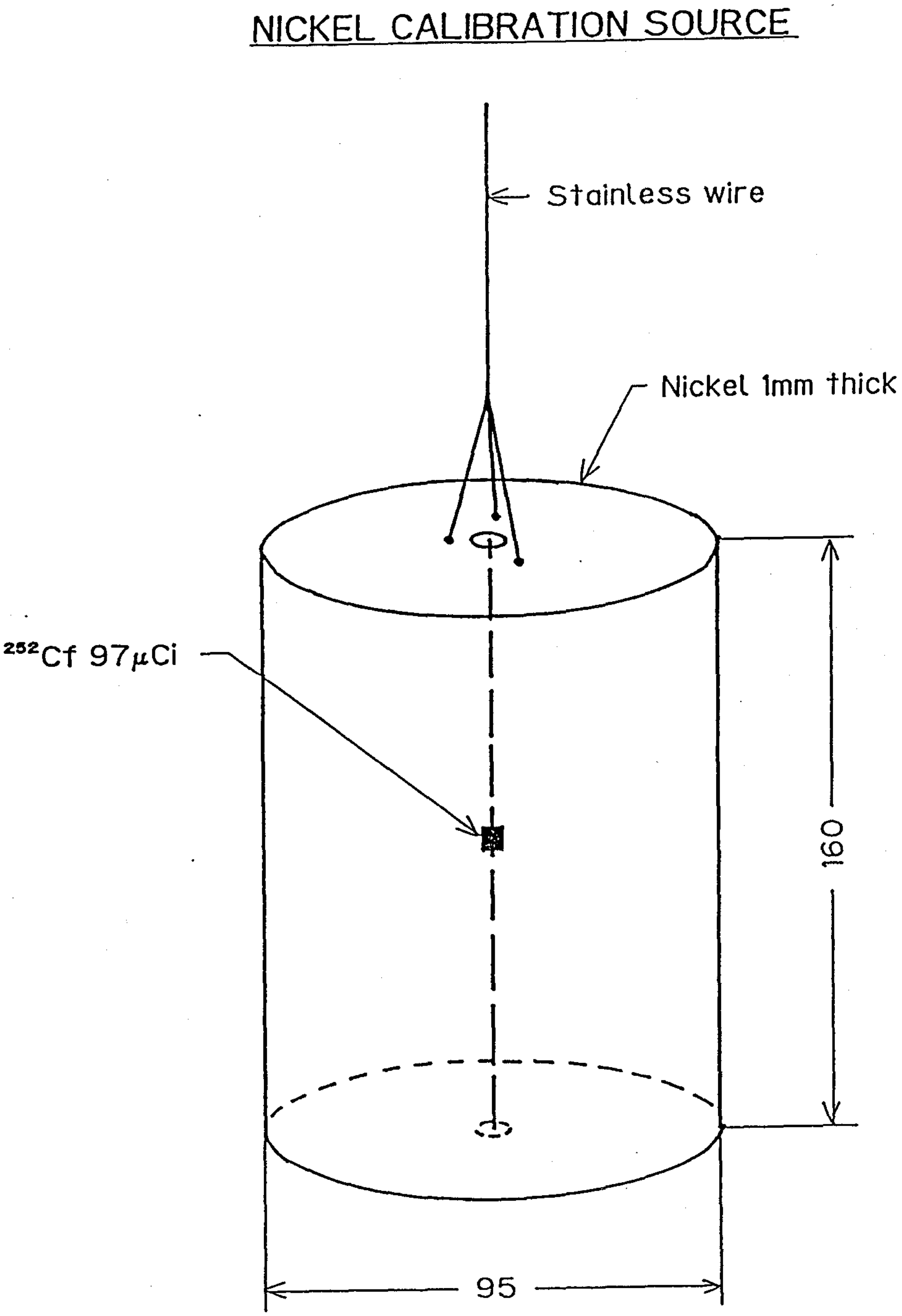
NICKEL CALIBRATION SOURCE
Stainless wire
Nickel 1mm thick
^{252}Cf 97μCi
160
95

Fig. 2.7

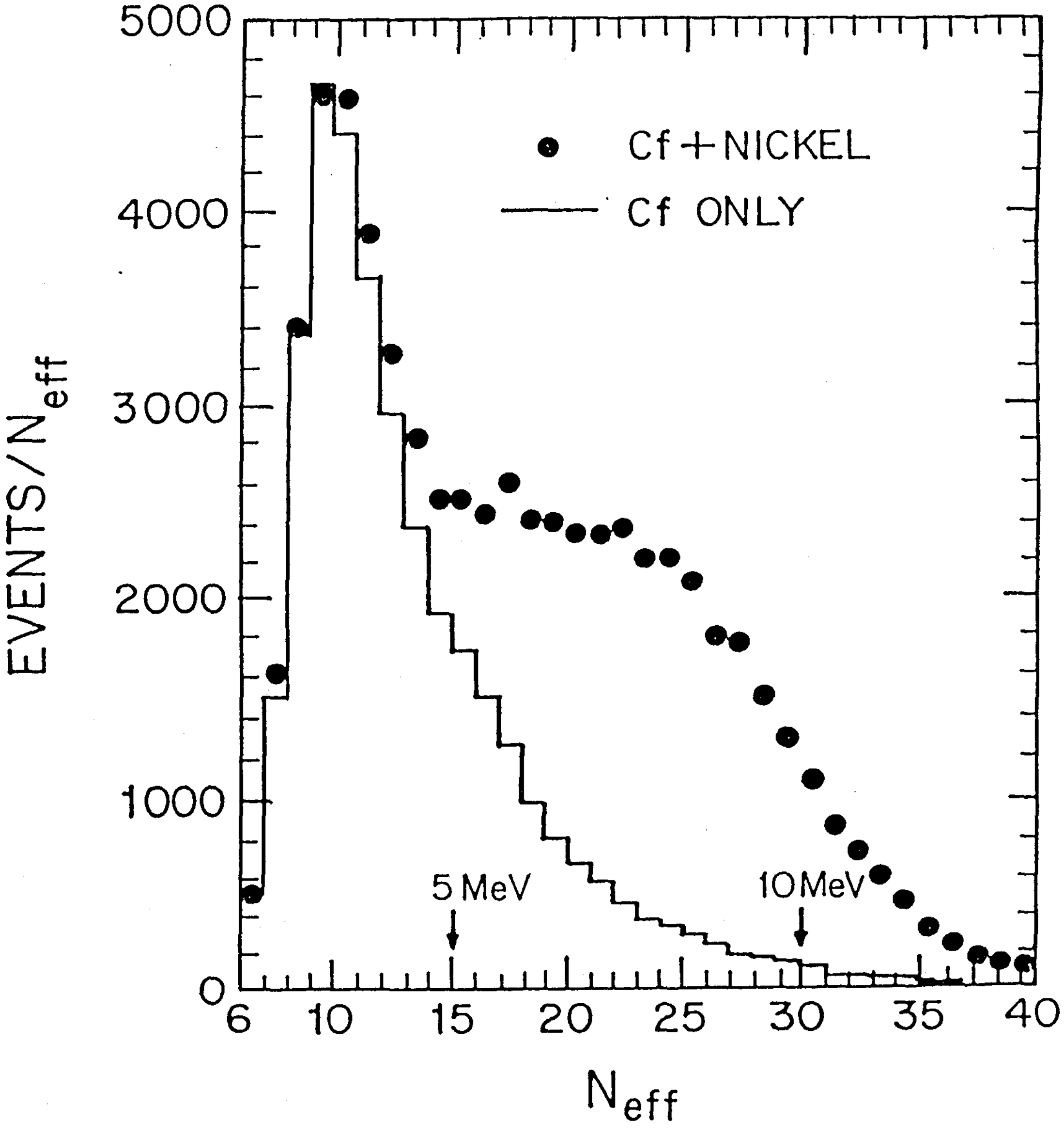
EVENTS/N_{eff}
5000
4000
3000
2000
1000
0
6
10
15
20
25
30
35
40
N_{eff}
● Cf + NICKEL
Cf ONLY
5 MeV
10 MeV

Fig. 2.8

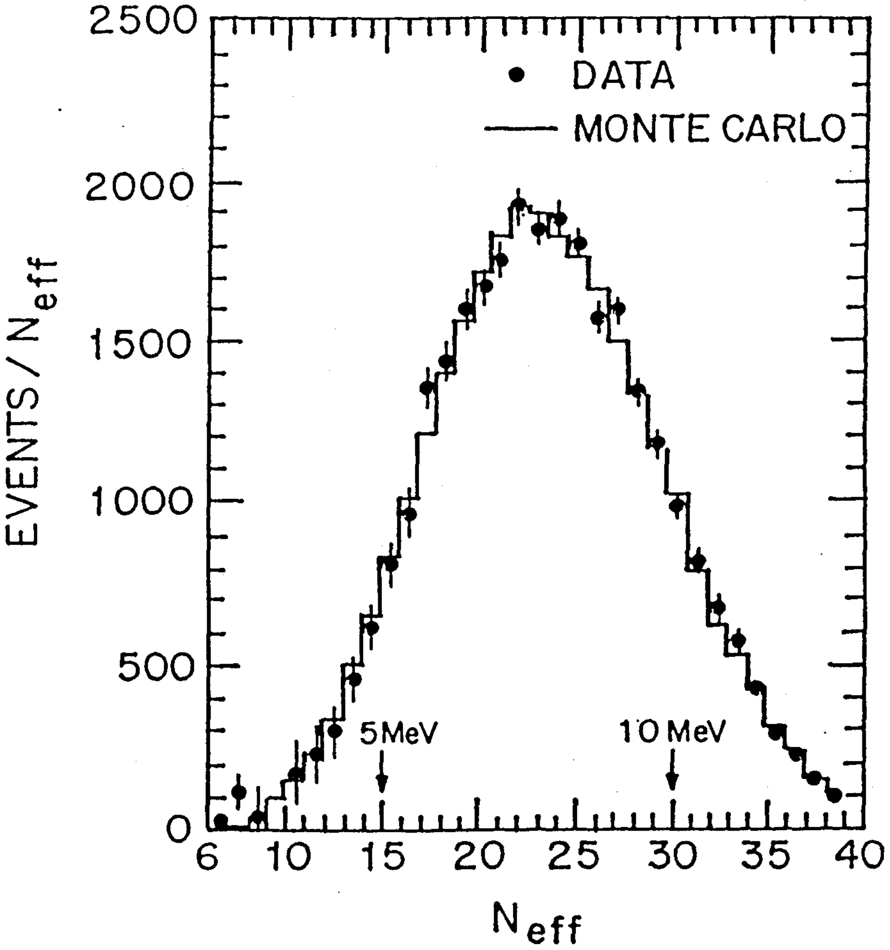
● DATA
—— MONTE CARLO
5MeV
10 MeV
EVENTS / N_{eff}
N_{eff}
0
500
1000
1500
2000
2500
6
10
15
20
25
30
35
40

Fig. 2.9

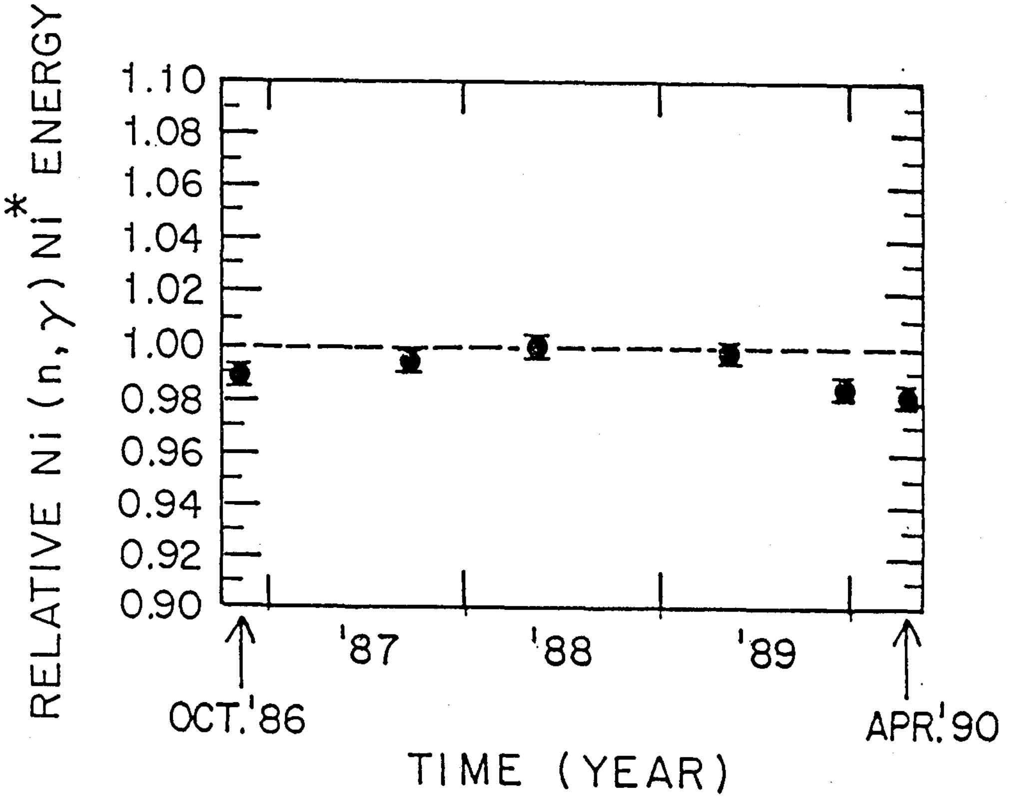
RELATIVE Ni (n, γ) Ni* ENERGY
1.10
1.08
1.06
1.04
1.02
1.00
0.98
0.96
0.94
0.92
0.90
OCT.'86
'87
'88
'89
APR.'90
TIME (YEAR)

Fig. 2.10

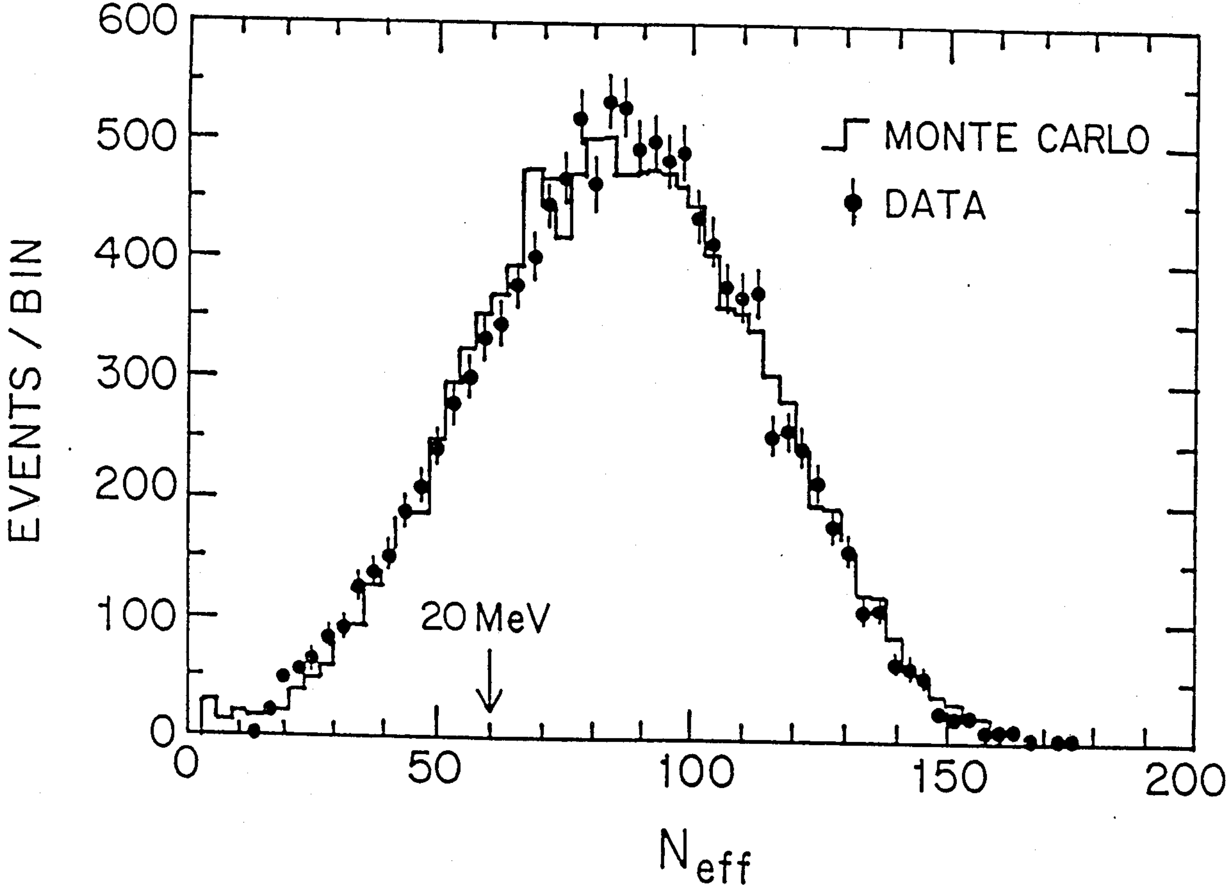
EVENTS / BIN
600
500
400
300
200
100
0
0
50
100
150
200
N_{eff}
MONTE CARLO
DATA
20 MeV

Fig. 2.11

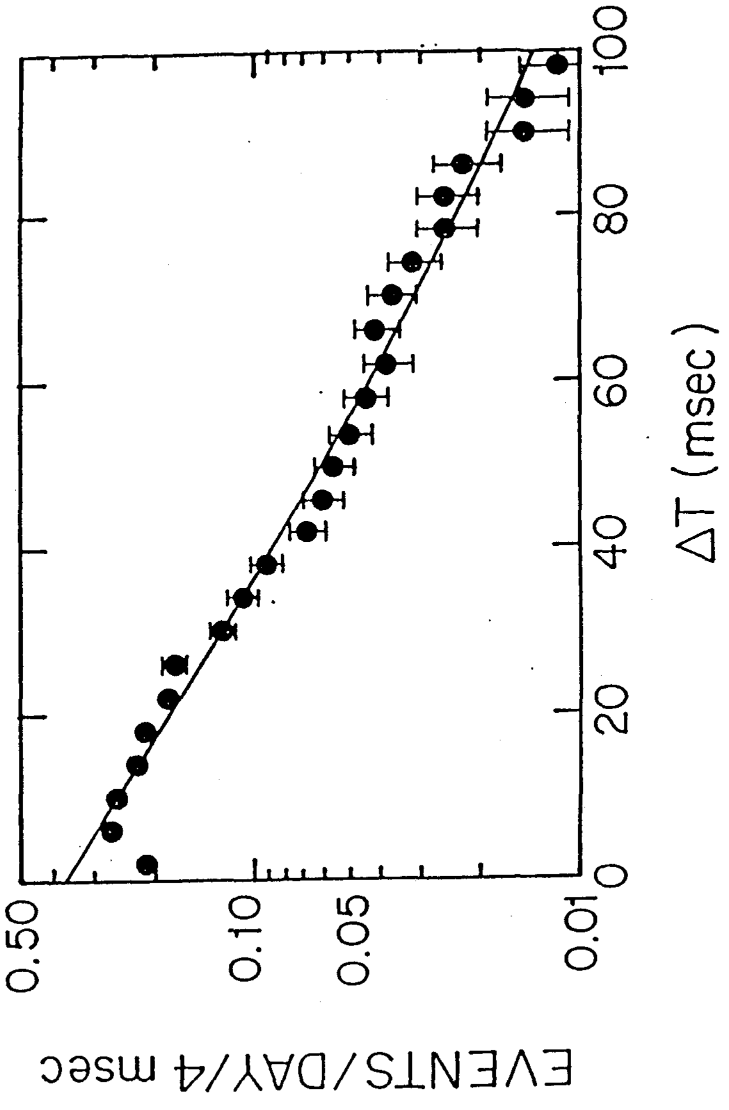

Fig. 2.12

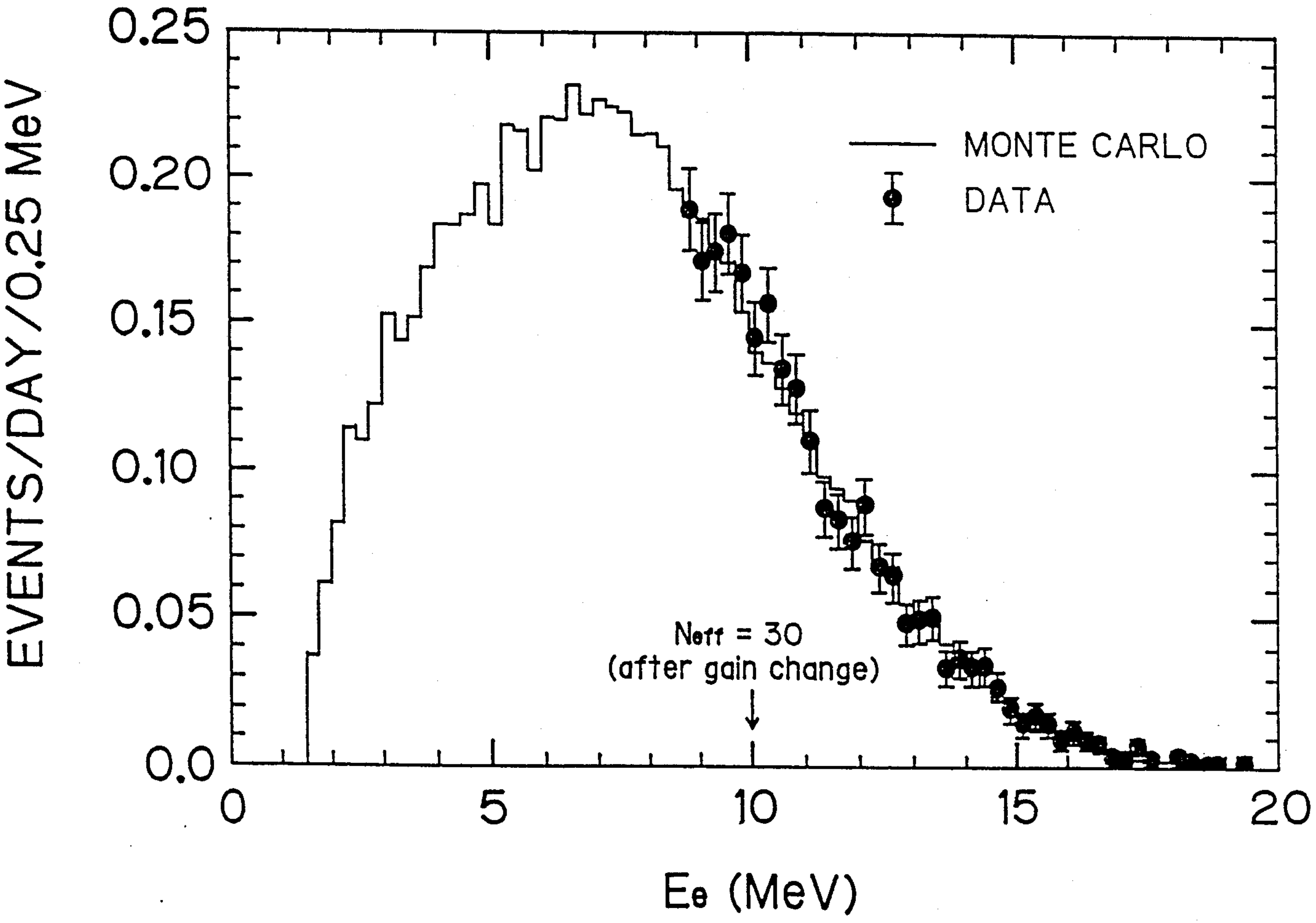
0.25
0.20
0.15
0.10
0.05
0.0
EVENTS/DAY/0.25 MeV
0
5
10
15
20
Ee (MeV)
MONTE CARLO
DATA
Neff = 30
(after gain change)

Fig. 2.13

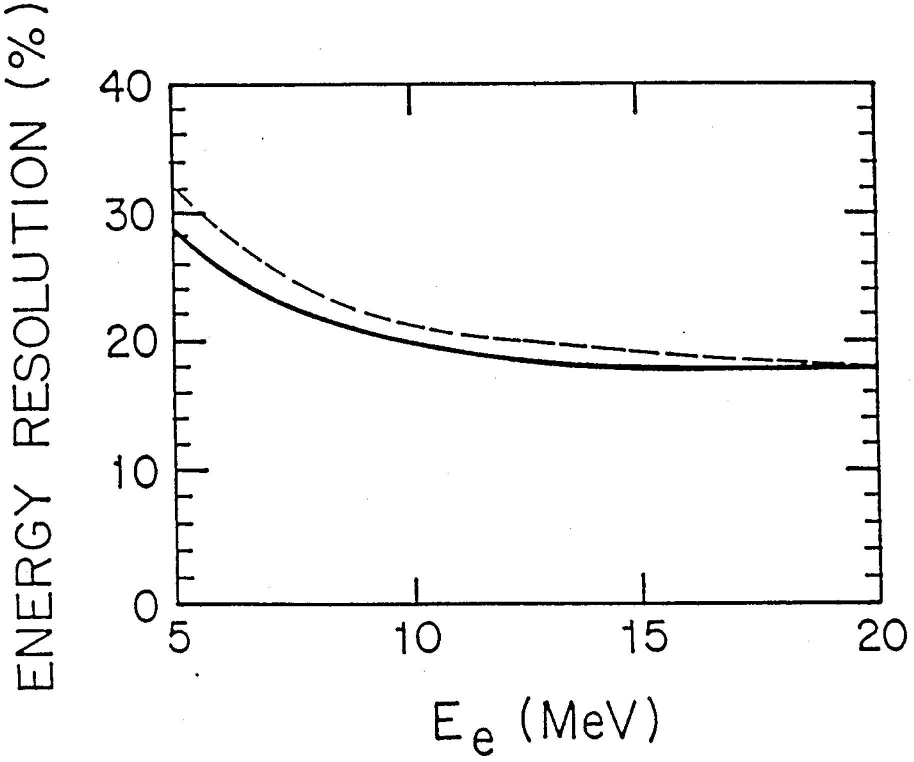

Fig. 2.14

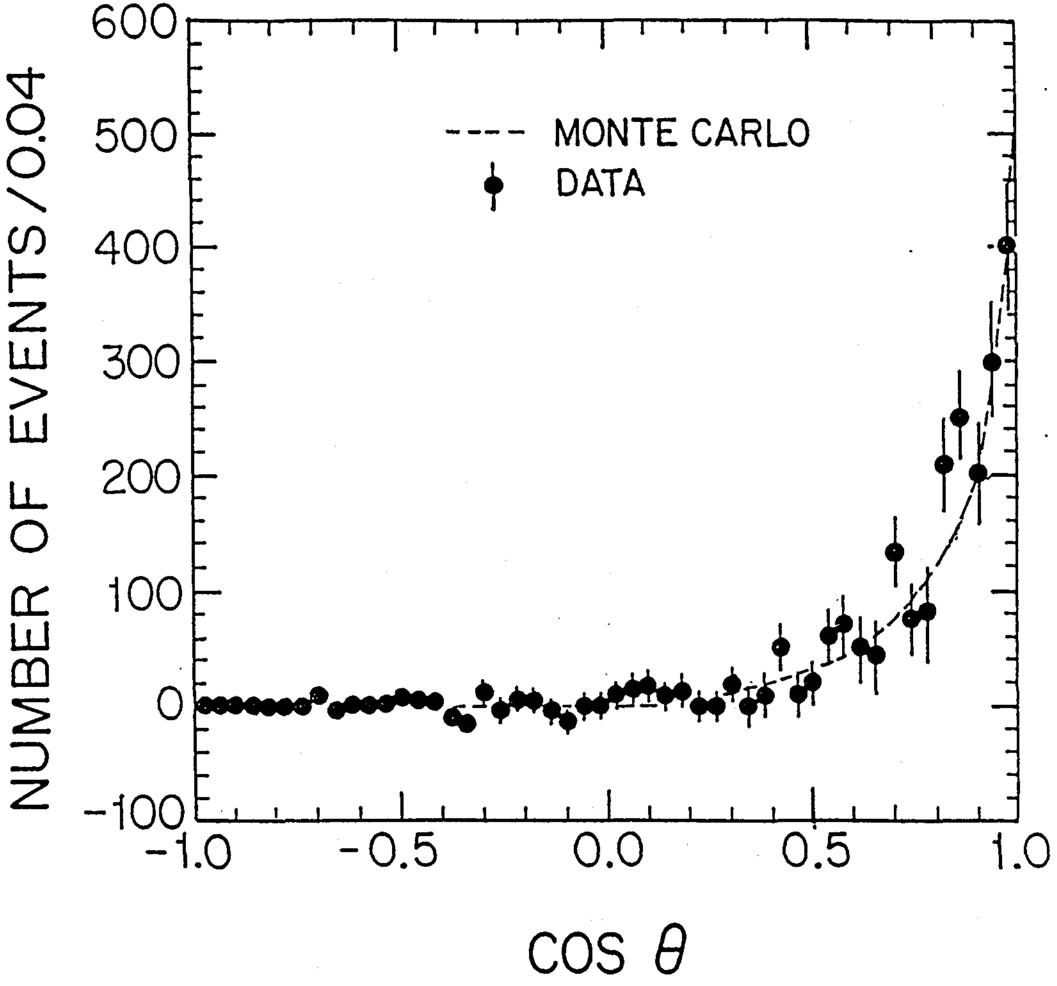
MONTE CARLO
DATA
NUMBER OF EVENTS/0.04
600
500
400
300
200
100
0
−100
−1.0
−0.5
0.0
0.5
1.0
COS θ

Fig. 2.15

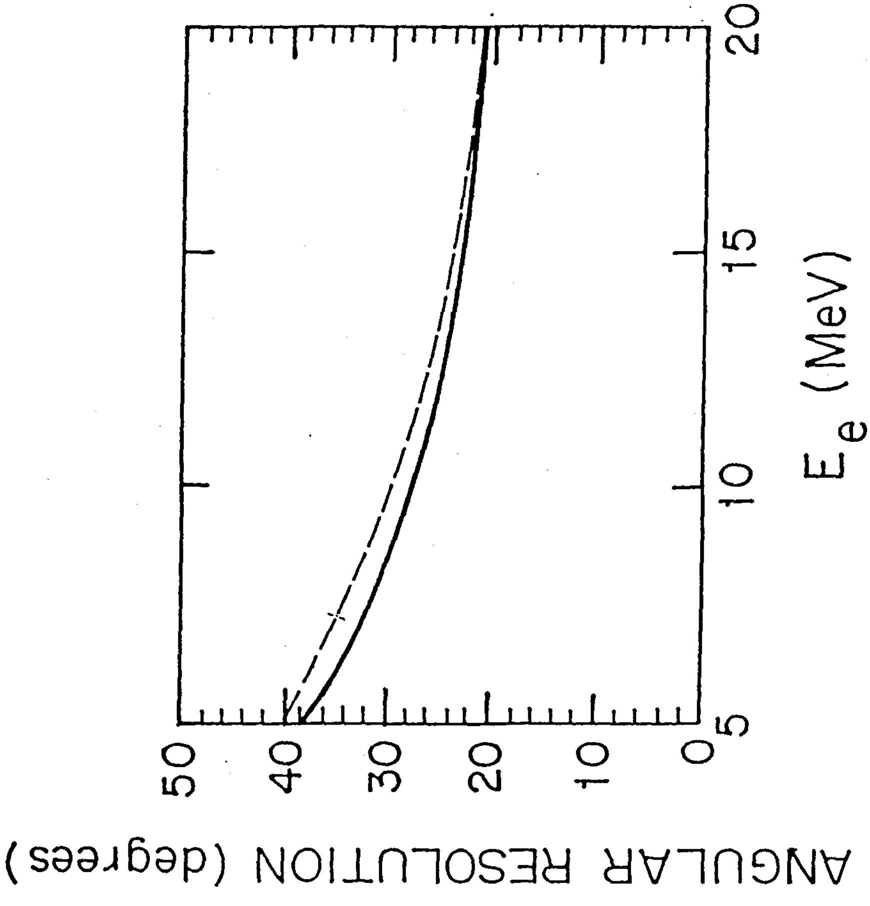

Fig. 2.16

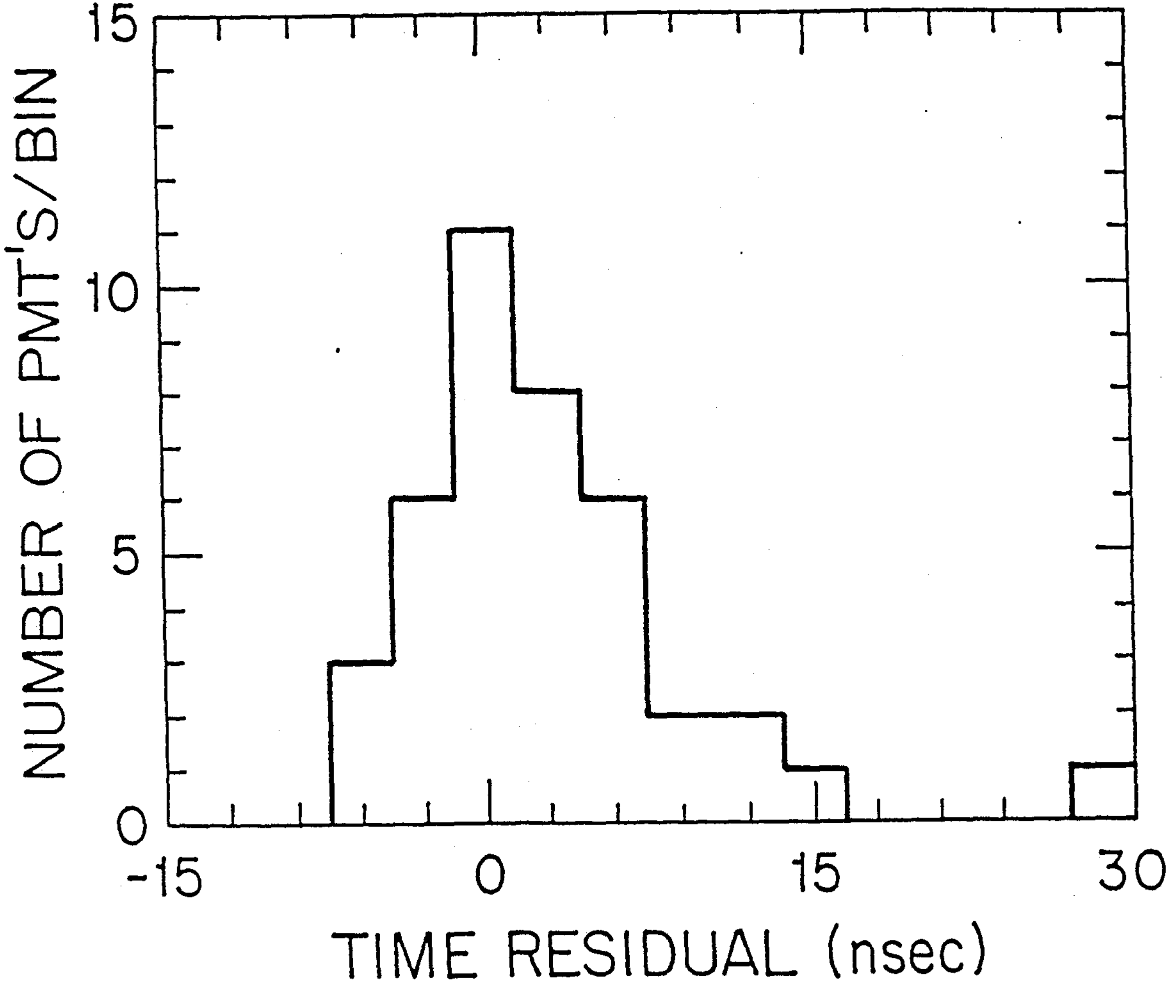

Fig. 2.17(a)

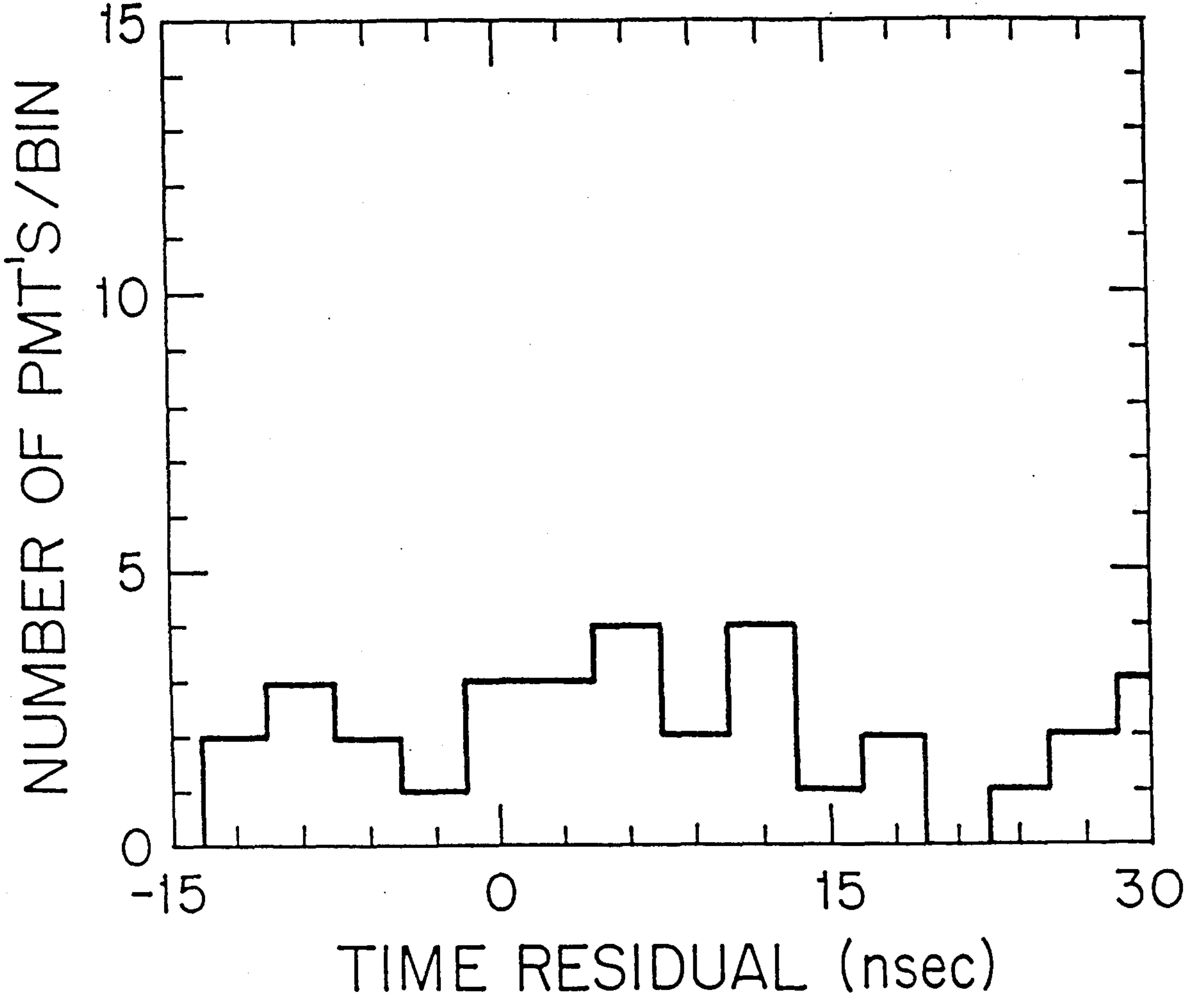

Fig. 2.17(b)

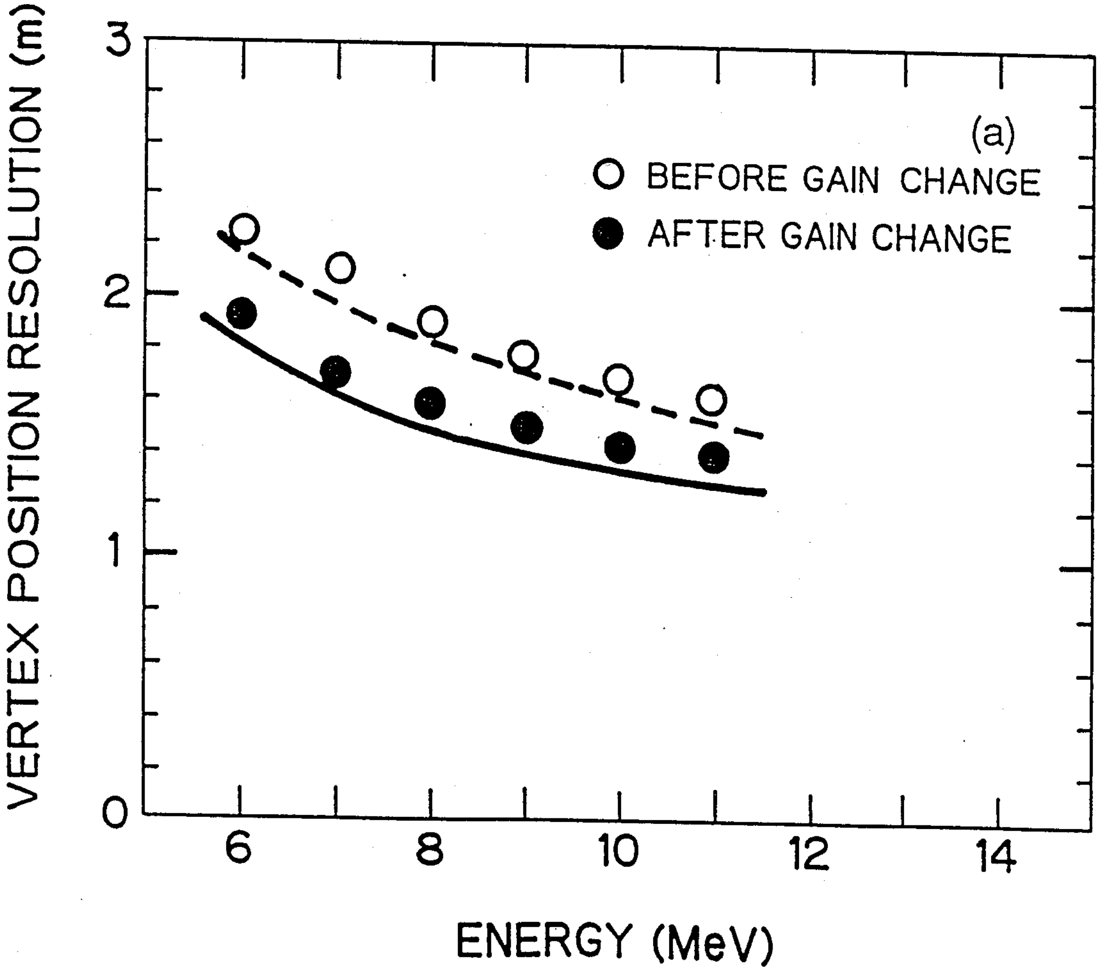
VERTEX POSITION RESOLUTION (m)
0
1
2
3
ENERGY (MeV)
6
8
10
12
14
(a)
○ BEFORE GAIN CHANGE
● AFTER GAIN CHANGE

Fig. 2.18

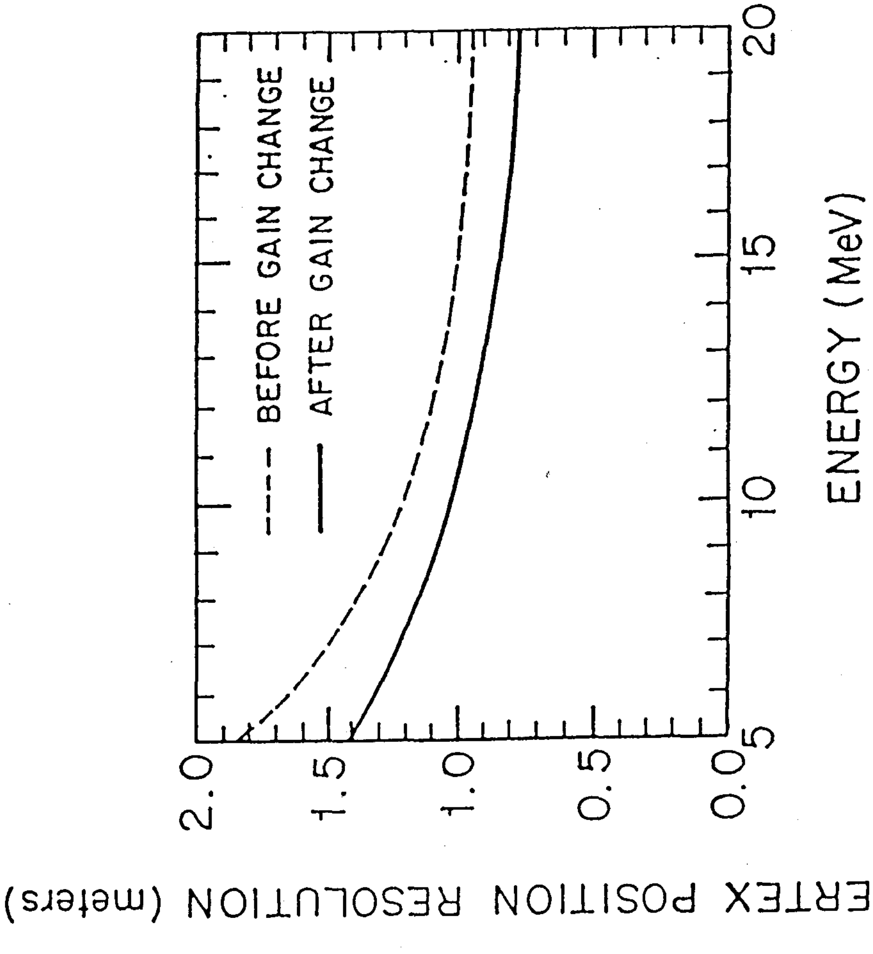
VERTEX POSITION RESOLUTION (meters)
2.0
1.5
1.0
0.5
0.0
5
10
15
20
ENERGY (MeV)
BEFORE GAIN CHANGE
AFTER GAIN CHANGE

Fig. 2.19

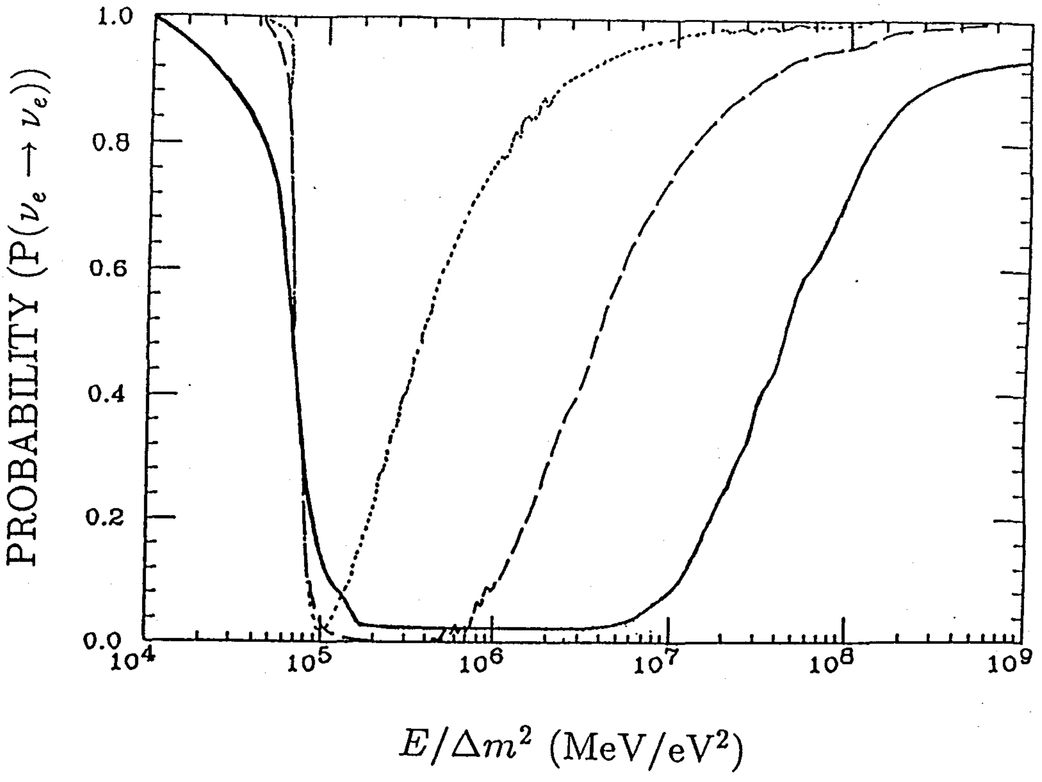
1.0
0.8
0.6
0.4
0.2
0.0
10^4
10^5
10^6
10^7
10^8
10^9
PROBABILITY $(\mathrm{P}(\nu_e \to \nu_e))$
$E/\Delta m^2$ (MeV/eV^2)

Fig. 3.1

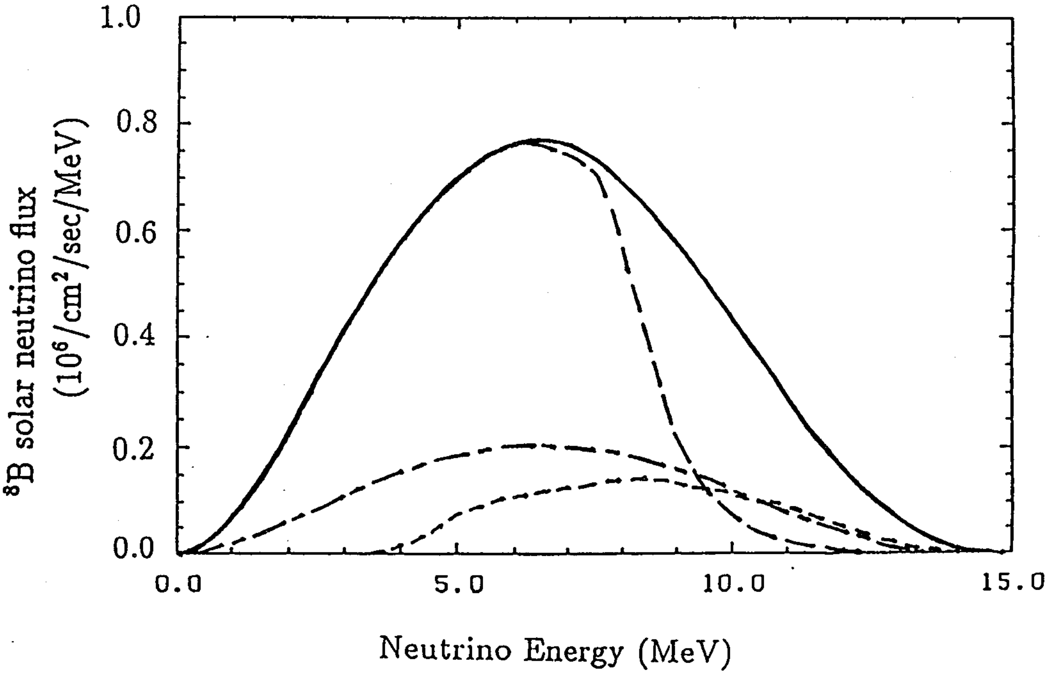
1.0
0.8
0.6
0.4
0.2
0.0
^{8}B solar neutrino flux
(10^6/cm^2/sec/MeV)
0.0
5.0
10.0
15.0
Neutrino Energy (MeV)

Fig. 3.2

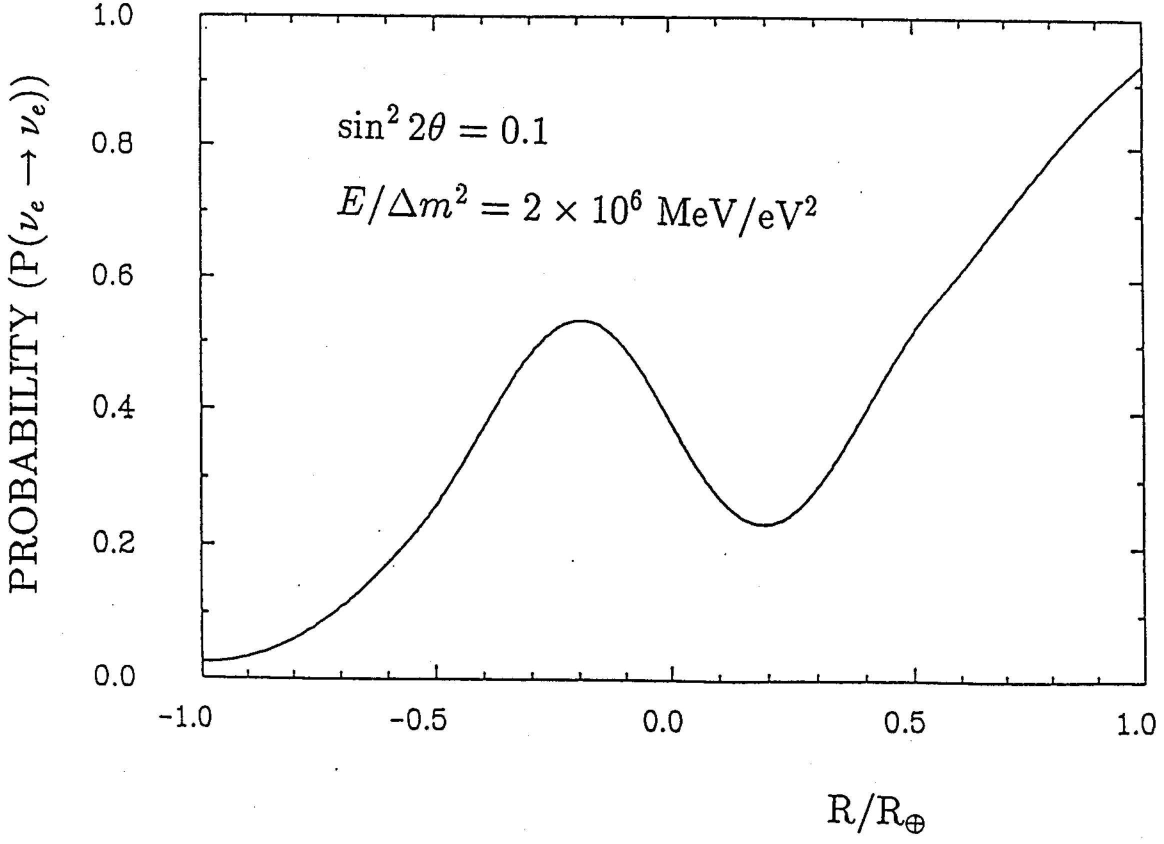
$\sin^2 2\theta = 0.1$
$E/\Delta m^2 = 2 \times 10^6$ MeV/eV^2
PROBABILITY (P($\nu_e \rightarrow \nu_e$))
1.0
0.8
0.6
0.4
0.2
0.0
-1.0
-0.5
0.0
0.5
1.0
R/R$_\oplus$

Fig. 3.3

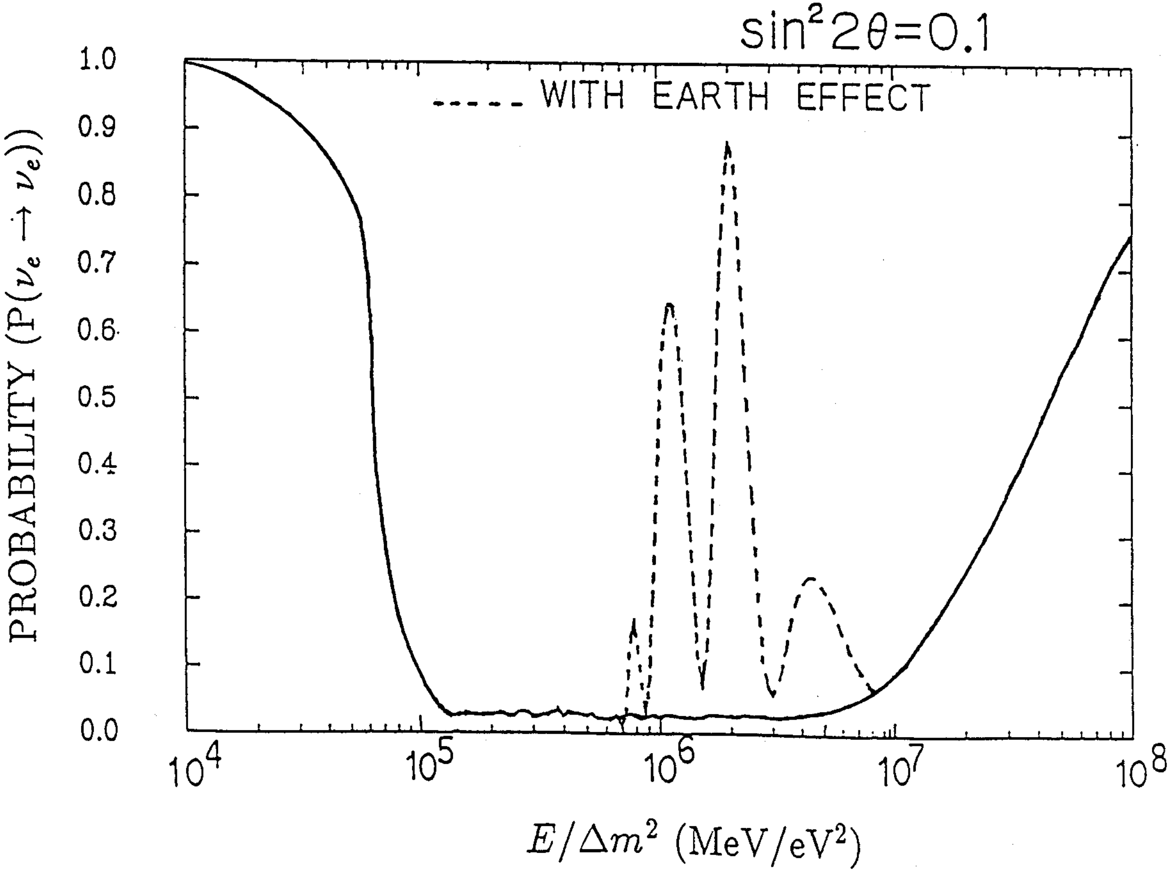
sin²2θ=0.1
----- WITH EARTH EFFECT
PROBABILITY (P($\nu_e \to \nu_e$))
1.0
0.9
0.8
0.7
0.6
0.5
0.4
0.3
0.2
0.1
0.0
10^4
10^5
10^6
10^7
10^8
$E/\Delta m^2$ (MeV/eV^2)

Fig. 3.4

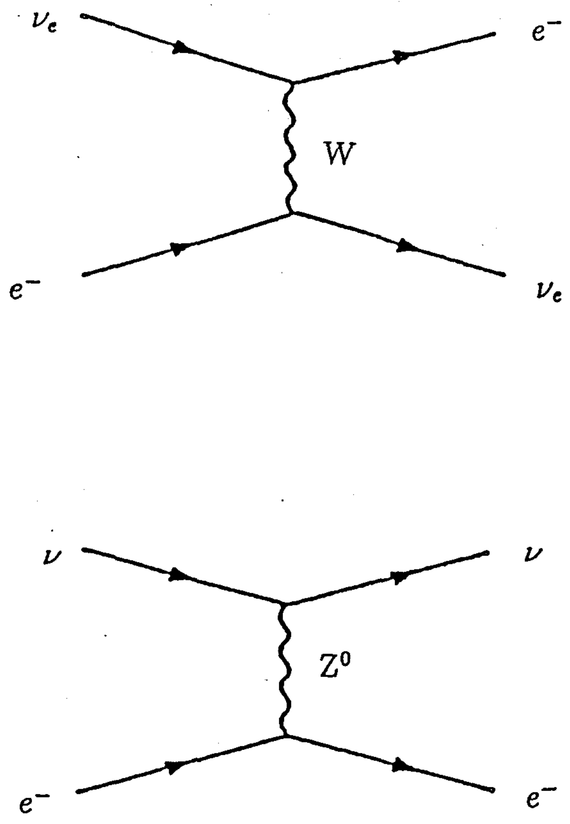

Fig. 3.5

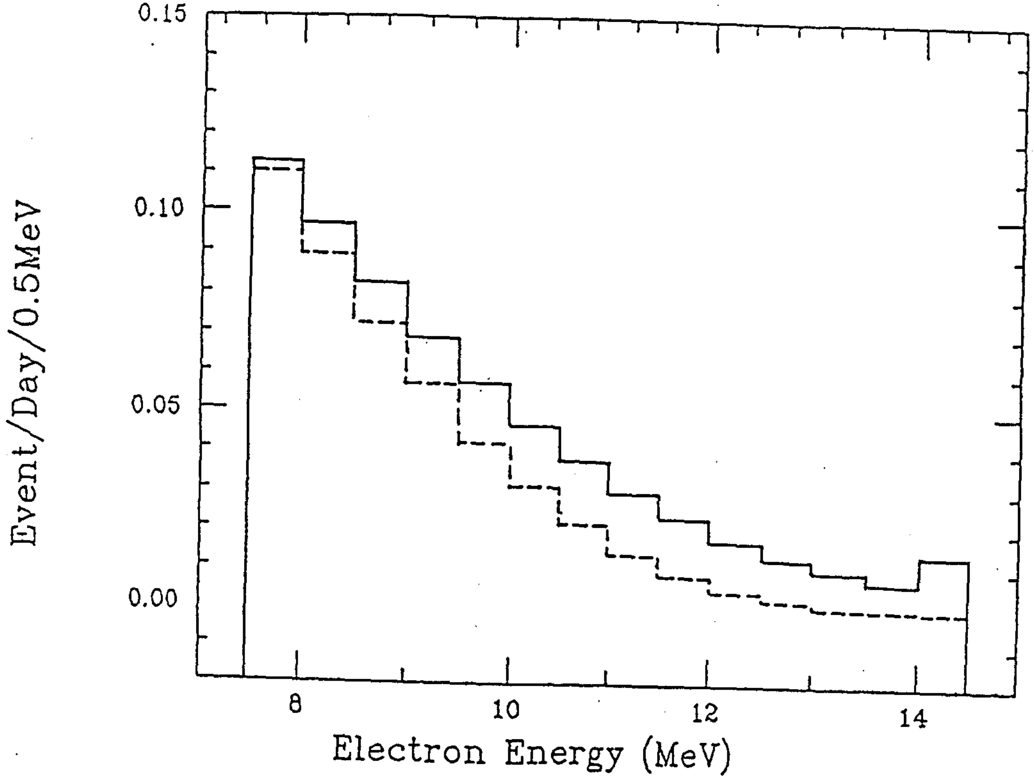

Fig. 3.6

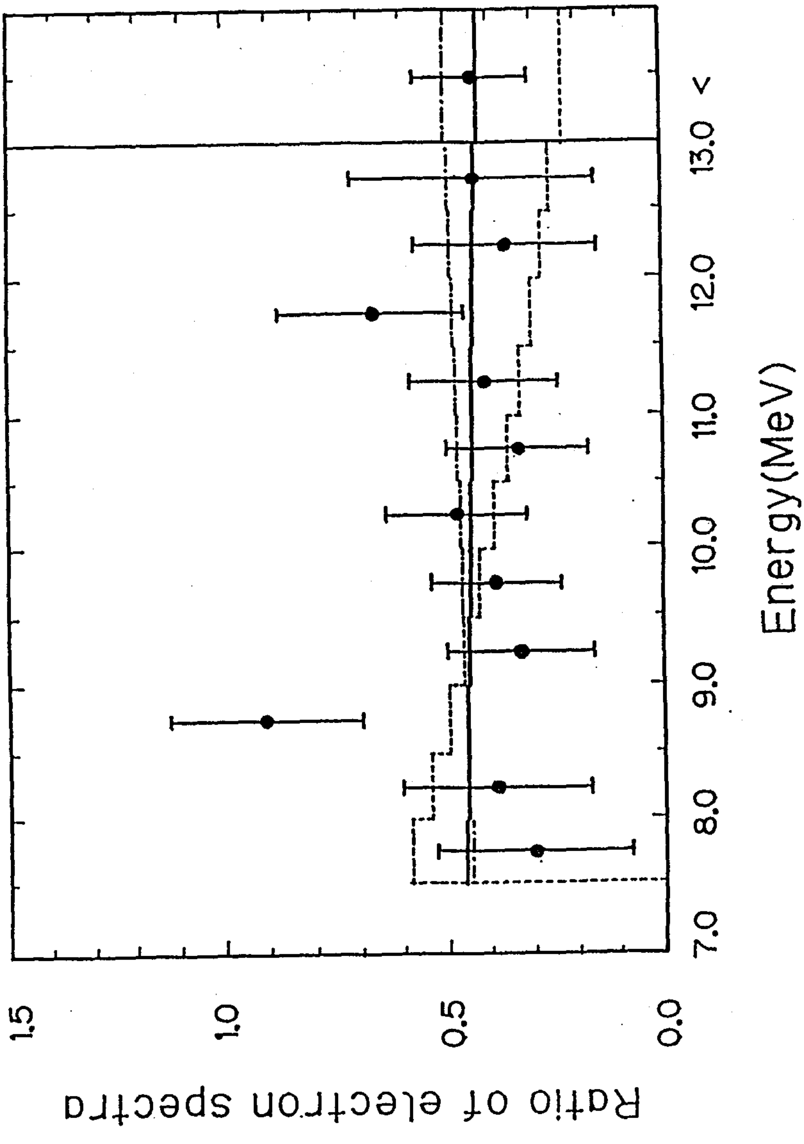
Ratio of electron spectra
0.0
0.5
1.0
1.5
Energy(MeV)
7.0
8.0
9.0
10.0
11.0
12.0
13.0
<

Fig. 3.7

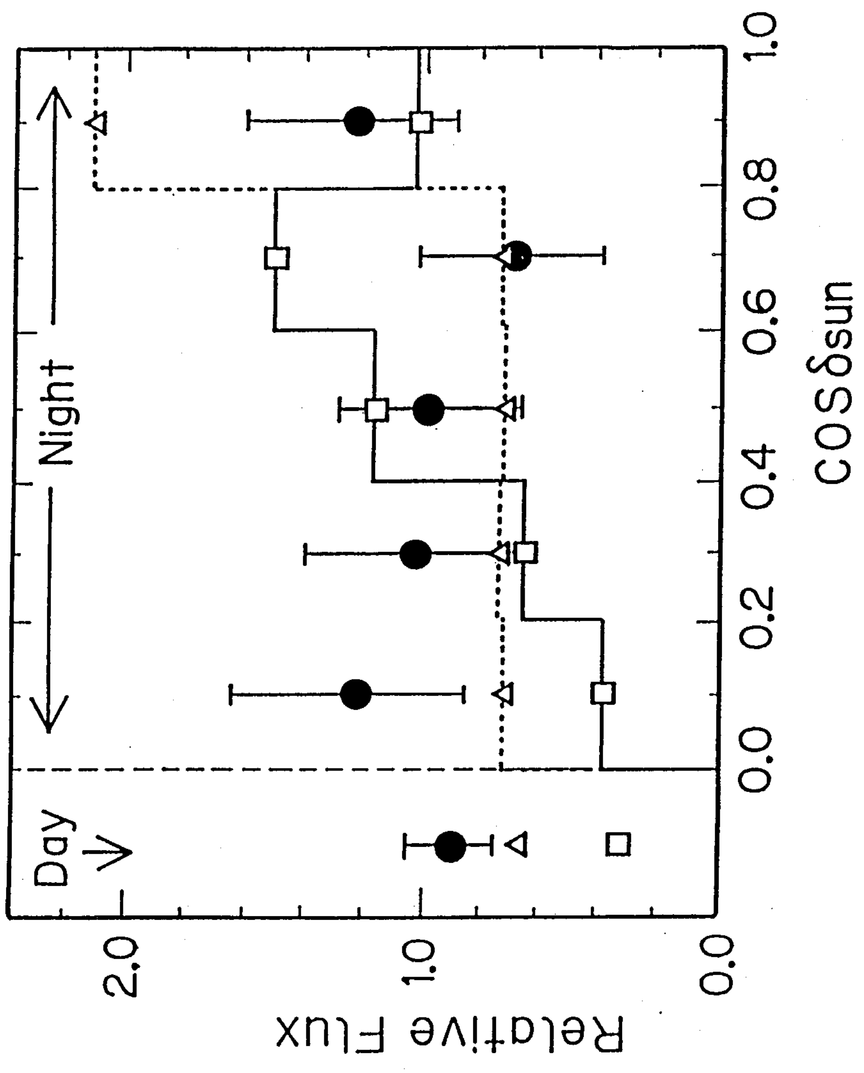

Fig. 3.8

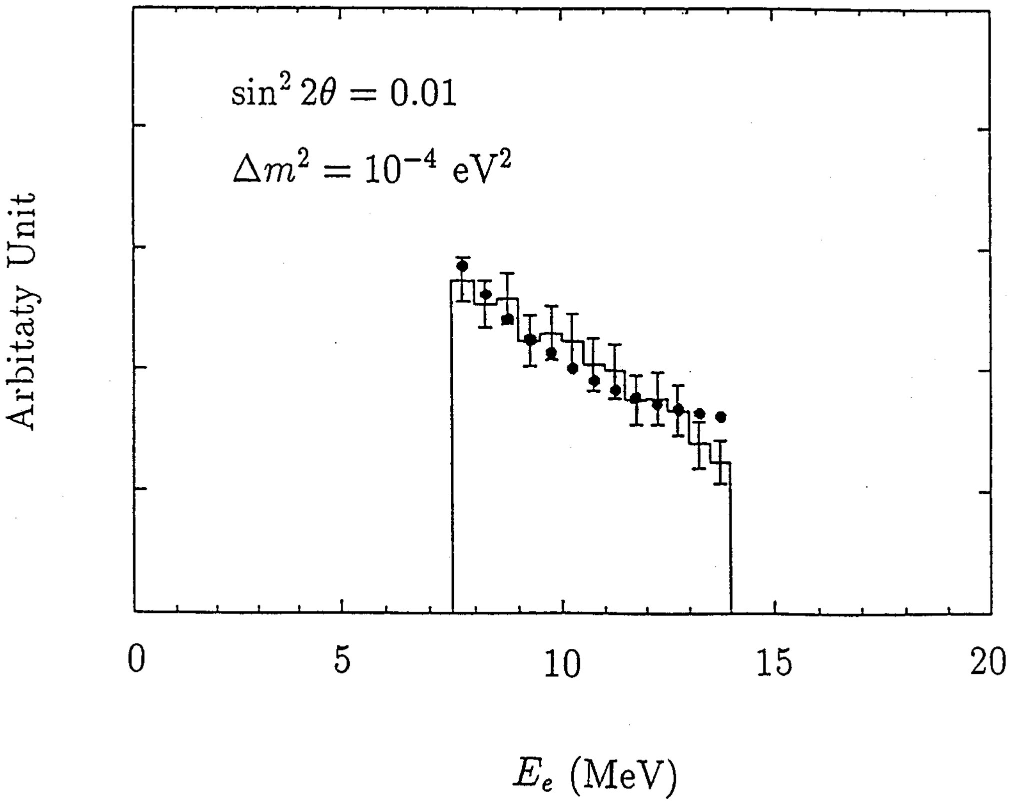
$\sin^2 2\theta = 0.01$
$\Delta m^2 = 10^{-4}$ eV^2
Arbitaty Unit
0
5
10
15
20
E_e (MeV)

Fig. 3.9

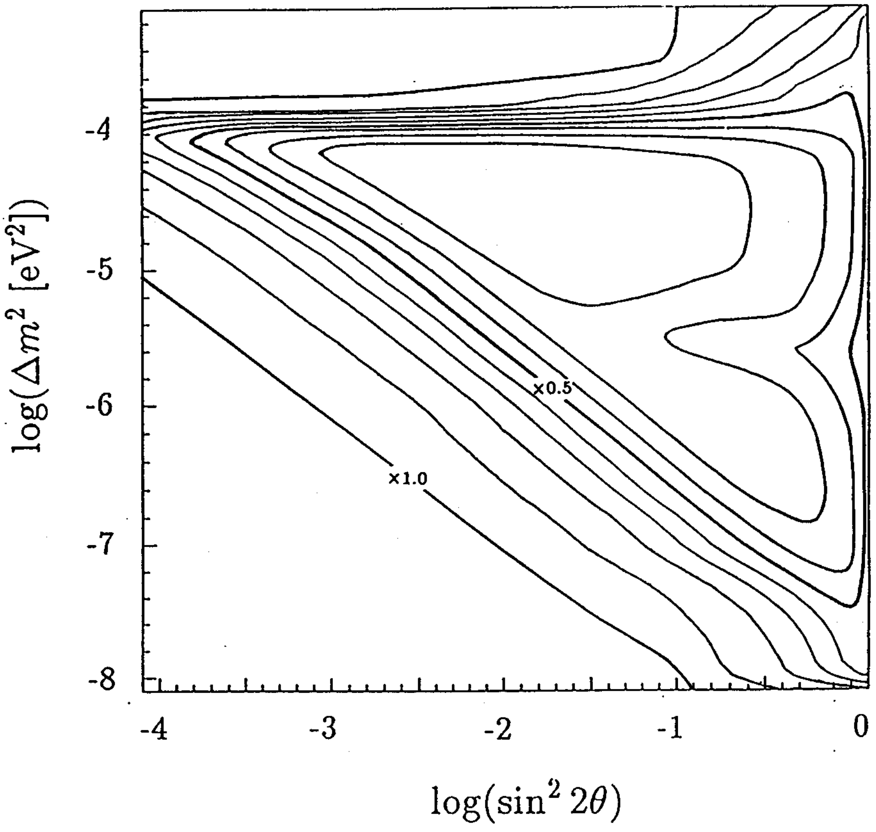

Fig. 3.10(a)

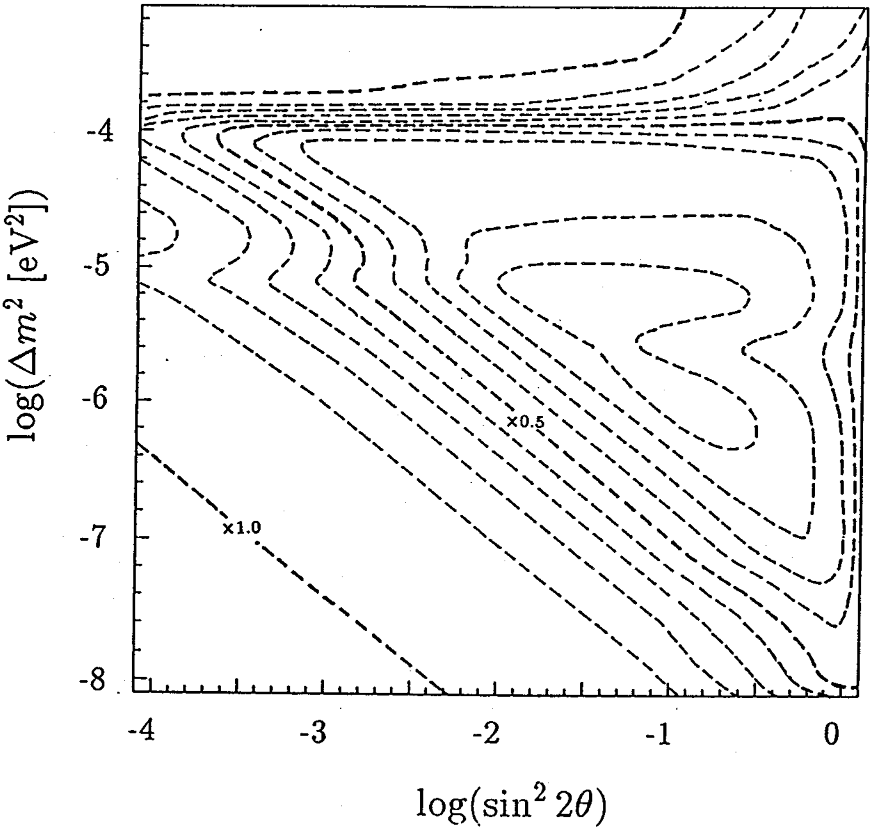

Fig. 3.10(b)

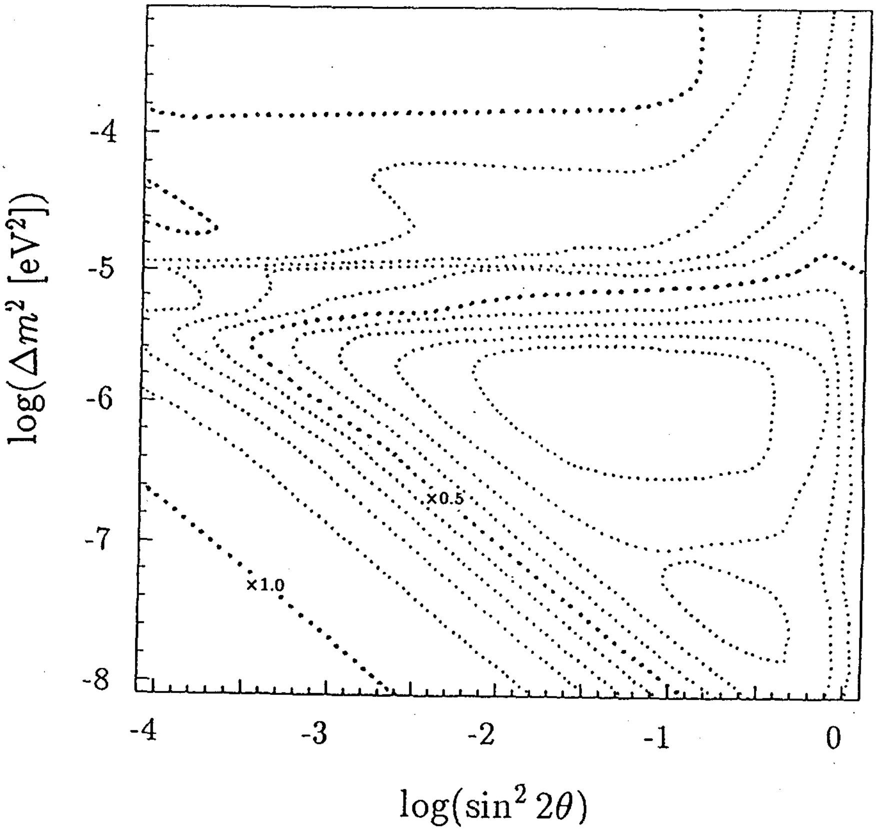

Fig. 3.10(c)

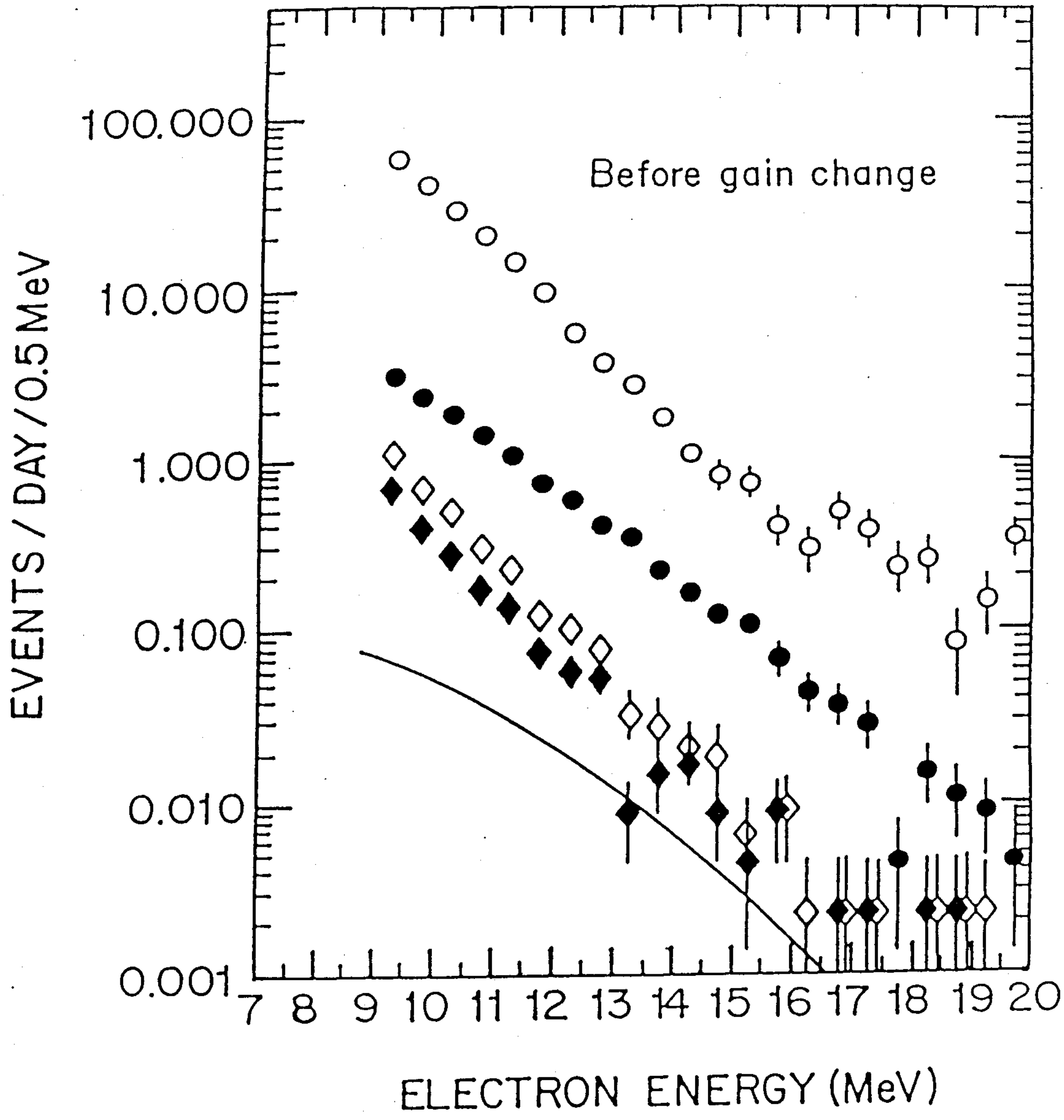
Before gain change
EVENTS / DAY / 0.5 MeV
100.000
10.000
1.000
0.100
0.010
0.001
7
8
9
10
11
12
13
14
15
16
17
18
19
20
ELECTRON ENERGY (MeV)

Fig. 4.1(a)

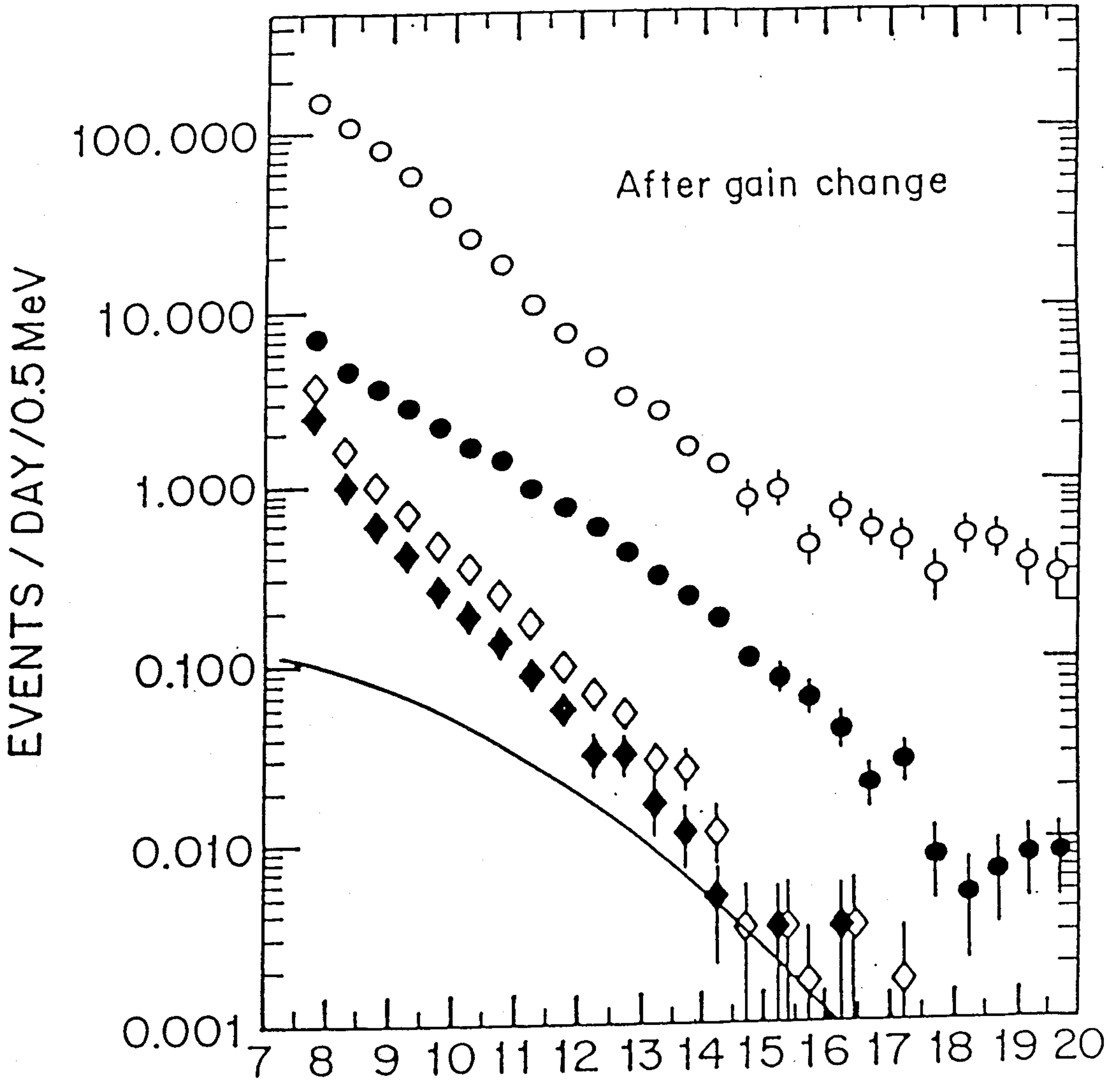
After gain change
EVENTS / DAY / 0.5 MeV
100.000
10.000
1.000
0.100
0.010
0.001
7
8
9
10
11
12
13
14
15
16
17
18
19
20
ELECTRON ENERGY (MeV)

Fig. 4.1(b)

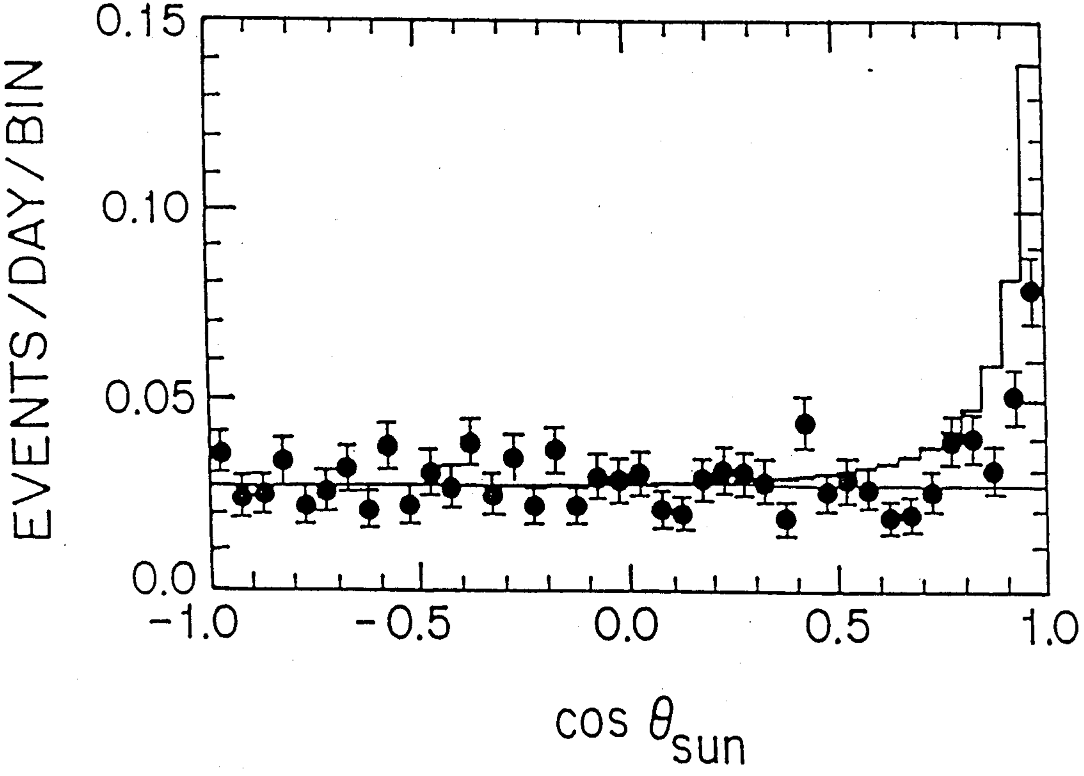

Fig. 4.2

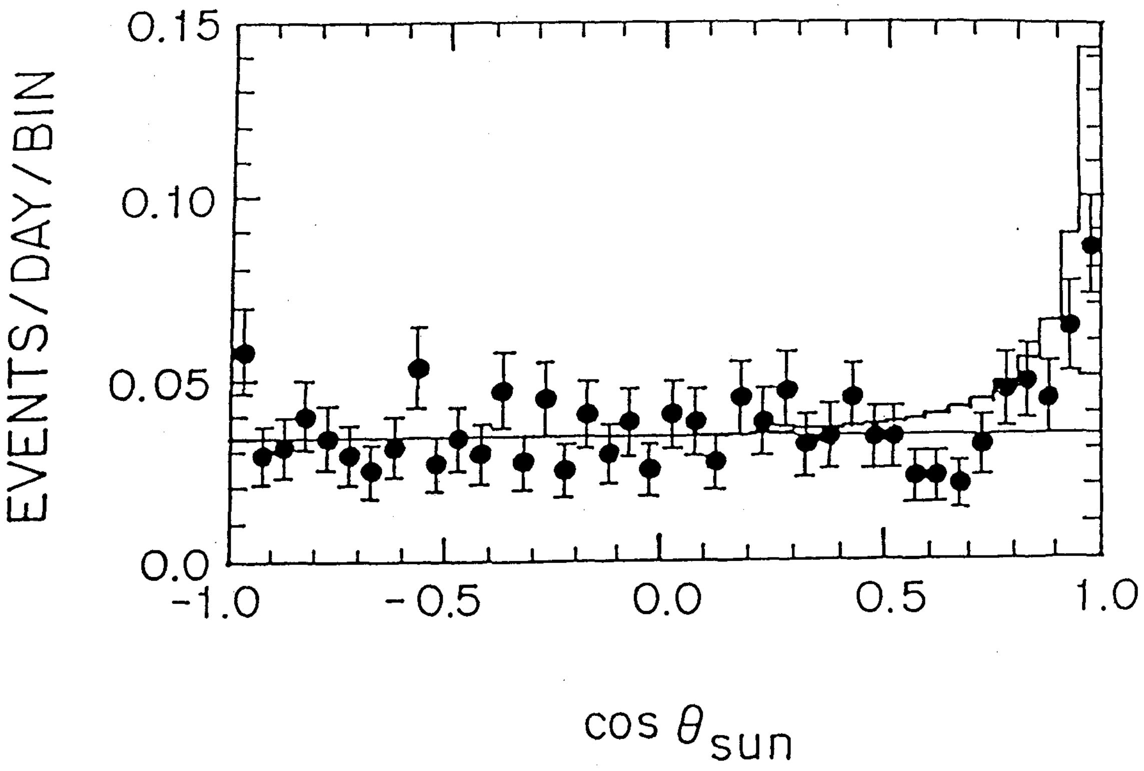

Fig. 4.3(a)

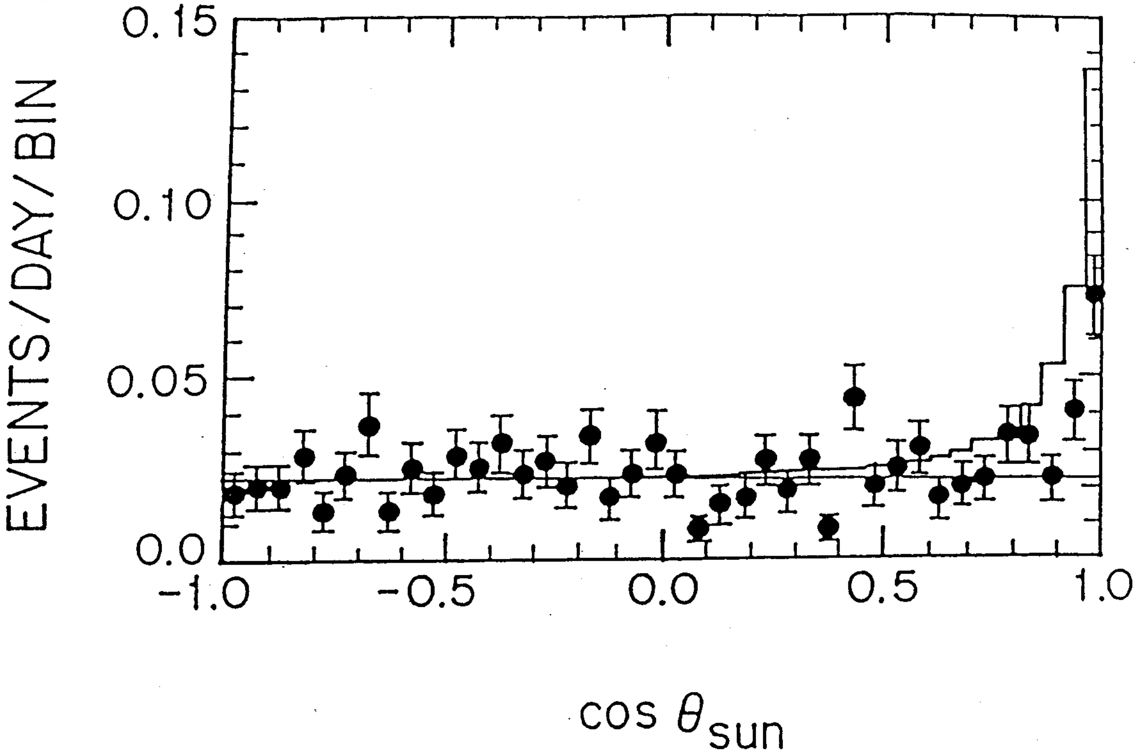

Fig. 4.3(b)

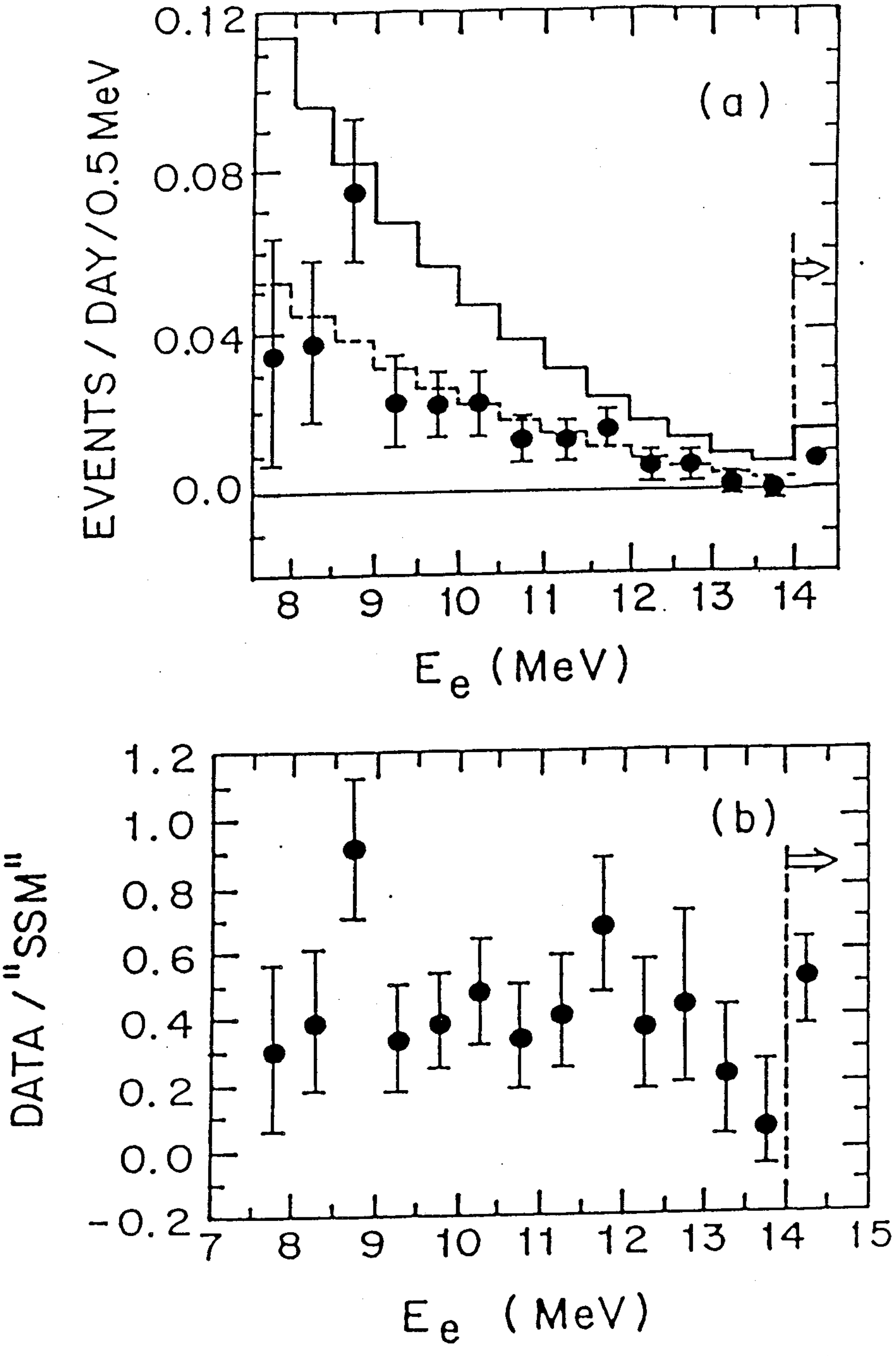
0.12
0.08
0.04
0.0
EVENTS / DAY/0.5 MeV
(a)
8
9
10
11
12
13
14
E_e (MeV)
1.2
1.0
0.8
0.6
0.4
0.2
0.0
-0.2
DATA / "SSM"
(b)
7
8
9
10
11
12
13
14
15
E_e (MeV)

Fig. 4.4

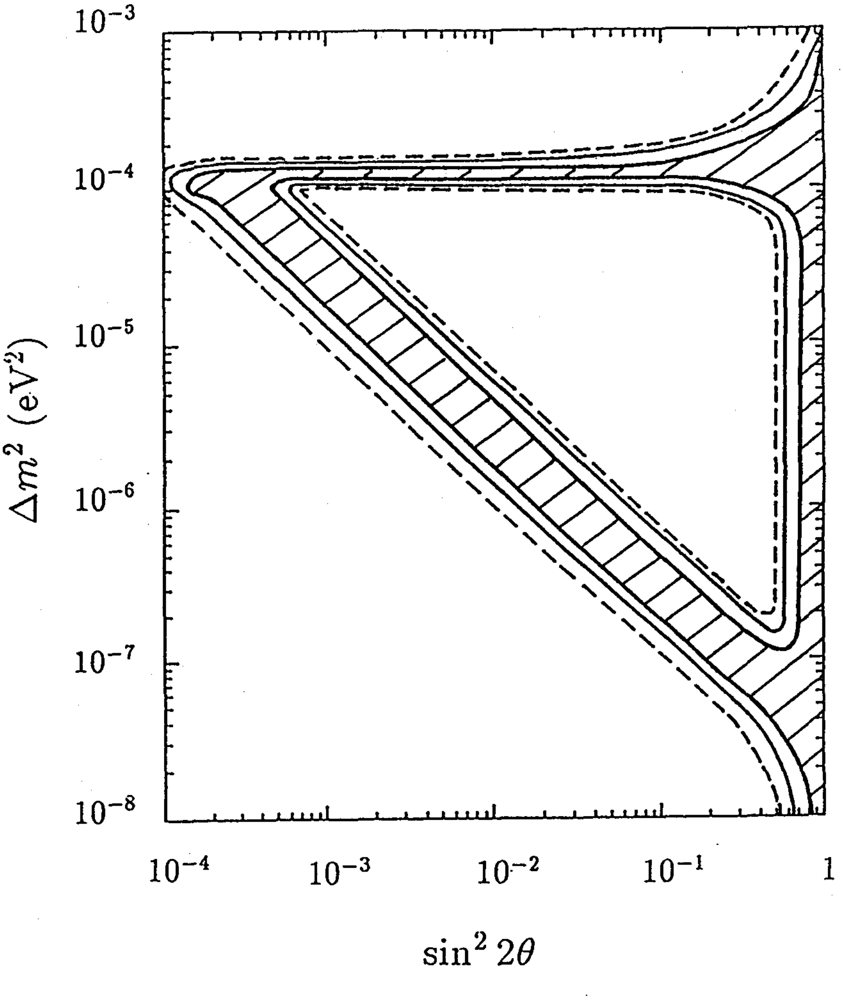

Fig. 4.5

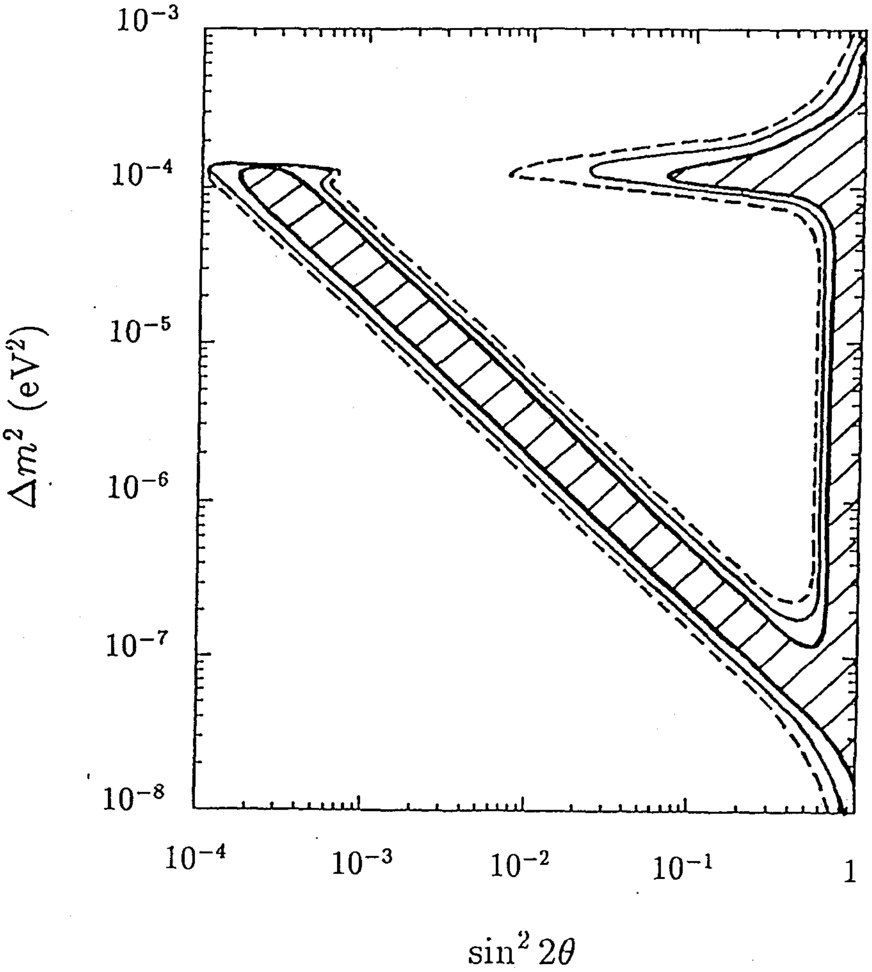

10^{-3}
10^{-4}
10^{-5}
10^{-6}
10^{-7}
10^{-8}
Δm^2 (eV^2)
10^{-4}
10^{-3}
10^{-2}
10^{-1}
1
$\sin^2 2\theta$

Fig. 4.6

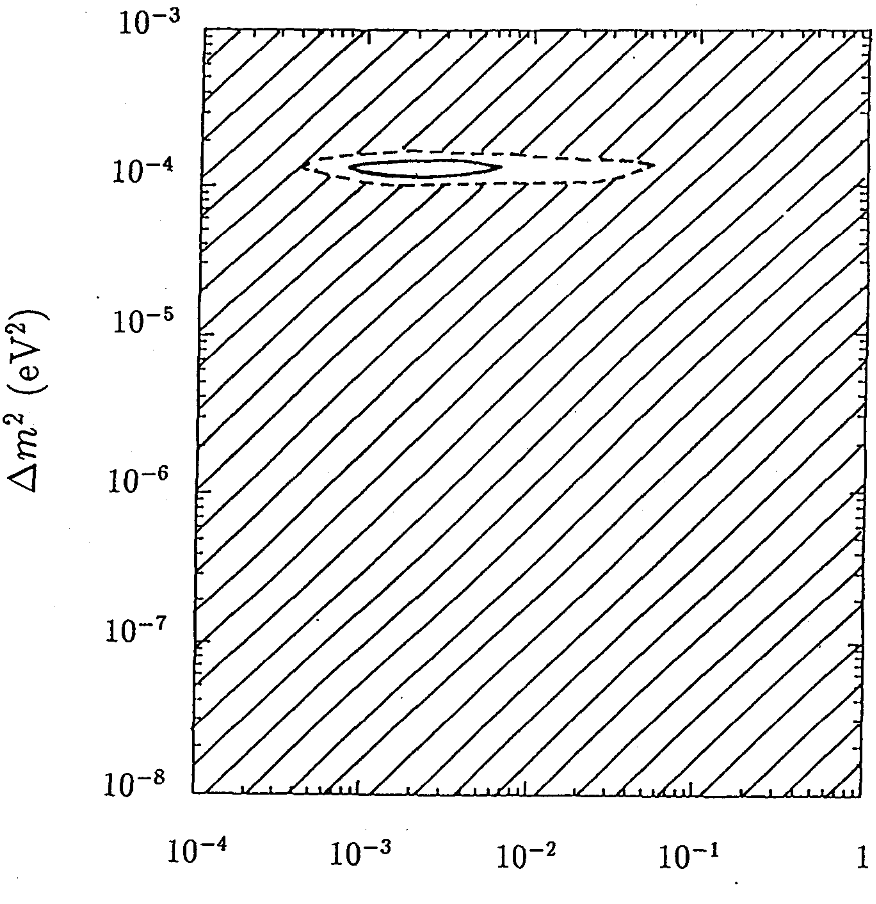

Fig. 4.7

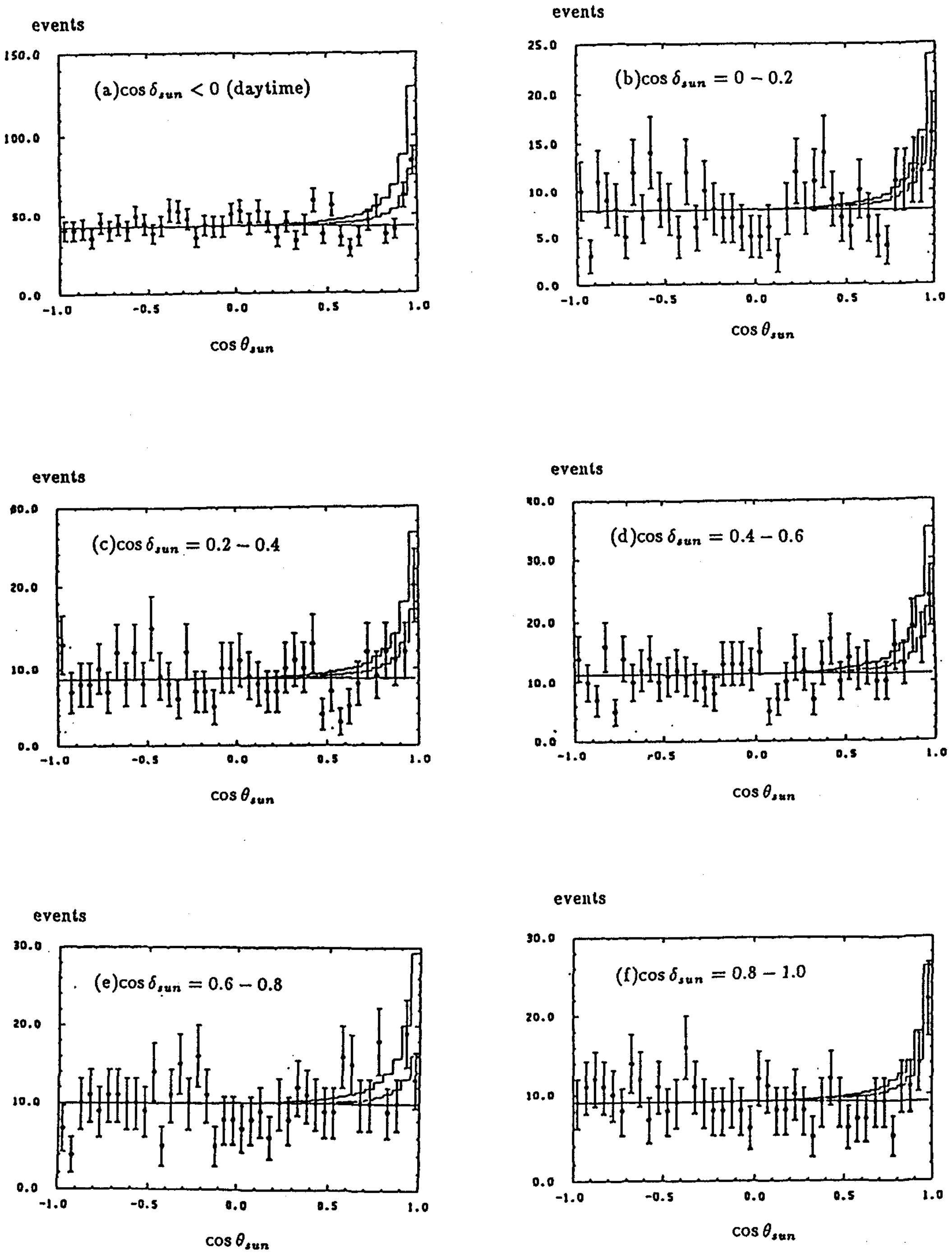
events
150.0
100.0
50.0
0.0
-1.0
-0.5
0.0
0.5
1.0
$\cos\theta_{sun}$
(a) $\cos\delta_{sun} < 0$ (daytime)
events
25.0
20.0
15.0
10.0
5.0
0.0
-1.0
-0.5
0.0
0.5
1.0
$\cos\theta_{sun}$
(b) $\cos\delta_{sun} = 0 - 0.2$
events
30.0
20.0
10.0
0.0
-1.0
-0.5
0.0
0.5
1.0
$\cos\theta_{sun}$
(c) $\cos\delta_{sun} = 0.2 - 0.4$
events
40.0
30.0
20.0
10.0
0.0
-1.0
-0.5
0.0
0.5
1.0
$\cos\theta_{sun}$
(d) $\cos\delta_{sun} = 0.4 - 0.6$
events
30.0
20.0
10.0
0.0
-1.0
-0.5
0.0
0.5
1.0
$\cos\theta_{sun}$
(e) $\cos\delta_{sun} = 0.6 - 0.8$
events
30.0
20.0
10.0
0.0
-1.0
-0.5
0.0
0.5
1.0
$\cos\theta_{sun}$
(f) $\cos\delta_{sun} = 0.8 - 1.0$

Fig. 4.8

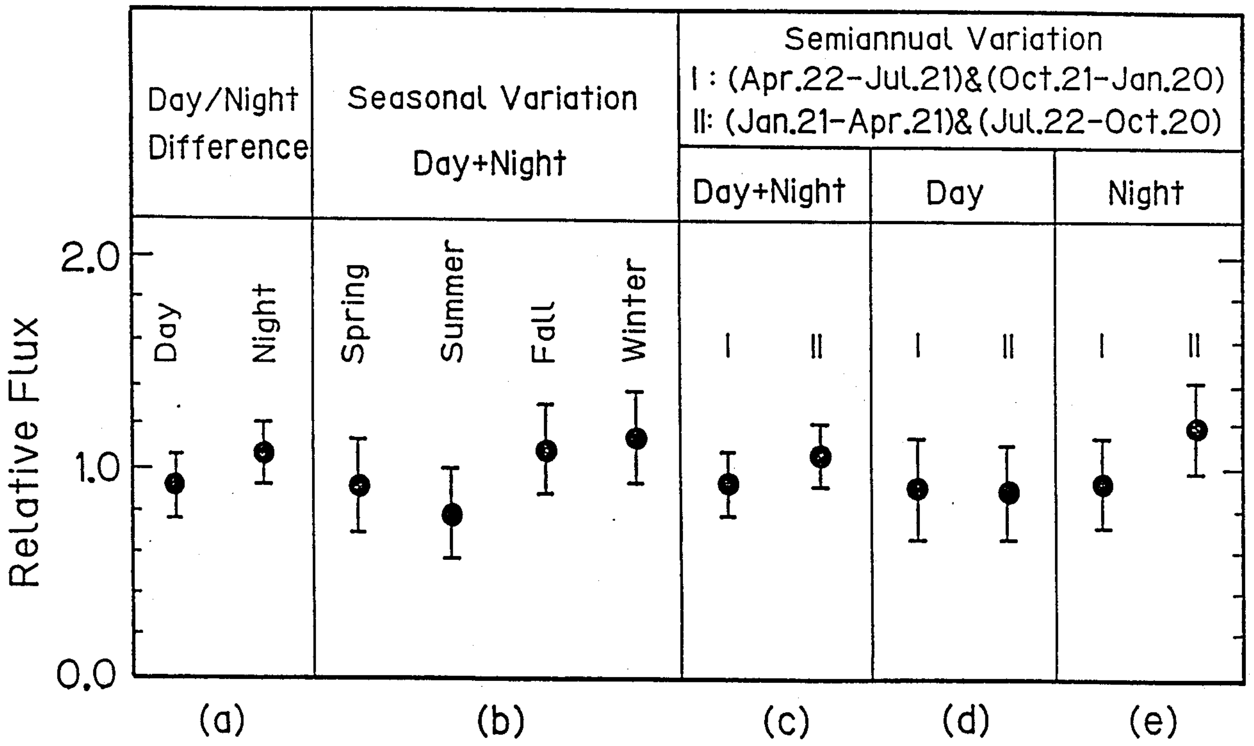
Day/Night Difference
Seasonal Variation
Day+Night
Semiannual Variation
I : (Apr.22-Jul.21)&(Oct.21-Jan.20)
II: (Jan.21-Apr.21)&(Jul.22-Oct.20)
Day+Night
Day
Night
Relative Flux
2.0
1.0
0.0
Day
Night
Spring
Summer
Fall
Winter
I
II
I
II
I
II
(a)
(b)
(c)
(d)
(e)

Fig. 4.9

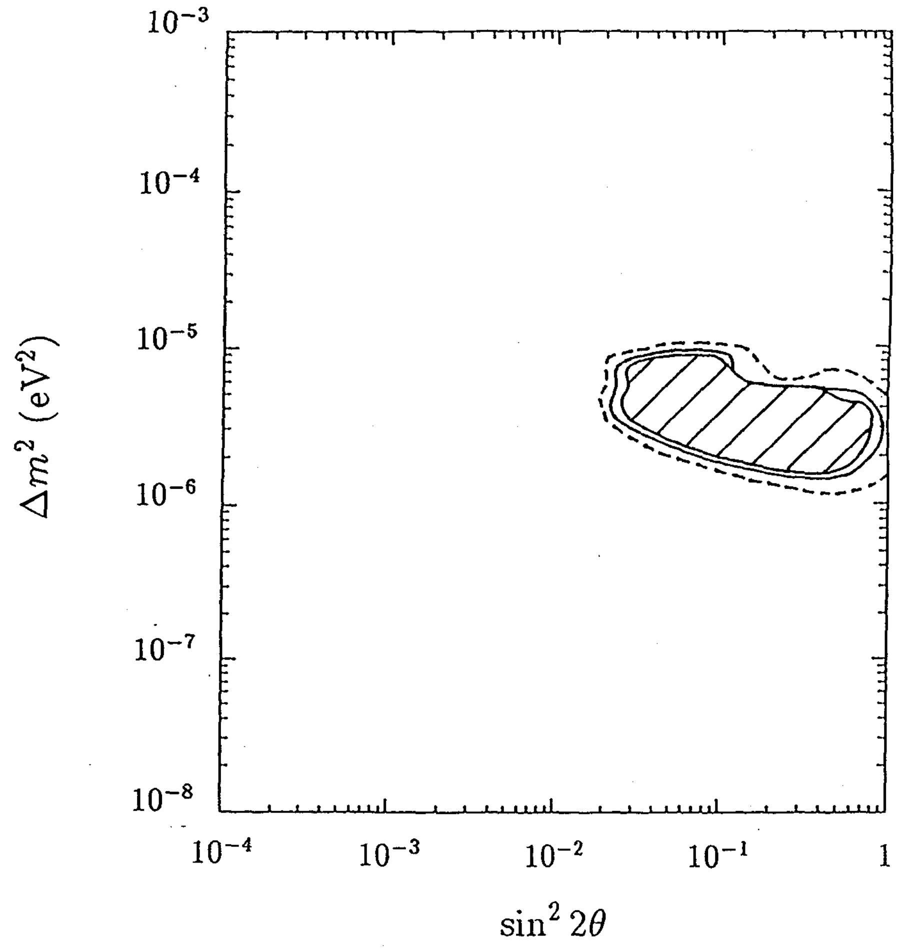
10^{-3}
10^{-4}
10^{-5}
10^{-6}
10^{-7}
10^{-8}
Δm^2 (eV^2)
10^{-4}
10^{-3}
10^{-2}
10^{-1}
1
$\sin^2 2\theta$

Fig. 4.10

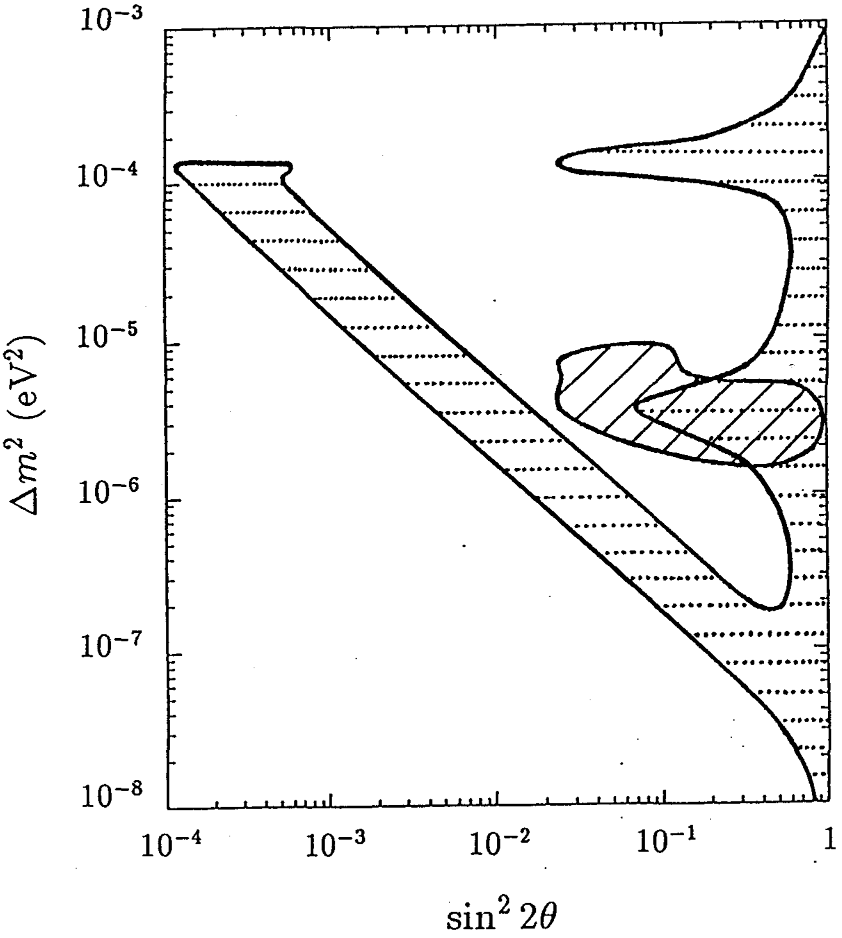
10^{-3}
10^{-4}
10^{-5}
10^{-6}
10^{-7}
10^{-8}
Δm^2 (eV^2)
10^{-4}
10^{-3}
10^{-2}
10^{-1}
1
$\sin^2 2\theta$

Fig. 5.1

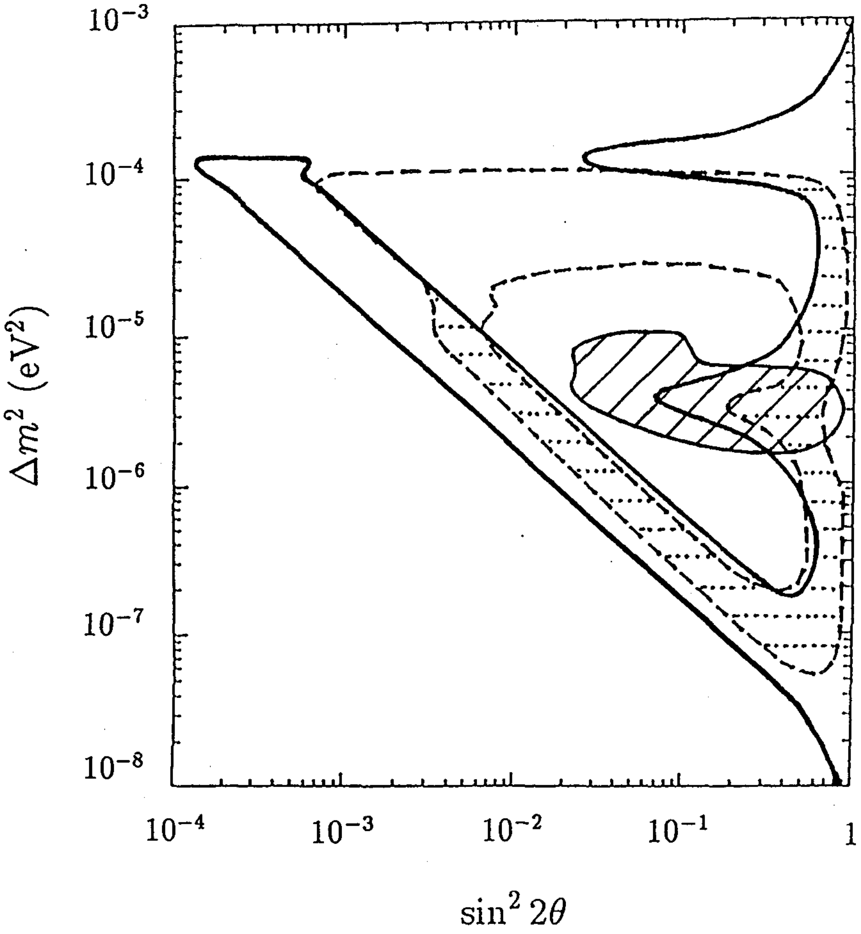
10^{-3}
10^{-4}
10^{-5}
10^{-6}
10^{-7}
10^{-8}
Δm^2 (eV^2)
10^{-4}
10^{-3}
10^{-2}
10^{-1}
1
$\sin^2 2\theta$

Fig. 5.2

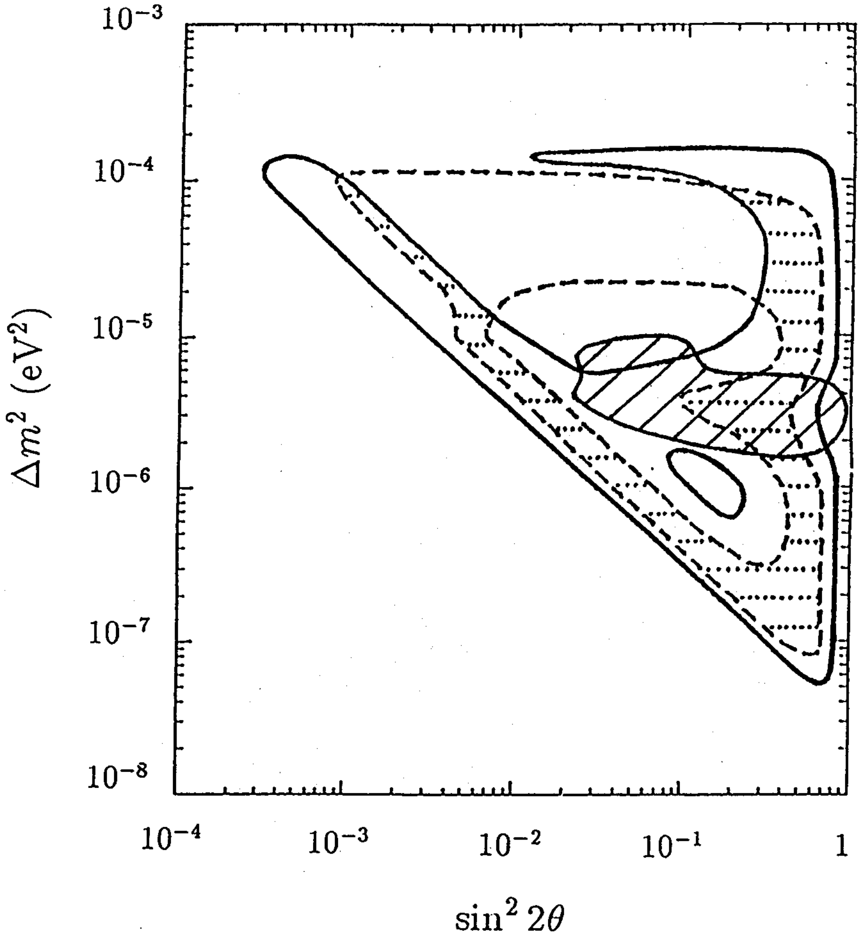
10^{-3}
10^{-4}
10^{-5}
10^{-6}
10^{-7}
10^{-8}
Δm^2 (eV^2)
10^{-4}
10^{-3}
10^{-2}
10^{-1}
1
$\sin^2 2\theta$

Fig. 5.3(a)

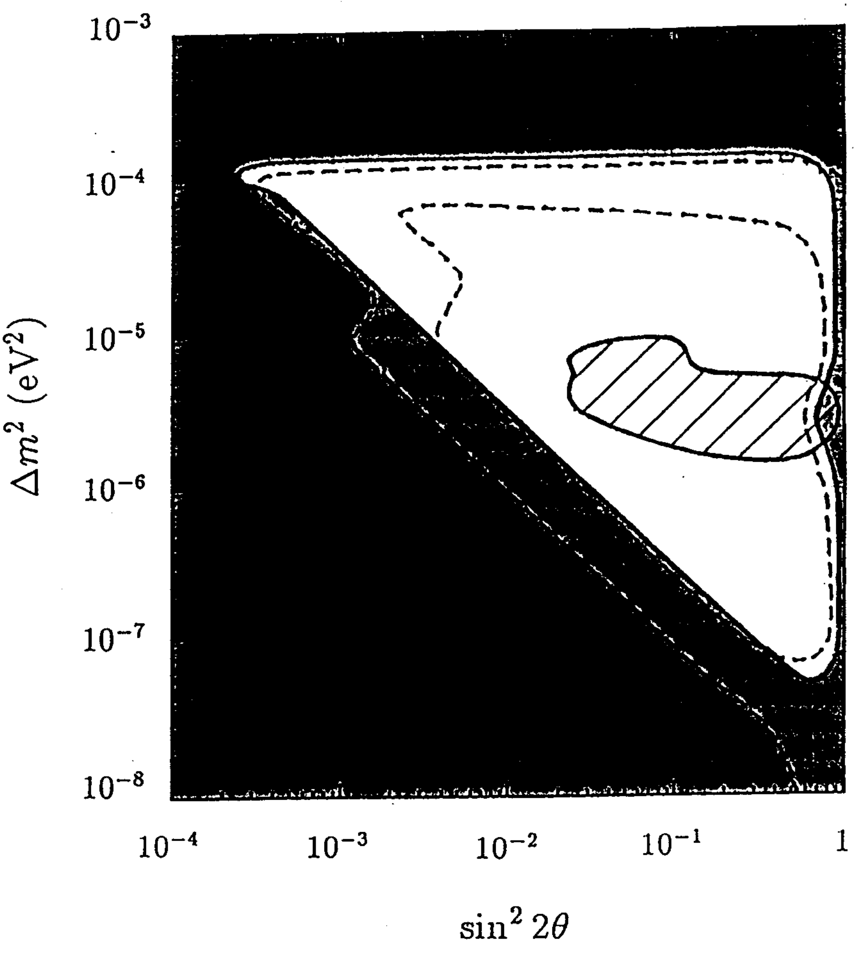

Fig. 5.3(b)

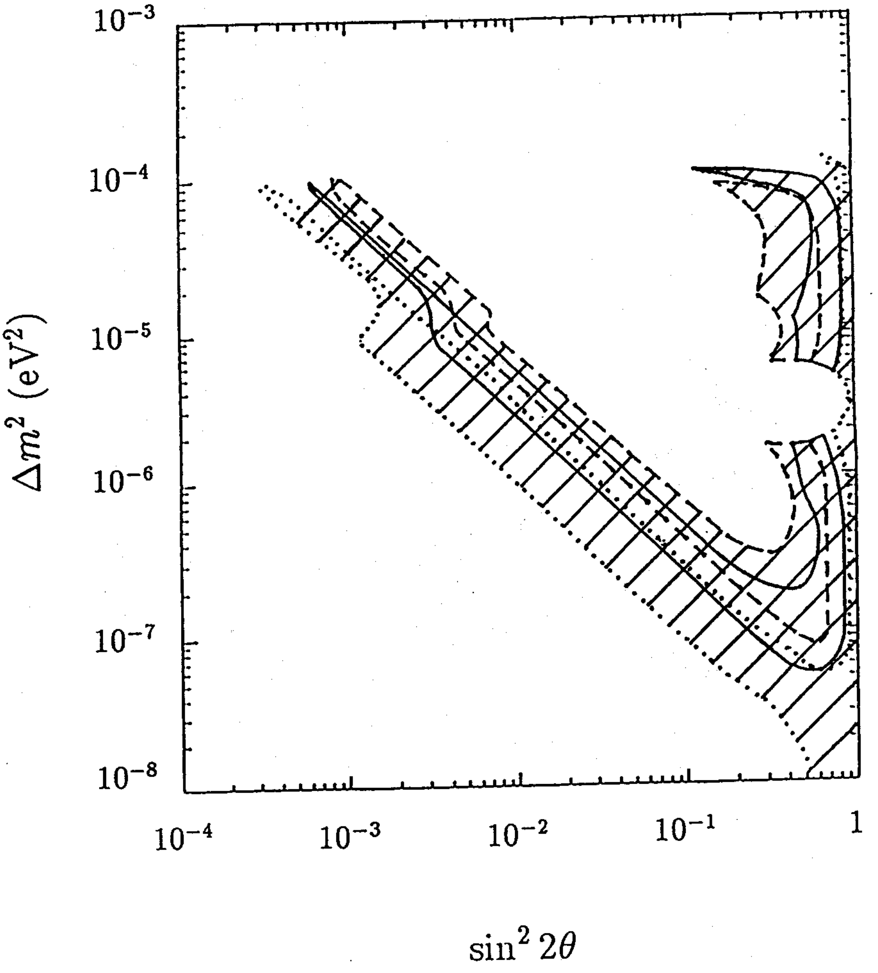
10^{-3}
10^{-4}
10^{-5}
10^{-6}
10^{-7}
10^{-8}
Δm^2 (eV^2)
10^{-4}
10^{-3}
10^{-2}
10^{-1}
1
$\sin^2 2\theta$

Fig. 5.4

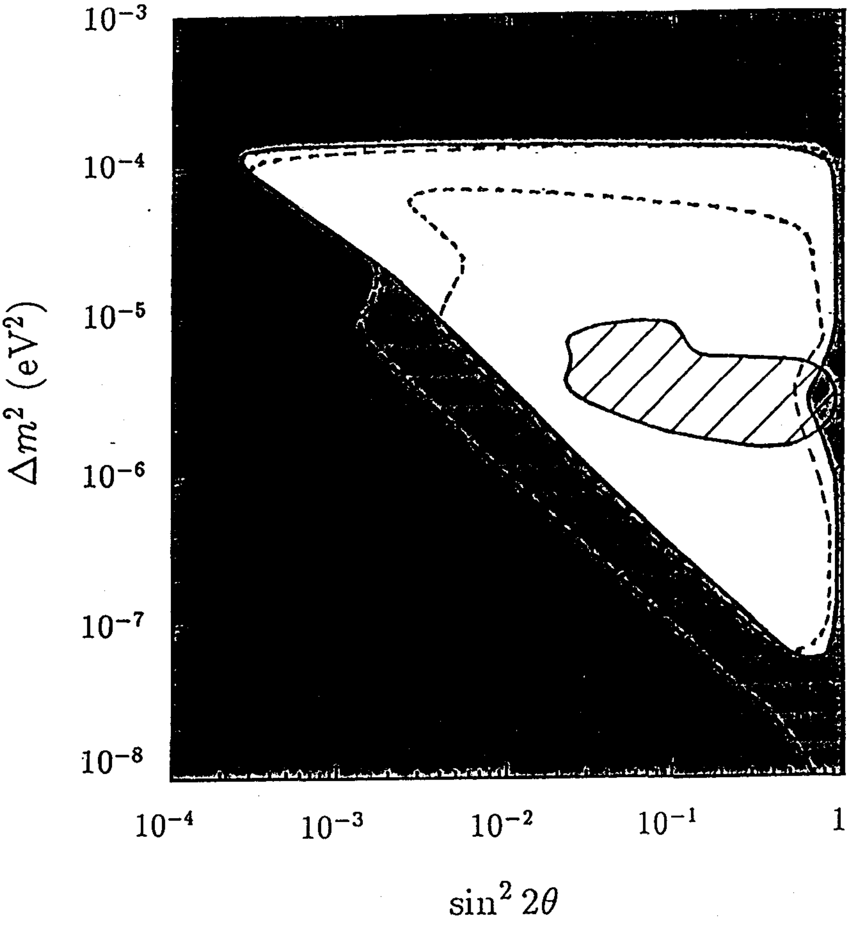
10^{-3}
10^{-4}
10^{-5}
10^{-6}
10^{-7}
10^{-8}
Δm^2 (eV^2)
10^{-4}
10^{-3}
10^{-2}
10^{-1}
1
$\sin^2 2\theta$

Fig. 5.5

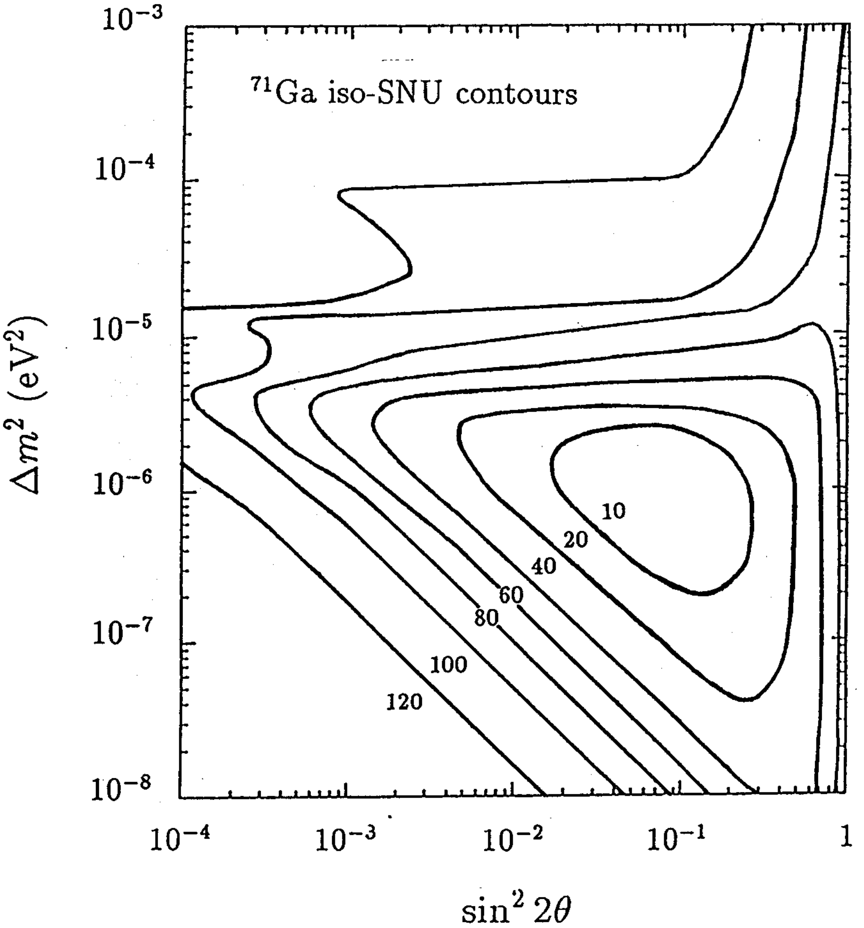
^{71}Ga iso-SNU contours
10
20
40
60
80
100
120
10^{-3}
10^{-4}
10^{-5}
10^{-6}
10^{-7}
10^{-8}
Δm^2 (eV^2)
10^{-4}
10^{-3}
10^{-2}
10^{-1}
1
$\sin^2 2\theta$

Fig. 5.6

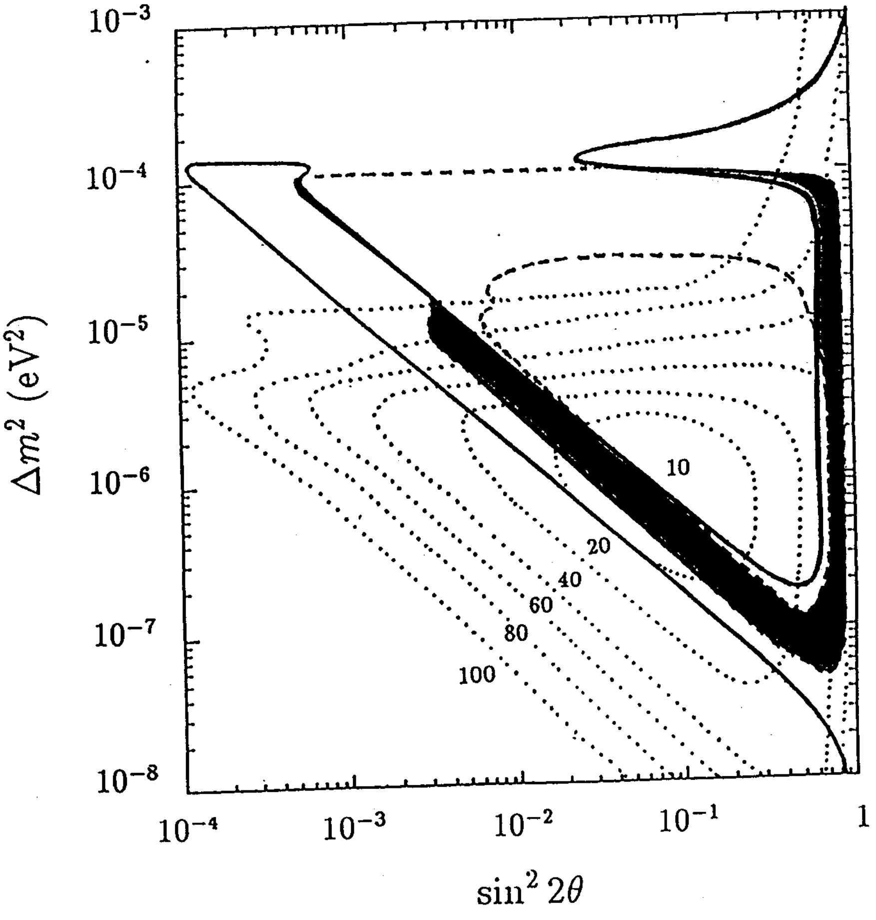
10^{-3}
10^{-4}
10^{-5}
10^{-6}
10^{-7}
10^{-8}
Δm^2 (eV^2)
10
20
40
60
80
100
10^{-4}
10^{-3}
10^{-2}
10^{-1}
1
$\sin^2 2\theta$

Fig. 5.7

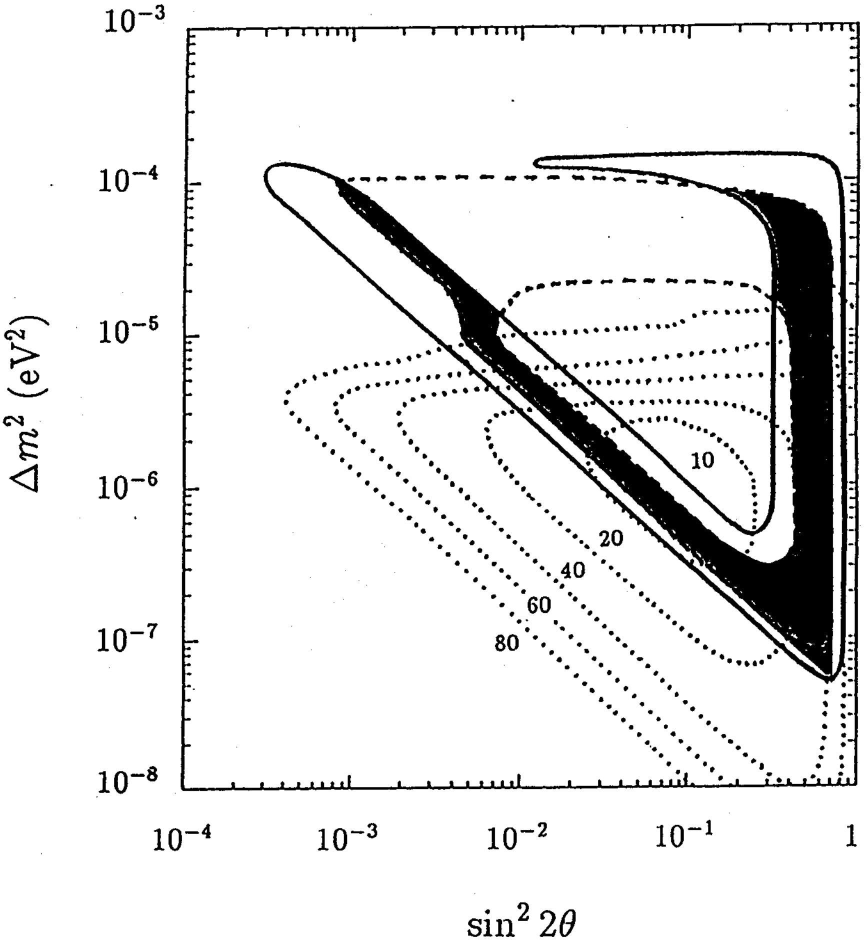
10^{-3}
10^{-4}
10^{-5}
10^{-6}
10^{-7}
10^{-8}
Δm^2 (eV^2)
10
20
40
60
80
10^{-4}
10^{-3}
10^{-2}
10^{-1}
1
$\sin^2 2\theta$

Fig. 5.8(a)

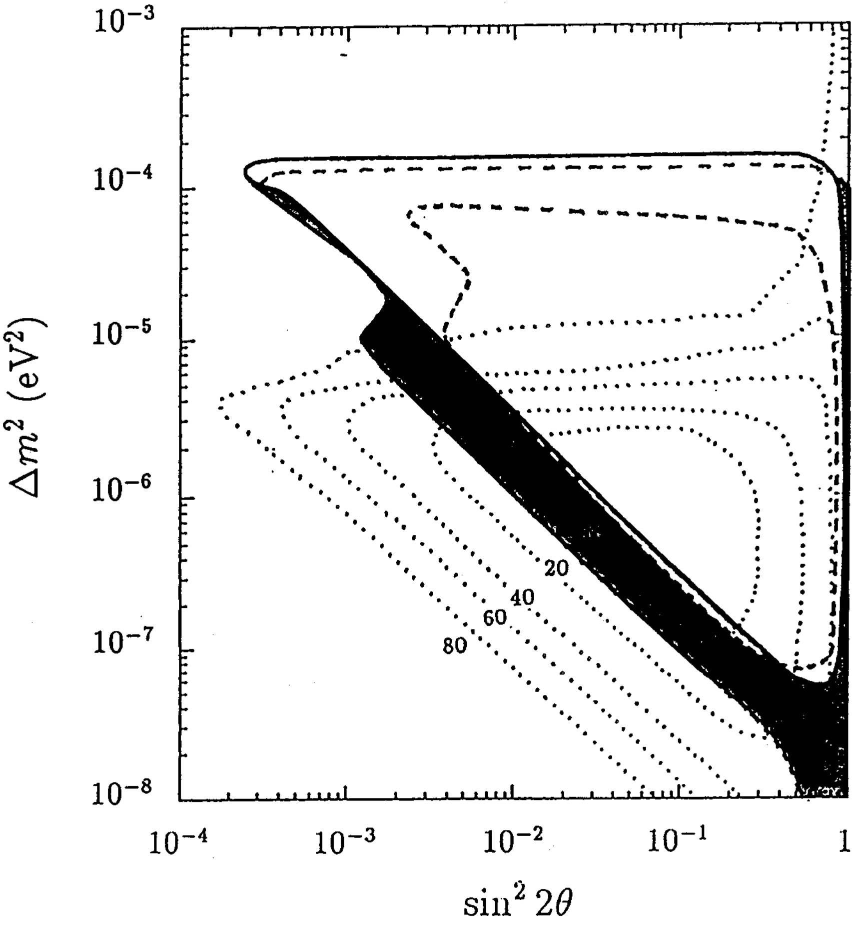
10^-3
10^-4
10^-5
10^-6
10^-7
10^-8
Δm² (eV²)
10^-4
10^-3
10^-2
10^-1
1
sin² 2θ
20
40
60
80

Fig. 5.8(b)

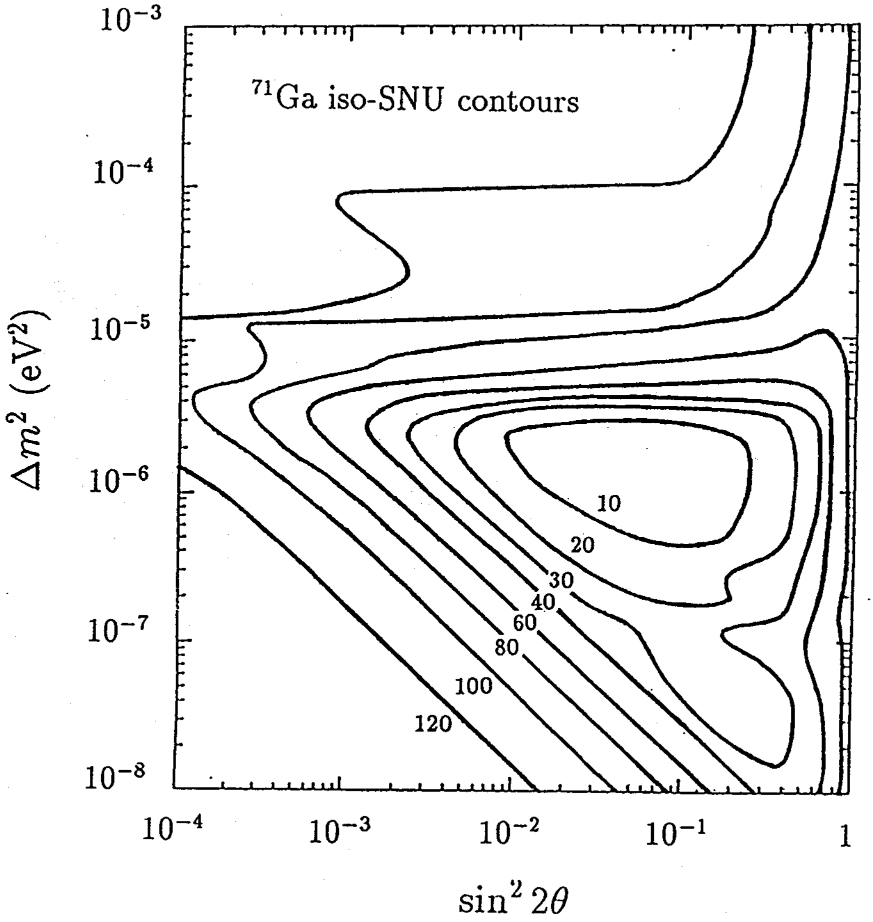
^{71}Ga iso-SNU contours
Δm^2 (eV^2)
10^{-3}
10^{-4}
10^{-5}
10^{-6}
10^{-7}
10^{-8}
$\sin^2 2\theta$
10^{-4}
10^{-3}
10^{-2}
10^{-1}
1
10
20
30
40
60
80
100
120

Fig. 5.9

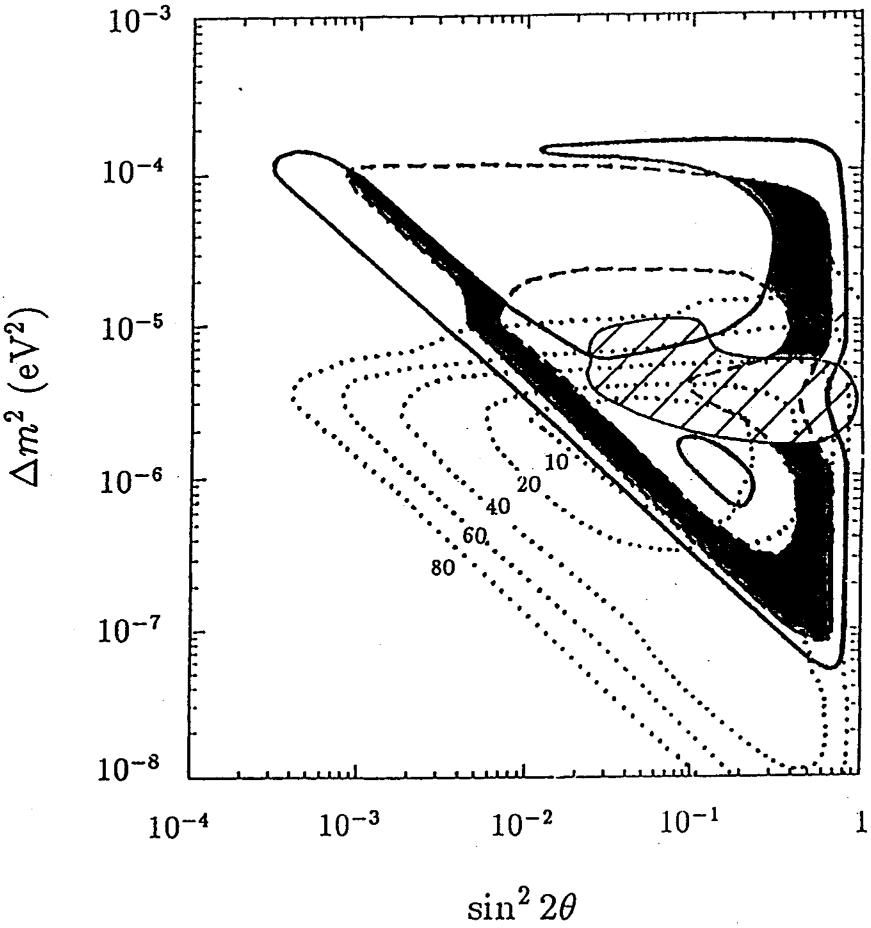
10^{-3}
10^{-4}
10^{-5}
10^{-6}
10^{-7}
10^{-8}
Δm^2 (eV^2)
10
20
40
60
80
10^{-4}
10^{-3}
10^{-2}
10^{-1}
1
$\sin^2 2\theta$

Fig. 5.10(a)

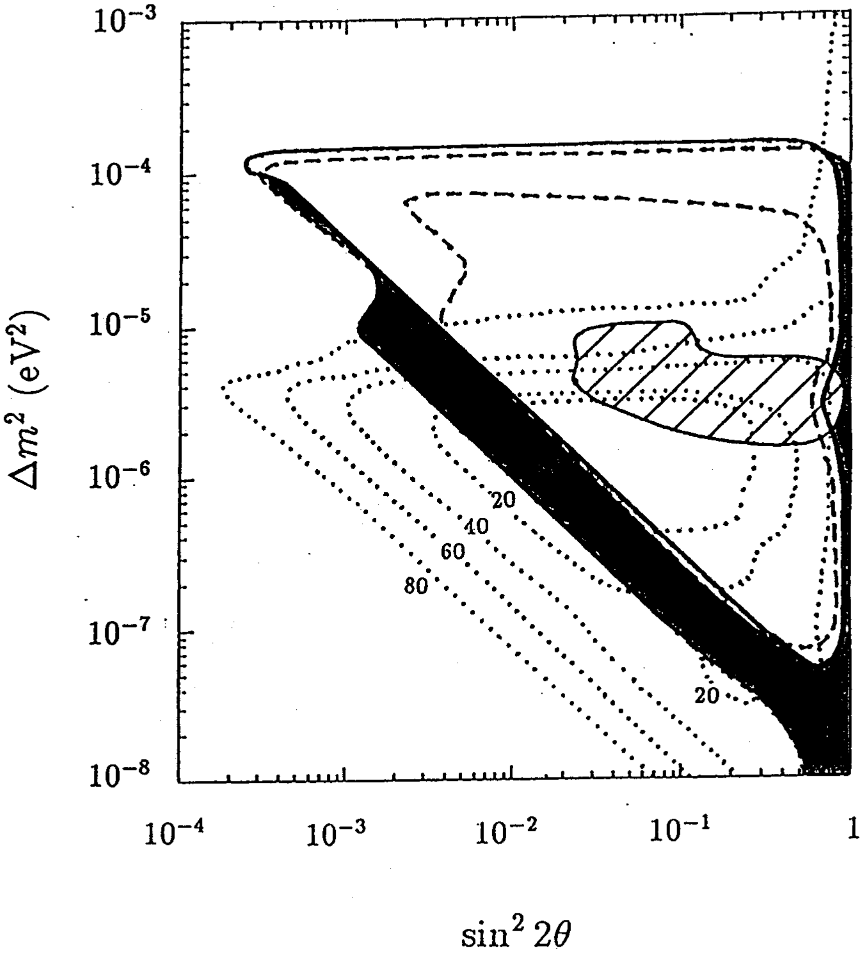

10^{-3}
10^{-4}
10^{-5}
10^{-6}
10^{-7}
10^{-8}
Δm^2 (eV^2)
20
40
60
80
20
10^{-4}
10^{-3}
10^{-2}
10^{-1}
1
$\sin^2 2\theta$

Fig. 5.10(b)

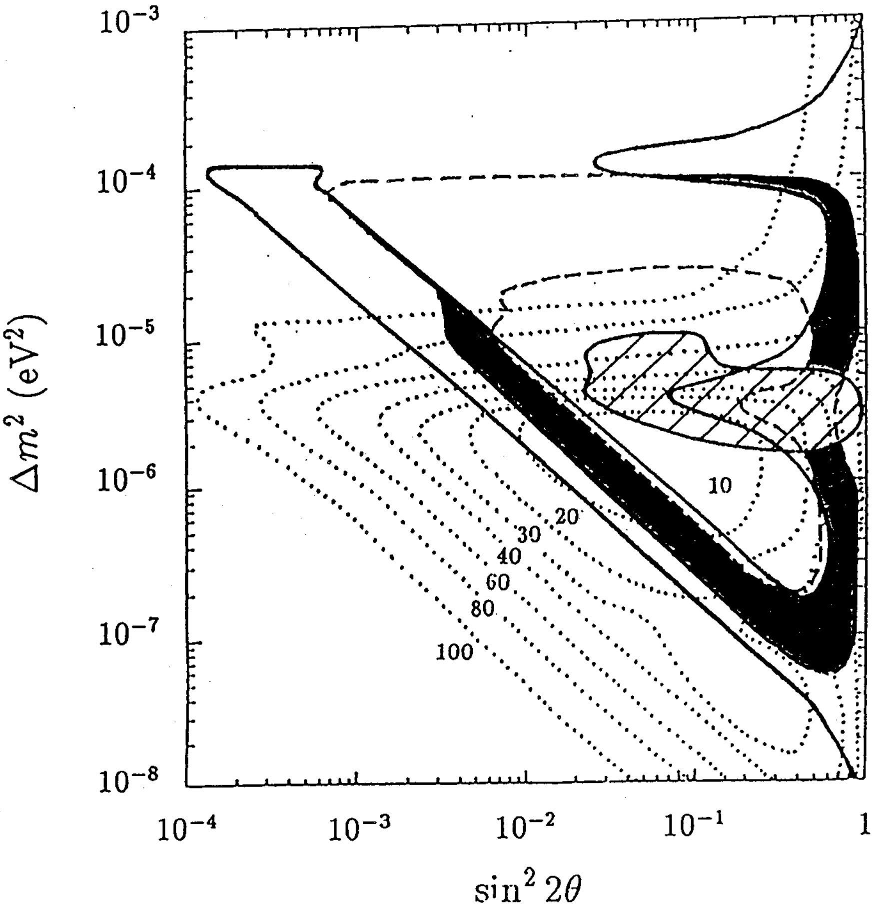

10^{-3}
10^{-4}
10^{-5}
10^{-6}
10^{-7}
10^{-8}
Δm^2 (eV^2)
10
20
30
40
60
80
100
10^{-4}
10^{-3}
10^{-2}
10^{-1}
1
$\sin^2 2\theta$

Fig. 5.11

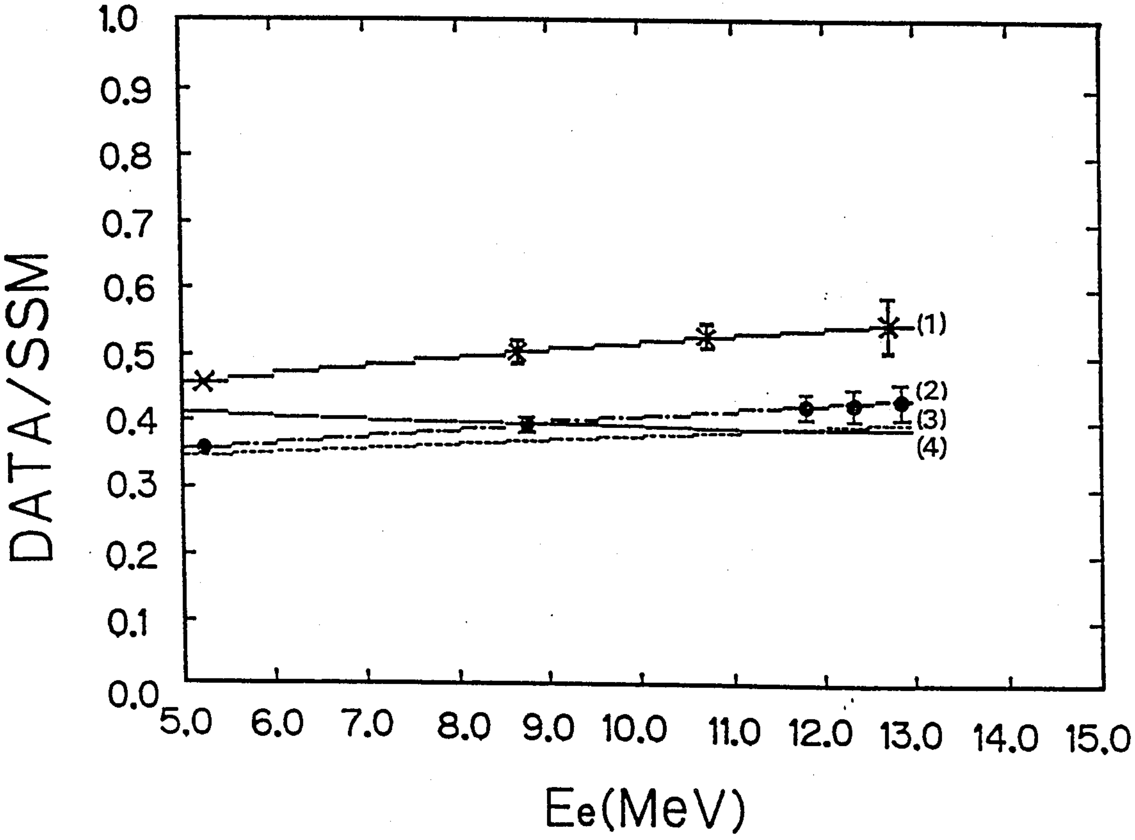
DATA/SSM
1.0
0.9
0.8
0.7
0.6
0.5
0.4
0.3
0.2
0.1
0.0
5.0
6.0
7.0
8.0
9.0
10.0
11.0
12.0
13.0
14.0
15.0
Ee(MeV)
(1)
(2)
(3)
(4)

Fig. 5.12